THESIS FOR THE DEGREE OF LICENTIATE OF ENGINEERING

Investigation of Issues Related to Electrical Efficiency Improvements of Pump and Fan Drives in Buildings

JOHAN ÅSTRÖM

Department of Energy and Environment
Division of Electric Power Engineering
CHALMERS UNIVERSITY OF TECHNOLOGY
Göteborg, Sweden 2008

Investigation of Issues Related to Electrical Efficiency Improvements of Pump and Fan Drives in Buildings
JOHAN ÅSTRÖM

Licentiante Thesis at the Chalmers University of Technology

Department of Energy and Environment
Division of Electric Power Engineering
Chalmers University of Technology
SE–412 96 Göteborg
Sweden
Telephone +46 (0)31–772 1000

Chalmers Bibliotek, Reproservice
Göteborg, Sweden 2008

Investigation of Issues Related to Electrical Efficiency Improvements of Pump and Fan Drives in Buildings

JOHAN ÅSTRÖM
Department of Energy and Environment
Chalmers University of Technology

Abstract

This thesis deals with issues related to efficiency of building related pump and fan drive systems. Different motor technologies are analyzed and a more detailed study on inverter fed Induction Motors (IM) is presented. A 4-pole, 4kW IM has been the focus of investigation, where different energy labels (eff1, eff2 and eff3), different voltage/frequency (V/Hz) control and different switching schemes of the frequency converter have been analyzed. Simulations as well as measurements have been performed with a close correlation of the results. The simulation results have then been used in order to analyze the saving potential for different load profiles. The general conclusion is that savings will be made during the life time of the drive system, both for an IM and frequency converter replacement. The analysis also show that the choice between an eff2 and eff1 IM, for the given load profiles, always generate the highest saving for the eff1 IM in economical terms, including the increased cost for an eff1 motor. It is interesting to note that, during the time period 1998-2003, eff2 label took 86% of the market share compared to eff1 8% and eff3 6%. It is also shown that losses introduced by the common over dimensioning of the pump and fan motor can result in increased energy efficiency with appropriate converter control compared with the use of a motor with lower rating. Finally, a study on modeling of the IM for bearing current prediction is presented containing a literature study and laboratory measurements.

Index Terms: Induction motor, permanent magnet motor, frequency converter, loss model, efficiency measurement, HVAC load profiles and saving potential.

Preface

This thesis is a part of a larger project that has been conducted in cooperation with the division of Building Service Engineering and the division of Electric Power Engineering, within the department of Energy and Environment at Chalmers. The common objective of this project has been to identify saving potentials in building related pump and fan operation. The focus of the work at the division of Building Service Engineering has been on the system side of the applications, whereas, the focus on the electrical part of the system has been the main target for the work conducted at Electric Power Engineering. It is of course not possible to make a clear distinction between the two areas, hence a cooperation has been important and valuable. This thesis will mainly deal with the electrical part of the system but in some extent also discuss Building Service related issues.

Acknowledgements

The financial support given by Göteborgs Energi, Energimyndigheten and Formas is gratefully acknowledged.

In addition, twenty companies have been involved in the project mainly by attending project meetings. Special thanks to FläktWoods, Grundfos, and Wilo for providing the project with test objects and for the time they have invested in many valuable company visits. I would like to thank my supervisor Dr. Torbjörn Thiringer for his supervision, his encouraging attitude, constructive feedback and for many interesting discussions. I would also like to thank my examiner Prof. Tore Undeland for his support and comments during our meetings.

I would also like to thank all my colleges and especially Magnus Ellsén, Robert Karlsson and Aleksander Bartnicki for their help with many practical things during this time. Also, a special thank to Andreas Karvonen for many constructive discussions.

Finally, I would like to thank Prof. Per Fahlén and PhD student Caroline Markusson at the division of Building Service Engineering and Dr. Lennart Jagemar at CIT Energy Management for a good cooperation.

Johan Åström
Göteborg, Sweden
June, 2008

Contents

Chapter 1

Introduction

1.1 Problem Background

A common goal of nations world wide is to produce and supply electricity in a way that is safe and environmentally friendly to the lowest cost possible. However, the majority of energy production causes negative effects on the environment and many environmental experts points out the connection between CO_2 emission and the increase in the global mean temperature. In order to reduce the energy consumption from non renewable energy sources, it is not only important to increase the use of renewable energy sources but also to reduce the energy use itself. Today, the electric power consumption in Sweden accounts for 140TWh where 31% [1] is consumed by the building sector (industries excluded). A significant part of this consumption comes from permanent installations such as pumps and fans. One problem is that the end user is not always responsible for all sources of electrical consumption and especially not for the permanent installations, made by the proprietor. Another problem is related to the interest of making an energy efficient installation. Usually, the proprietor does not ”pay the electric bill” and are only interested in a low initial cost, not in the electrical operating cost [2]. In order to overcome this problem, energy certification of buildings will be mandatory in the near future [1], increasing the need for energy efficient solutions.

Studies have been made in the area of Heating Ventilation and Air Condition (HVAC) applications. Both with respect to different system concepts and different electric drive technologies. However, the focus has been on large machines [3] due to the small power requirement of the individual component. As a result, few studies have been made on small and medium sized pumps and fans [4, 5]. However, buildings contain a large number of small and medium sized pumps and fans which altogether are responsible for a non insignificant part of the electrical consumption.

The large assortment of different drive systems on today’s market results in a difficult task in making the correct decision for a given application. The differences in potential savings between different concepts have not been established and is far from common

knowledge by the an installer or consumer.

Another aspect worth to consider is the dimensioning of HVAC systems. In an example taken from [6], approximately 40% savings where possible for a Constant Air Volume (CAV) system delivering 20% higher flow than needed. One of the reasons for this poor efficiency is that Induction Motors (IM) have a low efficiency at light load. An interesting issue is accordingly if these ”over dimensioning losses” can be reduced by using modern converter technology.

1.2 Literature overview

The energy efficiency of electric drives has been extensively studied in the literature. The IM is the most commonly used motors today and studies have been made on optimal control regarding IM efficiency [7, 8, 9]. Focus has been placed on different control methods in order to obtain optimal operation and evaluation of the resulting IM efficiency improvement. Furthermore, different loss models have been proposed [10, 11], in order to include all the loss components in the IM together with evaluation of its validity.

The Efficiency improvement of frequency converters have also been the target of extensive research. Frequency converter control schemes, using different switching schemes to decrease switching losses, [12, 13, 14] is the most common approach. Moreover, the development in power electronic devices have also made it possible to choose between a larger range of components. Comparative studies have been made of different devices and their counterparts [15, 16, 17]. Features such as switching transitions, thermal behavior and conduction losses are often the topic of the comparison.

1.3 Purpose of the work

The area of energy efficiency has been the target of research for a long time. However, there is still a lack of comparative studies of saving potential for different HVAC applications caused by different drive system setups. Furthermore, development in power electronics, electrical motors, different system concepts etc introduces new areas of investigation on a daily basis. The general objectives of this work is divided into five parts with focus on part 2,3 and 4.

- Establish relevant load profiles for evaluation of energy savings.
- Perform an investigation of motor and power electronic technologies and their energy efficiency
- Verify theoretical assumptions on an available induction motor drive system, in this case a 4kW motor.

- Analyze the potential savings using improved motor and power electronic technology as well as improved control methods for different load profiles.
- Investigate the negative effects of introducing power electronics in drive systems.

1.4 Outline of Thesis

Chapter 2 will describe different HVAC loads in buildings. Basic pump/fan operation and possible load profiles will be provided. In Chapter 3, the different types of electric drives used for HVAC applications will be described. Furthermore, the chapter also aims to give readers, not familiar with electric drive systems, power electronics and power quality, enough insight in order to understand later chapters dealing with these concepts. Chapter 4 will present the drive system models used in this thesis. Both steady state and dynamic models will be provided with focus on energy efficiency determination. In Chapter 5 the result from the field measurements on different pump applications are presented where measurements of the electric input power has been logged for 22 months. Chapter 6 will describe different control strategies for improving the efficiency in the IM and the frequency converter. Furthermore, simulation results will be provided using the models presented in Chapter 4. In Chapter 7, the control strategies presented in Chapter 6 will be analyzed using laboratory measurements on an IM fed by a frequency converter. Chapter 8 will analyze, the potential savings in an IM drive system for different load profiles, based on Chapter 2, 6 and 7.

In the topic of power quality, focus has been placed on the problem with damaging bearing currents in drive systems. In Chapter 10, a relevant model of the bearing currents in an IM will be provided together with a method for model parameter determination.

Chapter 2

HVAC loads in buildings

This chapter will describe the basic theory regarding pump and fan operation. In addition, an overview of pump assortment on today's market will be provided including sales statistics. Finally, different load profiles will be presented.

2.1 Pumps and fans as loads

This section will describe the load characteristics of pumps and fans. The operating characteristics of a pump and fan can be described by a Head-Flow,(H-Q), diagram seen in figure 2.1,[18]. The shape of the curve varies of course between different types of fans and pumps but are of minor importance for this illustration. Each curve in the diagram corresponds to a constant pump/fan speed and the steady state operating point will be defined at the intersection between the system curve and the pump/fan curve. The system curve represents the pressure drop in the system as a function of flow, where pressure drops arise from friction in pipes valves etc. In order to change the operating point, either the speed or the system characteristics needs to be changed. Figure 2.2 shows how a reduction of 50% in the flow, from Q_1 (point A) to Q_2, (B or B'), can be achieved. When the pump/fan speed is constant at n_1 the system characteristic needs to be changed in order to reduce the flow, eg using a valve, and the new operating point becomes B', (H_3,Q_2). If the system is kept unchanged and the the speed of the pump/fan is varied instead, the resulting operation point becomes B, (H_2,Q_2). It is evident that the power demand is much higher when the speed is kept constant. The affinity laws describes the relation between speed, head and flow and can be expressed as [18],

$$\frac{Q_1}{Q_2} = \frac{n_1}{n_2} \tag{2.1}$$

$$\frac{H_1}{H_2} = \frac{n_1^2}{n_2^2}. \tag{2.2}$$

As a result, the difference in power between two operating points can be expressed as

$$\frac{P_1}{P_2} = \frac{Q_1}{Q_2}\frac{H_1}{H_2} = \frac{n_1^3}{n_2^3}. \tag{2.3}$$

Hence, by reducing the speed by 50%, the power is theoretically reduced by 87.5% provided that the system curve is proportional to Q^2 which is the most common made assumption in the literature. The power difference between B' and B depends on the characteristics of the pump/fan, however the difference is always substantial.

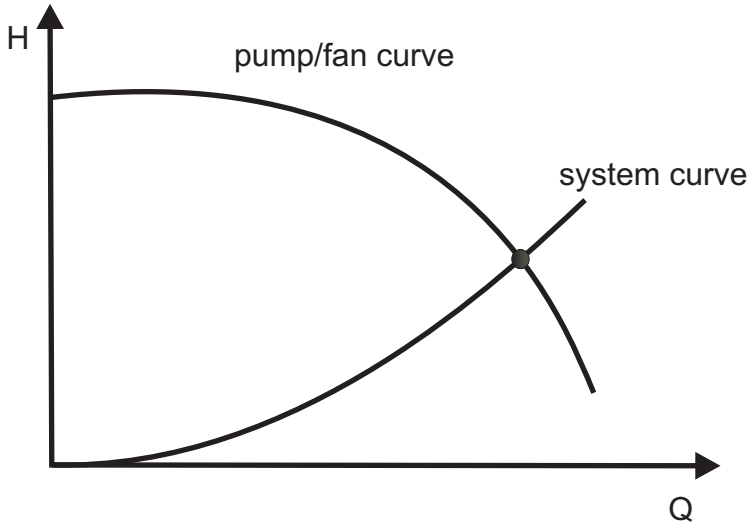

Fig. 2.1 Pump/fan characteristic for a given speed together with a system curve

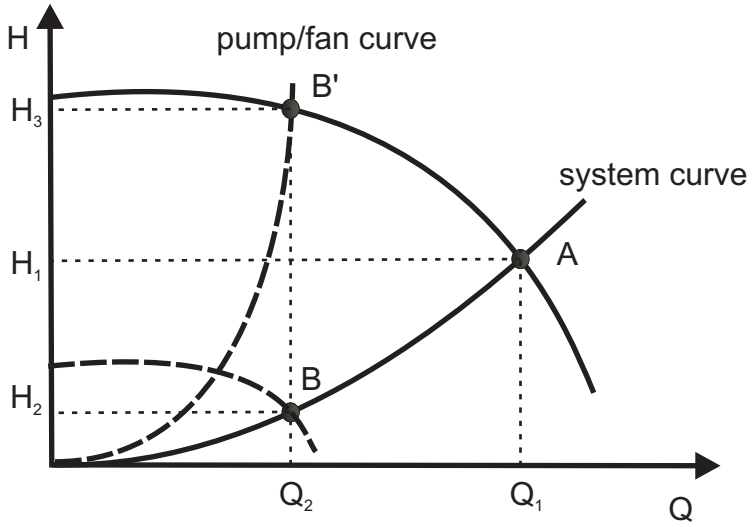

Fig. 2.2 Pump/fan characteristics for two different speeds together with two different system curves

2.1.1 Assortment of pumps and sales statistics

This section will focus on centrifugal pumps since this type is used in almost all pump applications in buildings. The information has been provided by contact with two manufacturers of pumps.

The pumps can be divided in two groups, canned type also called wet runner and dry rotor pumps. Wet pumps refers to pumps where the pumping liquid is in contact with the motor whereas the motor in a dry pump is completely separated from the pumping media. Wet pumps can be found in the power range up to 1.7kW, delivering a maximum head of 10-12m and a maximum flow of 50-60 m^3/h. Dry rotor pumps can be found for power ratings above 0.25kW.

The motors in wet pumps are either IM or PM motors and if they are equipped with a power converter this is always integrated with the pump. Dry motors are so far in principle only of IM type. They usually have an integrated frequency converter, when operated as a variable speed drive, but can also be equipped with an external converter supply.

Embedded functions

Variable speed pumps are usually controlled to be running at constant or proportional pressure which can be set in each individual pump. For larger pumps, it is possible to control the pressure and start/stop of the pump externally.

It is also possible to extract data from today's modern pumps. Parameters such as pressure, flow, electric power, total operating hours and total energy consumptions are often provided. However, smaller pumps, for residential buildings, does usually not have these additional functions.

Energy labels

Pumps in the power range $<$2.5kW are today labeled with an energy mark, (developed by Europump), A-G where A is the most energy efficient pump. This classification has been acknowledged by four of the major pump manufacturers in Europe which have a market share of 80% of the European market [19]. Table 2.1 shows the difference between the labels, where pump A, with index 0.4 consumes 40% energy, based on an annual load profile described in [19], compared to the reference pump with index 1. Label E is used as reference which corresponds to a constant speed IM circulation pump. Converter driven pumps using a PM motor usually falls under category A and variable speed IM usually falls under category B-D.

Sales statistics

Sales statistics have been provided from a large pump manufacturer. The data consists of sales numbers for Sweden in 2004 and 2005 on wet pumps, divided in three groups,

Table 2.1 Energy labels

Energy label	Index
A	<0.4
B	0.4-0.6
C	0.6-0.8
D	0.8-1.0
E	1.0-1.2
F	1.2-1.4
G	>1.4

constant speed pumps, (CSP), variable speed pumps (VSP) with IM and VSP using PM motors. The result is presented in Table 2.2.

Table 2.2 Sales statistics wet pumps

Type	2004 (%)	2005 (%)
CSP	94	93.4
VSP, IM	5.1	5.6
VSP, PM	0.9	1

Dry pumps are divided into two groups, CSP and VSP, and are presented in Table 2.3. It should be noted that dry pumps equipped with an external frequency converters are not accounted for in this statistic.

Table 2.3 Sales statistics dry pumps

Type	2004 (%)	2005 (%)
CSP	69.1	57.6
VSP, IM	30.9	42.4

2.2 Load profiles

This section will describe two basic load profiles obtained from the literature and two fictive profiles. The load demand refers to the demanded flow from a pump or fan. The torque demand can then be calculated using the affinity laws presented in Section 2.1 assuming that the efficiency of the pump and fan is constant. The load profiles presented in this section will be used for the saving potential analysis in Chapter 8. It should be noted that the profiles only show how a certain load can operate and that deviations can, and will, occur from case to case.

2.2.1 Load profile A

Load profile A describes a two level load operating at 100% for two thirds of the time and at 50% for one third of the time. This profile is can be found for Constant Air Volume system (CAV) using part time reduced flow [22]. Figure 2.4 shows the load demand and its annual distribution.

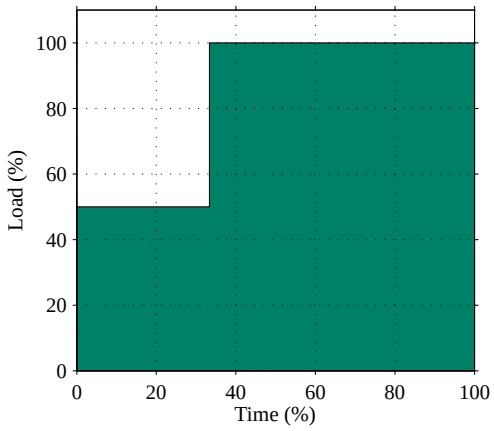

Fig. 2.3 Load profile representing a 100% load demand for 2/3 of the time and 50% 1/3 of the time (A).

2.2.2 Load profile B

Load profile B is taken from [23] and refers to a typical load profile for a Variable Air Volume system. Figure 2.3 shows the annual load demand.

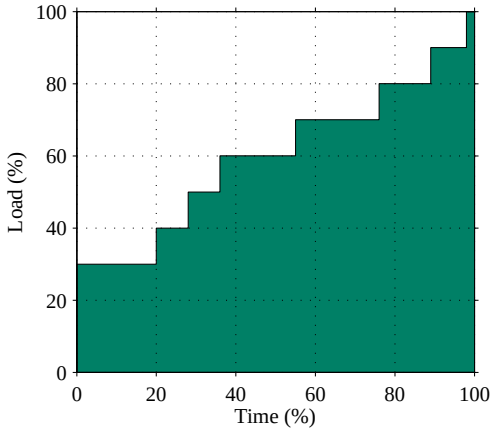

Fig. 2.4 Load profile representing a load profile for a VAV system. (B)

2.2.3 Fictive load profiles

Figures 2.5a and 2.5b shows load profiles C and D respectively. Profile C describes a load with 30% load demand for 80% of the time and 100% for 20% of the time. Load profile D describes a constant load demand.

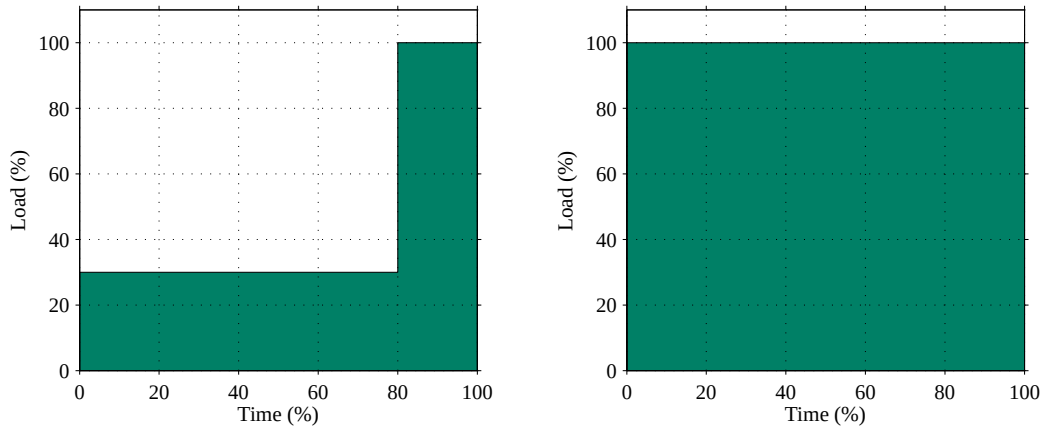

(a) Load profile with a low load demand during 80% of the time and 100% load demand 20% of the time (C).

(b) Load profile with constant power demand (D).

Fig. 2.5 Fictive load profiles

2.3 Dimensioning aspects

For each step in the derivation of a proper motor rating, a safety margin is added in order to guarantee the operation. As a result, over dimensioning of drive system becomes evident. The obvious consequence is of course a higher initial cost of the drive system. Furthermore, over dimensioning can, under certain circumstances, lead to decreased efficiency of the drive system resulting in a higher operating cost. The latter consequence will be further analyzed in Chapter 8.

Chapter 3

Drives for pumps and fans

This chapter will describe the different types of electric drives that are used for fan and pump applications. Furthermore, it also aims to give readers not familiar with electric drive systems, power electronics and power quality, enough insight in order to understand later chapters dealing with these concepts.

The basics of the Induction motor (IM) and Permanent magnet (PM) motors will be presented. Furthermore, frequency converter operation will be described followed by an introduction to EMC and power quality.

3.1 Induction motor

The Induction motor (IM) is the most widely used electrical motor today and can be found in all sorts of applications and power levels. The main advantage compared to other motor technologies is the possibility to connect the IM directly to the grid, without any additional power electronics.

Induction motors sold in EU are classified by an energy label eff1-eff3 where eff1 is the most energy efficient. This classification was introduced 1998 by the EU and CEMEP (the European Committe of Manufacturers of electrical Machines and Power electronics). The motors included in this classification are two and four pole IM in the range 1.1kW-90kW representing 75-80% of the European market [27]. The efficiency limits for 4-pole IM in the range 1.1-30kW can be seen in Table 3.1. The values are given for 75% of the rated load operation at rated voltage/frequency, (V/Hz).

The goal of CEMEP was to decrease the number of eff3 motor sales by 50% between 1998-2003. CEMEP had 36 members during this period, (eg ABB Siemens) which together sold 20 million units in Europe. The result was that, the eff2 label took most of the market share (86%, and eff1 8%). This can be explained by the increased cost of an eff1 motor, (20% higher compared to eff2), and that 80-90% are sold to OEM companies (original equipment manufacturer) [27].

Table 3.1 Efficiency limits for 4-pole IM at 75% of rated operation

kW	**Efficiency**, **eff3**	**Efficiency**, **eff2**	**Efficiency**, **eff1**
1.1	<76.2	≥76.2, <83.8	≥ 83.8
1.5	<78.5	≥78.5, <85.0	≥ 85.0
2.2	<81.0	≥81.0, <86.4	≥ 86.4
3	<82.6	≥82.6, <87.4	≥ 87.4
4	<84.2	≥84.2, <88.3	≥ 88.3
5.5	<85.7	≥85.7, <89.2	≥ 89.2
7.5	<87.0	≥87.0, <90.1	≥ 90.1
11	<88.4	≥88.4, <91.0	≥ 91.0
15	<89.4	≥89.4, <91.8	≥ 91.8
18.5	<90	≥90.0, <92.2	≥ 92.2
22	<90.5	≥90.5, <92.6	≥ 92.6
30	<91.4	≥91.4, <93.2	≥ 93.2

3.1.1 IM operation

The IM consists of a stator, (stationary part) and a rotor, (rotating part). The stator and rotor can be regarded as electromagnets consisting of a number of pole pairs. The stator consists of copper windings, sinusoidally distributed in order to create a sinusoidal magnetic flux wave when the motor is connected to a sinusoidal voltage. When a current is flowing in a winding, a magnetic flux is produced around the winding. If the IM has a balanced three phase winding, the net flux becomes constant in magnitude and will rotate at the same speed as the voltage frequency, ω_s (rad/s).

Assume now that the rotor is at stand still and a sinusoidal voltage is applied to the stator. A stator magnetic flux will now be created in the IM, crossing the air gap to the rotor. The rotating magnetic flux induces a rotor voltage perpendicular to the direction of the flux. As a result, a current is starting to flow in the rotor creating a force, acting on the rotor. The rotor will accelerate according to

$$J\frac{d\omega_r}{dt} = T_e - T_L \tag{3.1}$$

where J is the moment of inertia, ω_r is the rotor speed and T_e and T_L is the electromagnetic and load torque respectively.

A torque is produced as long as the stator flux is rotating relative to the rotor. Hence, when no load is applied to the IM the speed will increase until $\omega_r = \omega_s$.

When the IM is loaded, w_r decreases slightly in order for the IM to create the electromagnetic torque needed for the applied load. The difference in speed is called the slip speed which at rated operation is in the rage of 1-5% of ω_s depending on motor size, for motor ratings approximately above 200kW the slip is <1%.

Figure 3.1a shows the torque speed diagram for an IM together with a load character-

istic. The operating point will be in the intersection of the two curves. In order to change the speed the load curve or the IM curve has to change.

Figure 3.1b shows the torque speed diagram, for three fixed setup of voltages and frequencies. An important relationship regarding the operation of an IM is the ratio of the voltage and frequency (V/Hz) which is proportional to the flux produced in the motor. Furthermore, the maximum torque is proportional to the flux. As a result, by keeping the V/Hz constant, the rated torque will be produced by the same current magnitude which results in a constant rated torque as can be seen for the fist two T-ω curves in figure 3.1b. However, when the frequency is increased above a certain limit, in this case the synchronous speed ω_{s2}, the voltage will be constant due to the limitations of the frequency converter, and also due to the voltage rating if the IM. The motor is now running in its so called field weakening region which results in a lower rated torque, (operation in the field weakening region is more common in automotive applications).

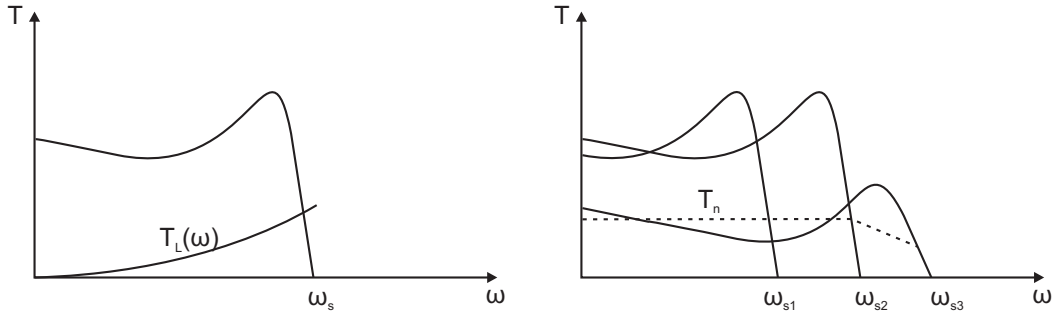

(a) Toque speed characteristics of an IM for a given voltage/frequency

(b) Torque speed characteristics of an IM for different voltage/frequency setups

Fig. 3.1 Torque speed diagram of an IM

3.1.2 Loss components

The efficiency of an IM is relatively high when running at its optimal operating point, which usually is located around 75% of its rated load, but can decrease substantially from its optimum at light load. This gives an opportunity to optimize the control of the IM in order to minimize the losses at each operating point which will be discussed more in detail in Chapter 6.

The different losses that occur in an IM are the following:

- Resistive losses
- Core losses
- Mechanical losses

- Harmonic losses
- Stray losses

The stator and rotor losses are represented by the resistive losses in the stator and the rotor windings. These losses constitute 55-60% of the total losses, according to [20] (not including the losses due to harmonics).

The mechanical losses produced in the IM are friction losses in the bearings and losses caused by the cooling fan, (if a fan cools down the motor); these losses contribute with 5-10% of the total losses [20].

Furthermore, the hysteresis and eddy currents in the core of the stator and the rotor cause core losses. This loss component contributes to approximately 20-25% of the total losses [20].

The harmonic losses are produced from the harmonics in the supply voltage and currents, which do not contribute to the mechanical output power. The amount of harmonics depends on the characteristics of the frequency converter.

Finally, the stray losses are the losses that are not accounted for by the other losses discussed above. These losses constitute 10-15% of the total losses [20].

These values are naturally dependent on load, motor size, motor design etc.

3.2 Permanent magnet motors

Permanent magnet motors have become more popular recent years due to cost reduction in PM material and its high efficiency also at low load, high power density and high dynamic performance.

All PM motors fall under the category of synchronous motors, which will be explained in the oncoming section. Usually power electronics is needed in order to operate the PM motor, accordingly a converter is needed to operate the motor.

This thesis will focus on a type of PM motor often referred to as Brush Less DC motors (BLDC), in addition it will also reflect on the differences regarding sinusoidally commutated PM motors, here after referred to as PMSM. The focus here has been placed on the BLDC type due to its advantage design and manufacturing, resulting in lower cost, as well as in control simplicity compared to a PMSM. It should be noted that the BLDC has a reduced dynamic performance compared to the PMSM. However, high dynamic performance is not needed in HVAC applications. Moreover, improvements in power electronics have made the BLDC an interesting competitor to the PMSM. As a result, the trends point to a wider use of BLDC motors compared to PMSM motors for loads with low dynamic performance such as pump and fans, [28, 29, 30].

3.2.1 Brush Less DC motors and PMSM

BLDC motors, also referred to as EC and BLCM in the literature, differs from PMSM in its construction and the commutation of the currents. The stator windings in a BLDC motor are equally distributed in contrast to the PMSM (and IM) which have sinusoidally distributed windings. Furthermore, the rotor magnets are also different in order to create a trapezoidally induced voltage in the stator windings, called back emf which can be seen in figure 3.2.

Figure 3.3 shows a 2 pole BLDC motor. The rotor consists of one permanent magnet creating two poles. The stator consists of three phases displaced by 120°. Each phase are equally distributed 60° on each side of the stator.

Consider phase a in figure 3.3a, assuming the rotor speed, ω_r, to be constant. The back emf in the a-phase winding are now at its maximum since all windings are enclosed by the rotor magnet. Its magnitude can be written as

$$E_a = k_e \omega_r \tag{3.2}$$

where k_e is the motor constant. It can be noted that the induced voltage will remain constant in the interval $0<\theta_r<120^\circ$. At θ_r=120° the winding edges will be ”cut” by the north pole and the south pole respectively, shown in figure 3.3b. As a result, the induced voltage will reduce linearly until the winding are enclosed by the magnets once more. The polarity of the induced voltage is now opposite from before. The same reasoning can be

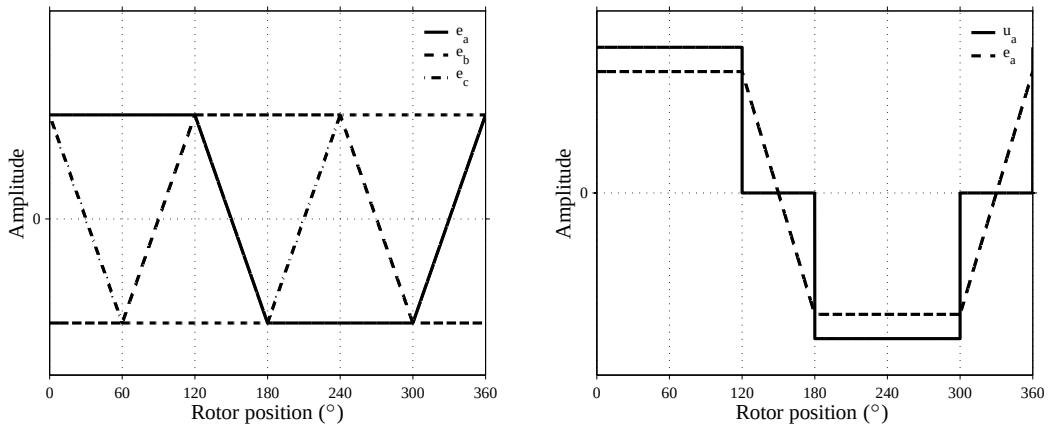

(a) Ideal back emf for all three phases (b) Back emf and phase voltage for phase a

Fig. 3.2 Ideal emf and voltage for a BLDC motor

done for all three phases and for an arbitrary number of pole pairs, the ideal back emf can be seen in figure 3.2.

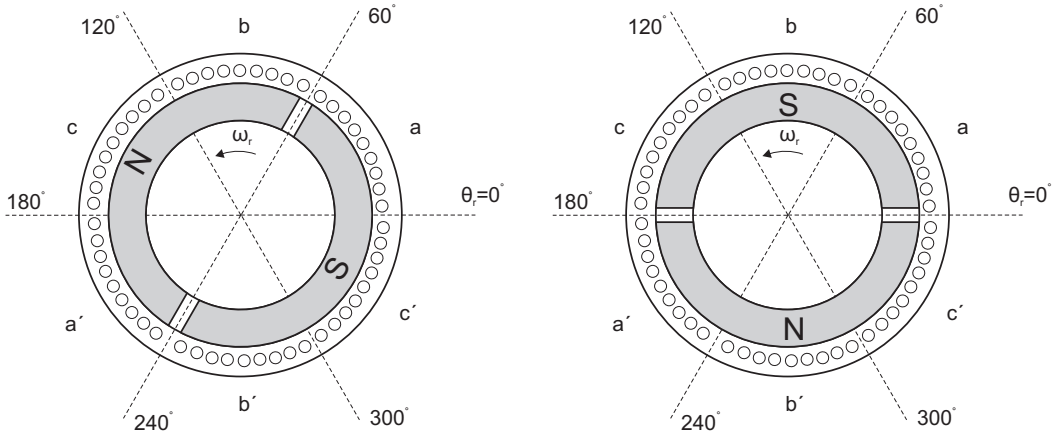

(a) The a winding are now enclosed by the magnet, creating the maximum induced voltage.

(b) The induced voltage in phase a will now decrease linearly for the next 60°

Fig. 3.3 Cross section of a 2-pole BLDC motor

The phases must now be exited in order to create a constant electromagnetic torque, T_e. T_e can be expressed as

$$T_e = \frac{e_a i_a + e_b i_b + e_c i_c}{\omega_r} \tag{3.3}$$

where ω_r is the mechanical rotor speed. It is evident, from (3.3), that it is desirable to keep the phase currents constant when the back emf is kept constant in order to have a constant torque.

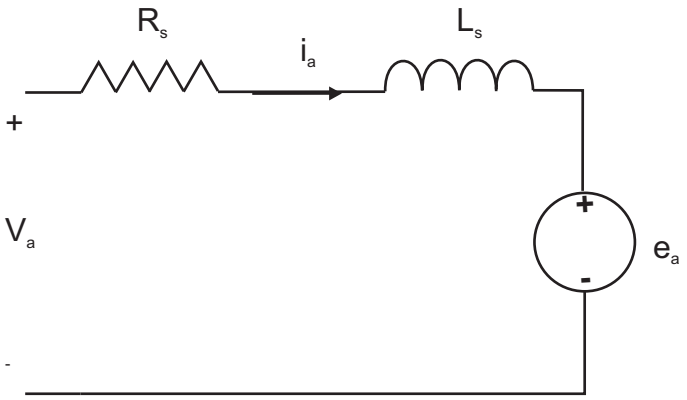

Fig. 3.4 Equivalent circuit of a BLDC.

Hence the phases will be excited according to figure 3.2b. T_e will now ideally become constant. However, due to the inductance in the motor, the phase currents will not decrease to zero or increase to its desired value at the same time instant as the phase voltage is turned off or on. This will result in a ripple in the torque which is one of the problem related to BLDC motors. The interested reader can find more details regarding the excitation of a BLDC in [35].

The difference in commutation when the windings are sinusoidally distributed are that it is not longer possible to keep the simple control of the voltage. Since the back emf now is sinusoidal, the applied voltage needs to be sinusoidal in order to produce a constant torque, which in turn makes the control more complex. Furthermore, the rotor position needs to be known all the time which also increases the complexity.

Figure 3.4 shows an equivalent per-phase circuit of the BLDC motor at steady state operation, (constant applied voltage, constant back emf and constant current). The steady state expression of the stator voltage can be expressed as, (ideally di/dt=0 at steady state)

$$V_a = I_a R_s + E_a = I_a R_s + k_e \omega_r \tag{3.4}$$

Since the commutation of the motor only depends on the rotor position it is not possible to increase the speed using faster commutation. Hence, in order to vary the rotor speed, the stator voltage magnitude needs to be changed. As a result, the rotor speed is proportional to the magnitude of the stator voltage. Furthermore, due to limitations in the voltage magnitude from the supply and allowed maximum current and voltage of the motor, the operating range can be described by figure 3.5. The maximum torque is decreasing with increasing speed since the emf comes closer to the maximum voltage, dc link voltage, which makes it impossible to maintain the current at the desired level.

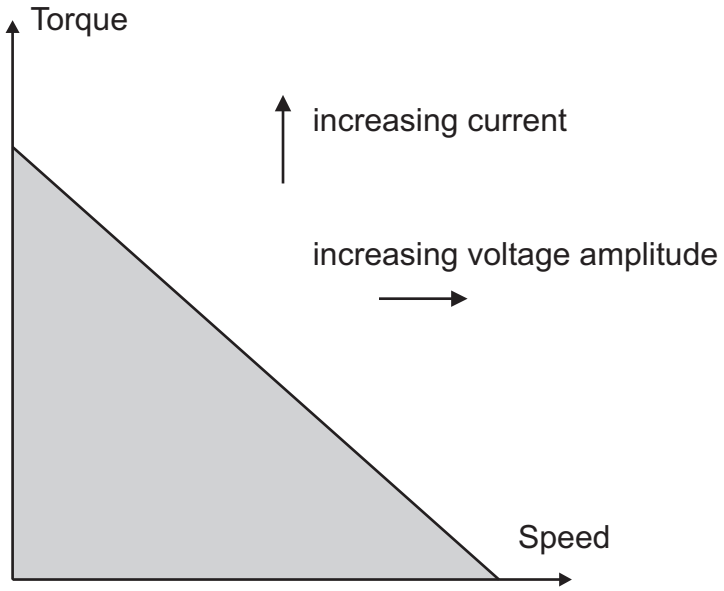

Fig. 3.5 Torque speed diagram of a BLDC motor

3.2.2 Loss components

Since the rotor of a BLDC/PMSM motor consist of permanent magnets, creating the rotor flux, the rotor current will be negligible. As a result, the rotor losses are assumed to be zero. The remaining losses are same as for the IM but different in magnitude. The power factor (PF) of a permanent magnet motor is higher then the an IM of similar rating since less magnetizing current, (less reactive power), is needed for magnetization. Often, the magnets can provide the complete magnetization of the motor. Hence, for a given output power, increased PF results in decreased current amplitude which in turn gives lower resistive losses in the motor.

The efficiency of PMSM/BLDC motors are more constant as a function of load compared to the IM where the efficiency drops quite rapidly with decreasing load as explained in Section 3.1. This can also be explained by the PF since the reactive current component in an IM is much larger and more or less constant, while the active current component is decreasing. As a result, the relative losses will increase with decreasing load (decreasing active current).

It is difficult to draw any conclusions between the difference in efficiency between a PMSM and a BLDC motor and this theme has not been treated further in this thesis. Studies have been made in order to determine the difference, [21], but it was not possible to make a general efficiency distinction between the to motor types.

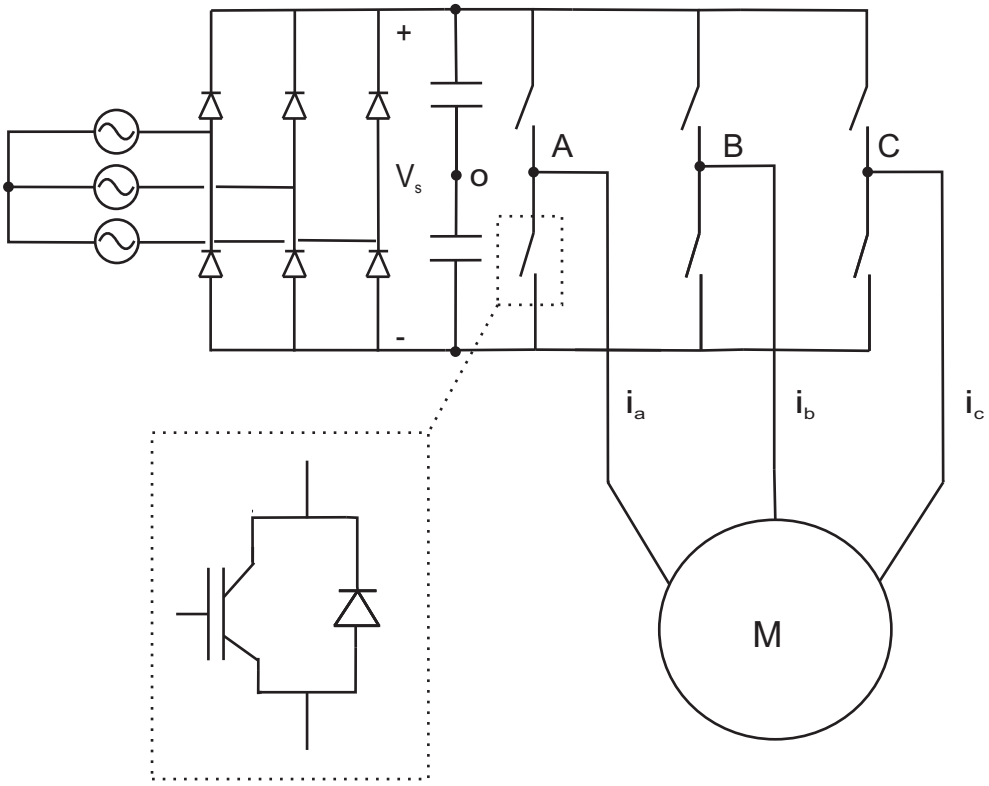

Fig. 3.6 Three phase frequency converter with a motor load

3.3 Frequency converters

In order to best change the speed of an IM and to operate a PM motor, a frequency converter is needed. Figure 3.6 shows a schematic diagram of a three phase frequency converter. The rectifier stage, which in this case consists of diodes, rectifies the grid voltage, v_r, v_s v_t. In order to create a stable DC voltage after the rectifier, a capacitor is connected in parallel. This part is called the DC link of the converter. The inverter, consisting of transistors can now be controlled in order to provide the motor with an arbitrary voltage and frequency.

By turning the transistors in each inverter leg on and off quickly, (several kHz), changing the output, (point A, B and C in the figure), from $\pm V_{dc}$, and by controlling the width of each pulse, a sinusoidal, (in average), voltage can be created. This technique is called Pulse Width Modulation (PWM). Figure 3.7 shows one leg of the frequency converter and the pulse pattern during one half of the fundamental period. It should again be pointed out that in the figure the switching frequency is fairly low in relation to the fundamental wave in order to illustrate the operation. During the time interval t_0-t_1, T_2 is on and the negative DC bus voltage is applied to the load. The current will flow through either D_2 or T_2, depending on the direction of the current i_a, shown in figure 3.8. If i_a is negative the current goes through the transistor otherwise through the freewheeling diode. At the time instant

t_2, T_2 turns off and T_1 turns on. The direction of i_a determines which component of T_1 and D_1 that will start to conduct. T_1 is now on during the time interval t_1-t_2. The resultant sinusoidal voltage can be seen in figure 3.7. The time duration of each pulse is determined by the reference voltage and it can be noted that the positive pulse width increases as the amplitude of the voltage increases.

The different loss components present in the converter are conductive losses and switching losses. The switching losses occur in two of the four components at each switching instant depending on the direction of the load current. Four cases are possible, also shown in figure 3.8:

T2 turns on (T1 turns off)

i_a is positive, results in turn off losses in T1 and turn on loses D2, (case 1).

i_a is negative, results in turn off losses in D1 and turn on lossesT2, (case 2)

T1 turns on (T2 turns off)

i_a is positive, results in turn off in D2 and turn on losses T1 (case 3)

i_a negative, results in turn off losses in T2 and turn on losses in D1 (case 4)

One special case occurs when i_a is zero, which results in zero switching losses. The switching losses can now be estimated using the switching characteristics presented in Section 3.3.2.

Details regarding the control of the frequency converter is described in Chapter 6.

The following subsections will describe the different loss components present in a frequency converter. The basic operation and physical structure of the most commonly used semiconductors in frequency converters are also provided in order to understand the different losses.

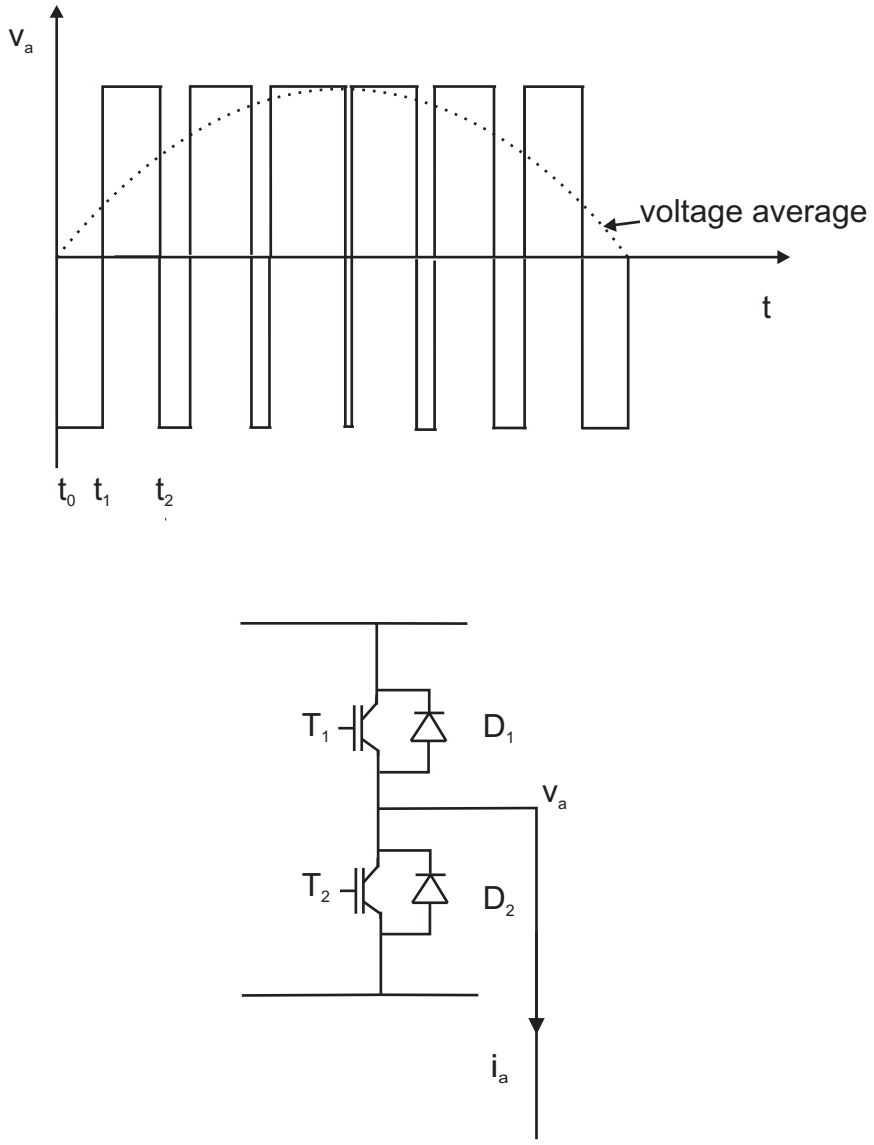

Fig. 3.7 Pulse pattern of one phase during half of the fundamental period

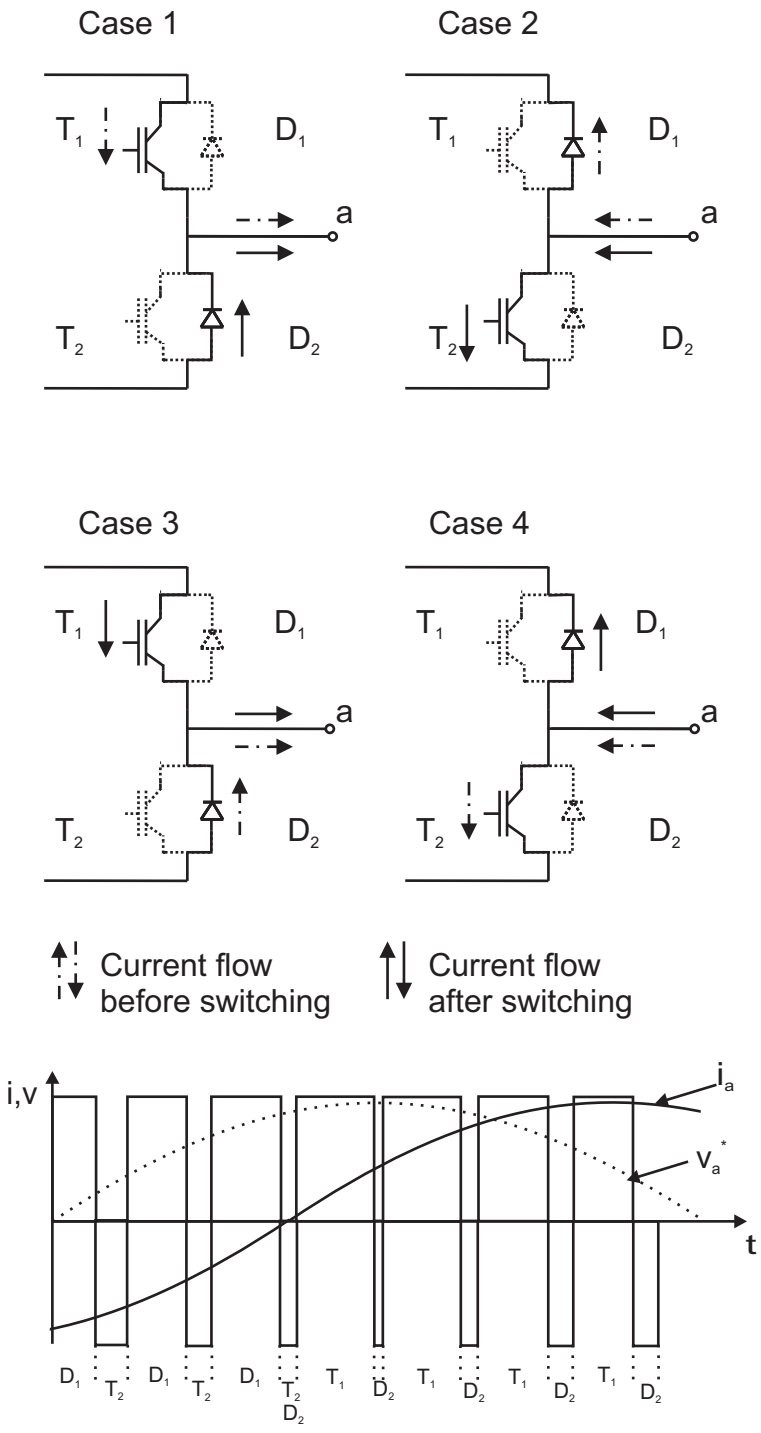

Fig. 3.8 Four cases of switching transitions

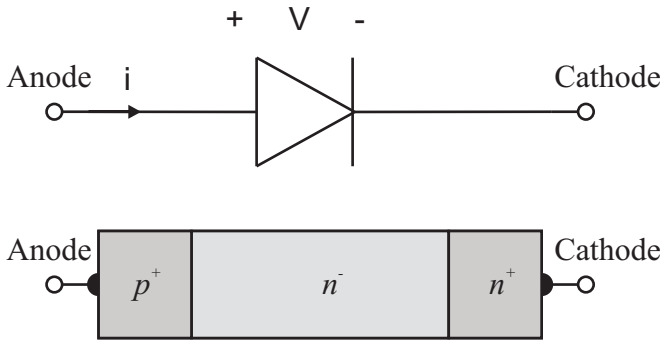

Fig. 3.9 Circuit symbol and the physical structure of a power diode.

3.3.1 Power Diodes

Power diodes have different physical structure and operational characteristics compared to low power diodes. However, the basic operating principle are the same, namely that the diode blocks the current when a reverse voltage is applied across the diode and conducting when the voltage over the diode is positive. Figure 3.9 shows the circuit symbol and the physical structure of the device. The difference compared to a low power diode is the n^- layer which is a region consisting of a lightly n-doped silicon material. The thickness of the n^- region decides how large reverse voltage the diode can withstand before it reaches its breakdown voltage. When the diode is conducting the voltage drop is approximately $V+R_{on}I$, where V is in the range of 0.8-1V and $R_{on}I$ is in the range of 1V at rated current. This can be compared to a low power diode which has a more constant voltage drop at its on-state. The magnitude of the voltage drop also depends on the dimensions of the diode. If the reverse blocking capability is increased, an increased length of the n^- layer will result, and the on-state voltage drop will increase. The losses in the diode comes mainly from conductive losses but also in some extent from switching losses.

Schottky Diodes

A Schottky diode is is a metal semiconductor junction consisting of a thin film of metal in contact with a semiconductor, usually Si. The advantage compared to a pn junction diode is the decreased voltage drop at on-state and the decrease of the recovery transitions, resulting in lower power dissipation and in addition also decreases the emitted electromagnetic interference (EMI). However, the reverse blocking capability is limited to a maximum of 250V for Si based Schottky diodes, [26], which makes it unsuitable for use in frequency converters. In order to increase the reverse blocking capability SiC can be used instead. The interested reader can find more detailed information in [25] and [26].

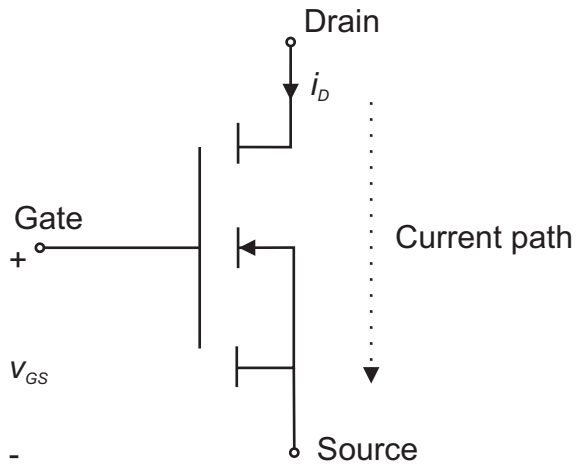

Fig. 3.10 Circuit symbol for an n-channel MOSFET

3.3.2 MOSFETs

Power MOSFET transistors are today the most commonly used transistor for blocking voltages up to a DC-level of 600V [26], corresponds to a three phase AC voltage of less then 400V. The advantages of the MOSFET compared to its counterparts are high switching speed and low gate drive power consumption. The current through the MOSFET is controlled by the gate voltage. Figure 3.10 shows the circuit symbol where v_{GS} and i_D denotes the gate-source voltage and the drain current respectively.

Figure 3.11 shows the physical structure of a n-channel MOSFET cell. Usually many cells are packed together in parallel in order to increase the current capability. The drain and source consists of an aluminium metallization grown on the drain n-region and across the pn material at the source. Between the two source terminals an isolated dielectric material is grown, isolating the gate from the source. When a positive gate voltage is applied, with respect to the source, an n-channel is formed between the drain and source, due to an accumulation of electrons, and the MOSFET is turned on. The thickness of the n-channel depends on the magnitude of the gate voltage. So, in principle, the MOSFET operates as a valve, where the Gate voltage determines how ”open” the valve is.

Figure 3.12 shows different operating states of a MOSFET for different v_{GS} where $v_{GS4}>v_{GS3}>v_{GS2}>v_{GS1}$. When the MOSFET is in its on-state it is operated in the ohmic region. It can be noted that, as v_{GS} is increased i_D increases, for a constant v_{DS}. Hence, by increasing the gate voltage the on-state voltage drop decreases for a constant current.

The idealized switching characteristics of one leg in a frequency converter, described in figure 3.13, using a MOSFET can be seen in figure 3.14. The load current is assumed to be of constant magnitude, I_{load} during this very short time period, less then 1μs. Hence, the load current is freewheeling trough the diode prior to the MOSFET turn on. At turn on, a positive gate-source voltage is applied and at time t_0 the gate voltage has reached the threshold voltage V_{th} which is the voltage level when the current starts to rise. The

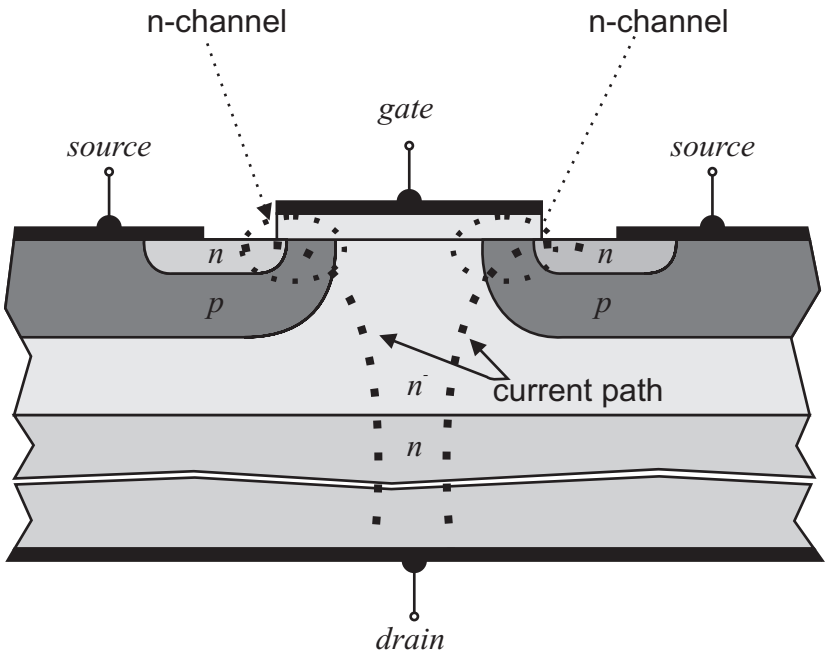

Fig. 3.11 Physical structure of cell in a power MOSFET.

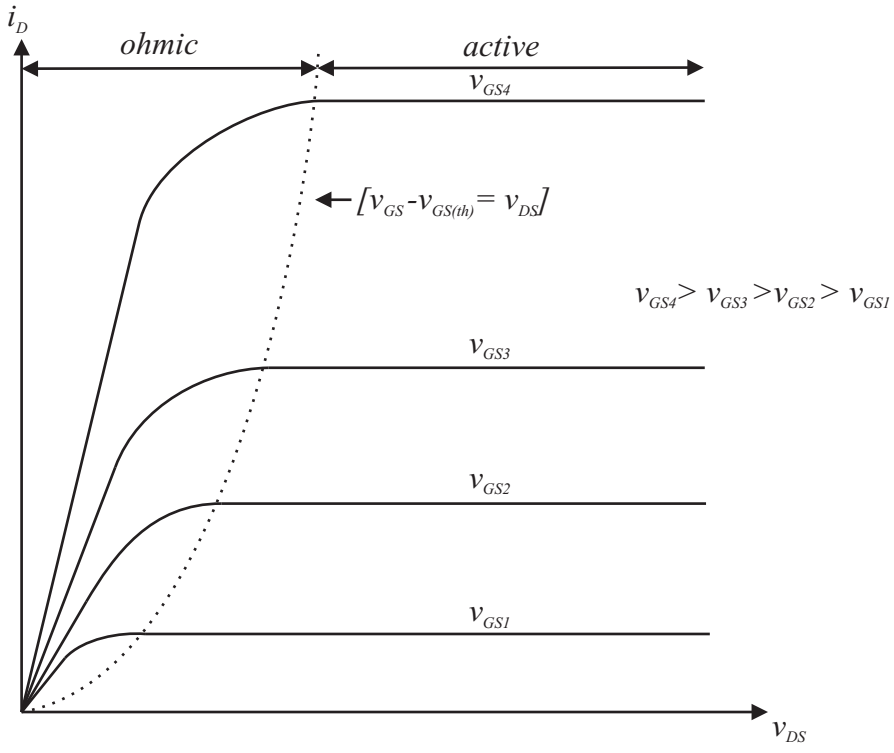

Fig. 3.12 I-V caracteristics of an n-channel MOSFET for different v_{GS}

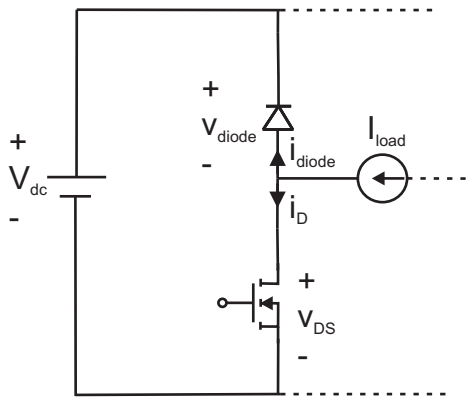

Fig. 3.13 Circuit diagram of the active components in one leg in a converter, valid for negative load current

voltage across the MOSFET will remain at its high value as long as the freewheeling diode is conducting. When the current in the MOSFET has reached I_{load} and accordingly the diode current comes to zero, the diode turns off and the voltage starts to increase over the diode and decrease across the MOSFET. At turn off of the MOSFET, the gate voltage applied to the gate is reduced to zero. The following time intervals shows the reverse characteristics as was described at turn on.There are some more important non-ideal characteristics for this switch procedure, and the interested reader can find more details in [25]. Details regarding how the stray inductance in the circuit gives over-voltage and how the discharge of the n-region results in recovery of the components is described in detail.

One important thing to point out is that in the reverse direction, the power MOSFET act as a diode, observe the p-n from drain to source. In the type of MOSFET transistor used in this work it is important to avoid that this diode turns on, which gives a circuit complication, as shown later.

3.3.3 IGBTs

An Insulated Gate Bipolar Transistor (IGBT) is the most commonly used transistor for high voltage applications from 400VAC and upwards. The physical structure of an n-channel IGBT is shown in figure 3.15. There are also different types of IGBTS having slightly different characteristics. By adding a n^+ layer between the p and n^- layer, often referred to as a non-punch-through IGBT, the switching speed can be increased. However, the on-state voltage drop will increase, the interested reader can find a detailed description of different IGBTs in [24].

The drawback of the IGBT compared to the MSOFET is the switching speed which is lower for the IGBT.

The hard switched voltage and current waveforms for the IGBT are similar to those of

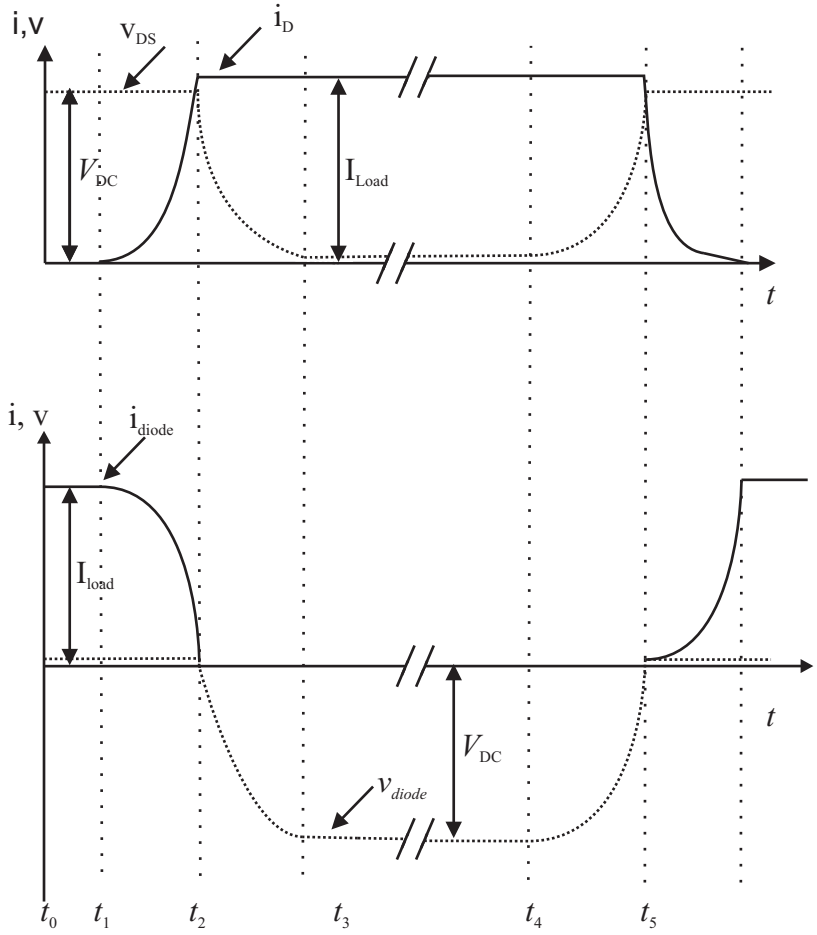

Fig. 3.14 Turn on and off characteristics of the MOSFET and diode with an inductive load

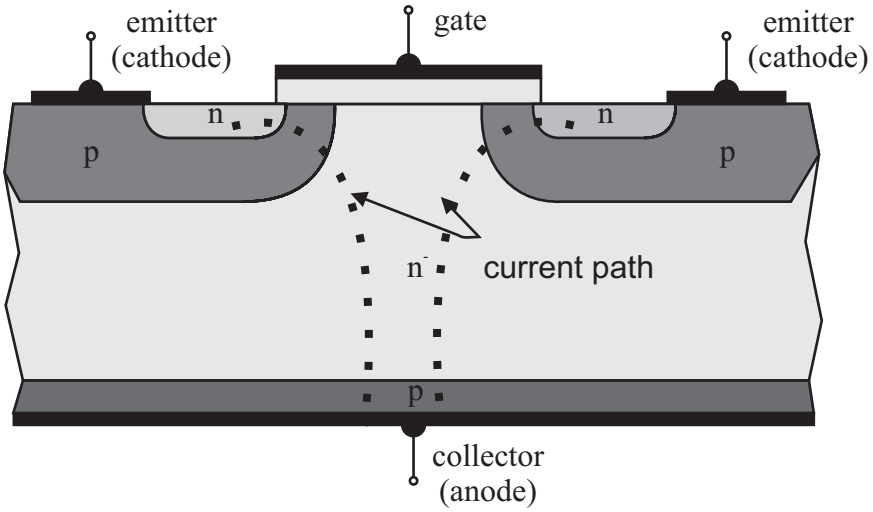

Fig. 3.15 Physical structure of an IGBT

the MOSFET. The main difference is that the current trough the IGBT at turn off decreases slowly at the end of the transition. This is often referred to as current tailing which makes the IGBT slower than the MOSFET.

3.4 EMC and power quality

All electronic devices emit electromagnetic noise. This radiation is a side-effect of the basic operation of the device, worsened by parasitics as stray inductances and recovery of components. The emissions from one device can interfere with other devices, causing potential problems. These emissions are called ElectroMagnetic Interference (EMI) and are today an important issue in the design of electronic systems.

Electromagnetic compatibility (EMC) refers to the ability of an electric device to operate without emitting levels of EM energy that cause EMI in other devices in the surrounding area, nor being affected by its EM surroundings.

The increased use of power electronics in todays drive system can result in problems regarding EMC issues [37]. The drive system themselves are vulnerable to disturbances and they emit EM disturbances. Several issues needs to be considered when power electronics are introduced. Firstly, the motor conditions changes. The motor are now fed with a non ideal waveform which results in higher losses, larger current, voltage spikes on the motor terminal and increased risk for bearing currents. Hence, the lifespan of a motor which is not designed as a variable speed drive (VSD) can be reduced. Furthermore, other equipment in the vicinity can be negatively affected by the VSD due to conductive- and/or radiated interference.

3.4.1 Basic power quality concepts

This section will show how a VSD differs from the desired ideal load. Figure 3.16 shows an example of an ideal voltage and current feeding a load. The voltage and current are in phase and sinusoidal, containing only one frequency component, referred to as the fundamental component. However, this is only valid for a purely resistive passive load. Power electronic loads on the other hand is far from an ideal resistor. Figure 3.17 shows the line current of a three phase converter of a VSD pump. By looking at the frequency content of this current it can be noted that large amounts of different frequency components are present, where the components with frequencies above the fundamental frequency is referred to as harmonics. Hence, harmonics are sent back to the power distribution network where they can cause a distortion in the supply voltage to other equipment, increased losses in transformer station, capacitor failures, and disturbance in power line communications.

In order to quantify how a load draws power from the grid different quantities are defined. The displacement power factor, DPF, is defined as

$$DPF = cos(\varphi_1) \tag{3.5}$$

where φ_1 is the phase angle between the fundamental current and voltage. The DPF equals to 1 for the ideal case. Note that the DPF does not include any information regarding the

harmonic content in the voltage or current. The power factor, PF, is defined as

$$PF = \frac{V_{s1} I_{s1}}{V_s I_s} cos(\varphi_1) \tag{3.6}$$

where V_{s1} and I_{s1} denotes the fundamental voltage and current respectively and V_s, I_s denotes the total voltage and current component. Often the PF is defined assuming an ideal voltage resulting in a cancelation of the voltage component in the expression. A further common quantification of voltage and current distortion is Total Harmonic Distortion, THD, defined as

$$\%THD_i = 100 \sqrt{\sum_{h \neq 1} \frac{I_{sh}^2}{I_{s1}^2}} \tag{3.7}$$

$$\%THD_v = 100 \sqrt{\sum_{h \neq 1} \frac{V_{sh}^2}{V_{s1}^2}}. \tag{3.8}$$

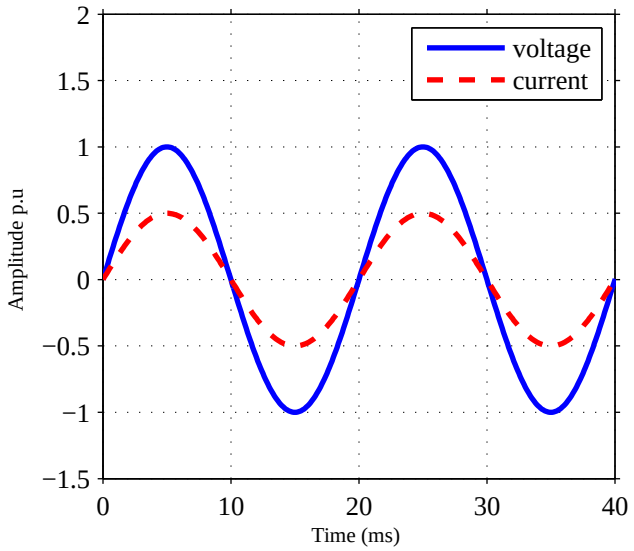

Fig. 3.16 Ideal voltage and load current

3.4.2 Coupling mechanisms

There are different coupling paths between a source and a victim, where the victim refers to the affected device due to EMI caused by the source. The most obvious path is through the point of common coupling (PCC), but there are also other coupling mechanisms. When two conductive materials A and B, are isolated from each other there is always a stray capacitance connection between them as can be seen in figure 3.18, showing two

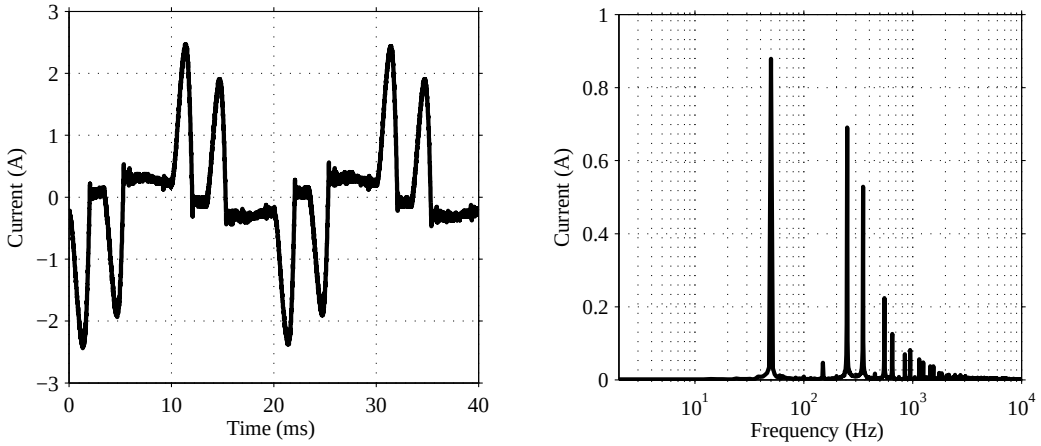

(a) Line current of a three phase converter of a VSD pump

(b) Frequency contend of the current

Fig. 3.17 Example of a current drawn by a non ideal load, in this case a three phase frequency converter

cables referred to as A and B. The size of the stray capacitance depends on the distance, the separating medium and the area of A and B. Since the impedance of a capacitance decreases with increasing frequency, the possible risk of EMI increases as the frequency content in the current increases. Problems related to stray capacitances are damaging bearing currents in IM which will be further analyzed in Chapter 9.

Another coupling mechanism is inductive coupling. When a current, i_A flows in cable A in figure 3.18, a magnetic field is created around the cable, L_A and L_B is referred to as the stray inductance in the cables. A part of the magnetic field is also crossing cable B causing a current to flow in cable B counteracting the magnetic field, according to Faraday's law. The amount of coupling between the cables are often denoted by mutual inductance, M, and depends on the distance between the cables and the stay inductance in the cables. It can also be noted that the coupling is dependent on the angle of the coupling magnetic field. As a result, the coupling is maximum when the cables are in parallel and zero when they are perpendicular to each other.

Today's modern VSD are using fast switching elements, creating high frequency components. The high speed of the switching transitions causing large dv/dt. As a result, possible problems with EMI can be present. Figure, 3.19 shows a simple example of a voltage pulse with two voltage slopes and figure 3.20 shows their frequency content. It can be noted that the increase in dv/dt and hence the increase in speed of a device increases the high frequency content, and hence, increases the potential risk of EMI.

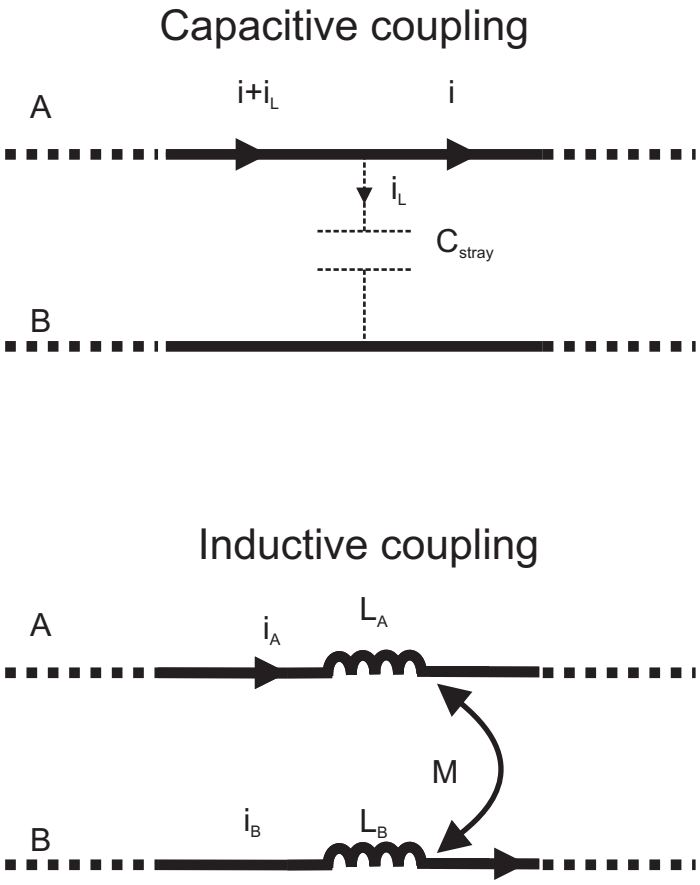

Fig. 3.18 Capacitive and inductive coupling

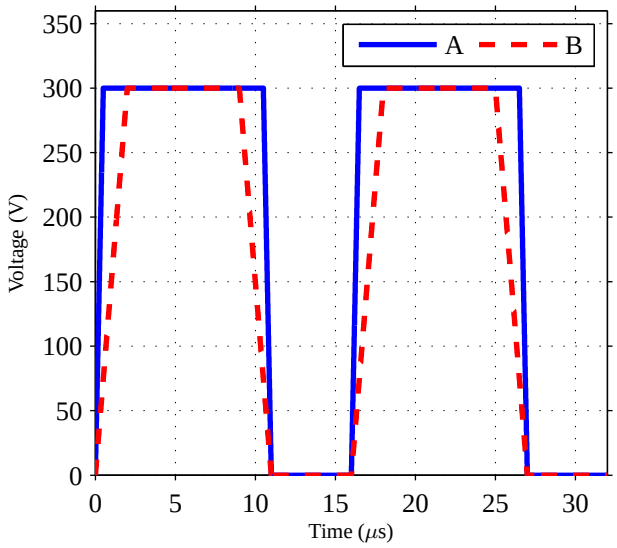

Fig. 3.19 Voltage pulses with different dv/dt slopes

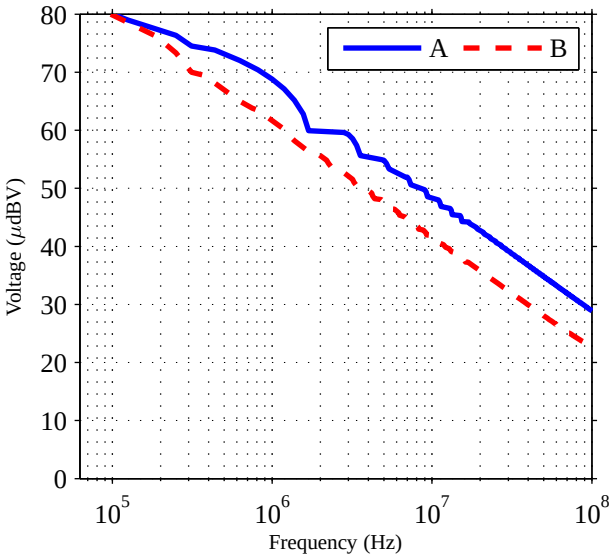

Fig. 3.20 Frequency content for two voltage pulses with different dv/dt slopes

Chapter 4

Modeling of electrical drive systems

There are many different types of motor models presented in the literature. This chapter will present the models used in this work and motivate why these have been chosen. The overall goal is to model the losses in a drive system as accurate as possible. Due to the relative complex nature of the losses in drive systems, it is not possible to account for all factors. However, it will be possible to identify trends between different control schemes and motor designs. Both dynamic modeling and stationary modeling is used.

4.1 Induction motor

4.1.1 Dynamic modeling

Dynamic models are for apparent reasons more complex than stationary models. Furthermore, the efficiency at stationary conditions are of interest since HVAC applications are assumed to operate at constant load demand for time durations that are much longer than the transient transitions. In order to estimate the converter loss components, the motor current at each switching instant needs to be known. Hence, a dynamic model is more convenient which makes it easy to determine the instantaneous current magnitude at each switching instant.

A dynamic Matlab Simulink ® model of the IM used for the purpose of estimating the switching losses in a frequency converter and compare different switching schemes will be considered. As a result, the IM model will be made as simple as possible, not containing iron losses nor stray or mechanical losses.

The derivation of the IM equations are well documented in the literature [33] and will therefore only be described briefly. It is assumed that the IM has a balanced three phase winding. The stator and rotor voltages can be expressed as

$$\mathbf{v}^s_{abcs} = R_s \mathbf{i}^s_{abcs} + \frac{d}{dt}\mathbf{\Psi}^s_{abcs}, \tag{4.1}$$

$$\mathbf{v}^s_{abcr} = R_r \mathbf{i}^s_{abcr} + \frac{d}{dt}\mathbf{\Psi}^s_{abcr} \tag{4.2}$$

where the stator and rotor voltages are denoted by $\mathbf{v}_{abcs}$, $\mathbf{v}_{abcr}$ and the stator and rotor fluxes $\mathbf{\Psi}_{abcs}$ and $\mathbf{\Psi}_{abcr}$ respectively. The superscript s refers to the reference frame which in this case is the stationary reference frame.

The flux is defined as

$$\Psi = Li \tag{4.3}$$

which gives the following expression for the derivative of the flux

$$\frac{d}{dt}\mathbf{\Psi} = \frac{d}{dt}(\mathbf{L}\mathbf{i}) = (\frac{d}{dt}\mathbf{L})\mathbf{i} + \mathbf{L}(\frac{d}{dt}\mathbf{i}). \tag{4.4}$$

Since the inductance in the IM is a function of the rotor position it is more convenient to express the derivative as

$$\frac{d}{dt}\mathbf{L} = \frac{d\Theta}{dt}\frac{d\mathbf{L}}{d\Theta} = (\frac{d\mathbf{L}}{d\Theta})\omega_r. \tag{4.5}$$

where Θ is the electrical rotor position and ω_r is the electrical rotor speed. The equations can now be written on the following general form

$$\mathbf{V} = \mathbf{R}\mathbf{i} + \frac{d}{dt}\mathbf{L}\mathbf{i} + \mathbf{L}\frac{d\mathbf{i}}{dt} = (\mathbf{R} + \frac{d}{dt}\mathbf{L})\mathbf{i} + \mathbf{L}\frac{d\mathbf{i}}{dt} \tag{4.6}$$

The next step is to express the inductance in the motor. All windings are coupled to each other where M_{xy} defines the mutual inductance in phase x caused by the current in phase y. Since the IM is symmetrical it is assumed that the expression for the inductance in each phase are equal. The mutual inductances between two stator windings, displaced 120 degrees, can be expressed as

$$M_{xy(s)} = M_s \cos(\Theta) = M_s \cos(2\pi/3) = -0.5M_s \tag{4.7}$$

where M_s is the mutual stator inductance. It should be noted that the magnetizing inductance, L_m, in the equivalent circuit of the IM is not the same as M_s. The relation between the two quantities are

$$M_s = 3/2L_m. \tag{4.8}$$

This term is a result from the derivation of the equivalent circuit, for details refer to [33].

The inductance matrix for the stator can now be expressed as

$$\mathbf{L}_{ss} = \begin{pmatrix} M_s + L_{s\sigma} & -0.5M_s & -0.5M_s \\ -0.5M_s & M_s + L_{s\sigma} & -0.5M_s \\ -0.5M_s & -0.5M_s & M_s + L_{s\sigma} \end{pmatrix}. \tag{4.9}$$

The leakage inductance for each phase does not contribute to the coupling.

The coupling between the stator and rotor windings are a bit more complex since the mutual inductance depends on the rotor position. The mutual inductance matrix, $\mathbf{L}_{sr}$, can be expressed as

$$\mathbf{L}_{sr} = \begin{pmatrix} M_{sr}cos(\Theta) & M_{sr}cos(\Theta + \frac{2\pi}{3}) & M_{sr}cos(\Theta + \frac{4\pi}{3}) \\ M_{sr}cos(\Theta + \frac{4\pi}{3}) & M_{sr}cos(\Theta) & M_{sr}cos(\Theta + \frac{2\pi}{3}) \\ M_{sr}cos(\Theta + \frac{2\pi}{3}) & M_{sr}cos(\Theta + \frac{4\pi}{3}) & M_{sr}cos(\Theta) \end{pmatrix}. \tag{4.10}$$

Since the parameters are determined assuming equal numbers of turns in the stator and rotor,

$$M_s = M_r = M_{sr} = M_{rs}. \tag{4.11}$$

Continuing with the rotor equations, using the similar reasoning as for the stator, the inductance matrixes can be expressed as

$$\mathbf{L}_{rs} = \begin{pmatrix} M_{rs}cos(\Theta) & M_{rs}cos(\Theta + \frac{4\pi}{3}) & M_{rs}cos(\Theta + \frac{2\pi}{3}) \\ M_{rs}cos(\Theta + \frac{2\pi}{3}) & M_{rs}cos(\Theta) & M_{rs}cos(\Theta + \frac{4\pi}{3}) \\ M_{rs}cos(\Theta + \frac{4\pi}{3}) & M_{rs}cos(\Theta + \frac{2\pi}{3}) & M_{rs}cos(\Theta) \end{pmatrix} \tag{4.12}$$

$$\mathbf{L}_{rr} = \begin{pmatrix} M_r + L_{r\sigma} & -0.5M_r & -0.5M_r \\ -0.5M_r & M + L_{r\sigma} & -0.5M_r \\ -0.5M_r & -0.5M_r & M_r + L_{r\sigma} \end{pmatrix}. \tag{4.13}$$

The inductance matrix is now completely determined for the physical stator and rotor voltages and currents. However, it is possible to transform it to an arbitrary reference frame, refer to [33].

The next step is to define the $\mathbf{R}'$ matrix which can be expressed as,

$$\mathbf{R}' = \mathbf{R} + \frac{d\mathbf{L}}{dt}. \tag{4.14}$$

The expression for the R matrix can be expressed as

$$\mathbf{R} = \begin{pmatrix} R_s & 0 & 0 & 0 & 0 & 0 \\ 0 & R_s & 0 & 0 & 0 & 0 \\ 0 & 0 & R_s & 0 & 0 & 0 \\ 0 & 0 & 0 & R_r & 0 & 0 \\ 0 & 0 & 0 & 0 & R_r & 0 \\ 0 & 0 & 0 & 0 & 0 & R_r \end{pmatrix}. \tag{4.15}$$

The model of the IM is now described using the phase voltages as input. However, the phase voltage is not well defined when the IM is fed with a PWM voltage since the sum

of the phase voltages do not equal zero (as for a balances sinusoidal voltage). Hence, it is more convenient to use the line to line voltages as inputs. It is further assumed that

$$i_a + i_b + i_c = 0. \tag{4.16}$$

The system equations can easily be modified, and by using (4.16) the system can be expressed using two line to line voltages as inputs.

In order to simplify the expression the following variables are defined,

$$A_1 = cos(\Theta) \tag{4.17}$$

$$A_2 = cos(\Theta + \frac{2\pi}{3}) \tag{4.18}$$

$$A_3 = cos(\Theta + \frac{4\pi}{3}) \tag{4.19}$$

$$B_1 = sin(\Theta) \tag{4.20}$$

$$B_2 = sin(\Theta + \frac{2\pi}{3}) \tag{4.21}$$

$$B_3 = sin(\Theta + \frac{4\pi}{3}). \tag{4.22}$$

By rearing the $\mathbf{L}$ and $\mathbf{R}$ matrix in order to suit the line to line voltages u_{a-bs}, u_{b-cs},u_{b-cr} and u_{b-cr} and furthermore eliminating i_{cs} and i_{cr},$\mathbf{L}$ and $\mathbf{R}$ can be expressed as

$$\mathbf{L} = \begin{pmatrix} 1.5M + L_{s\sigma} & -1.5M - L_{s\sigma} & M(A_1 + A_2 - 2A_3) & M(-A_1 + 2A_2 - A_3) \\ 1.5M - L_{s\sigma}) & 3M + 2L_{s\sigma} & M(A_1 - 2A_2 + A_1 + A_3) & M(2A_1 - A_2 - A_3) \\ M(A_1 - 2A_2 + A_3) & M(-A_1 - A_2 + 2B_3) & 1.5M + L_{r\sigma} & -1.5M - L_{r\sigma} \\ M(A_1 + A_2 - 2A_3) & M(2A_1 - A_2 - 3B_3) & 1.5M - L_{r\sigma}) & 3M + 2L_{r\sigma} \end{pmatrix} \tag{4.23}$$

$$\mathbf{R} = \begin{pmatrix} R_s & -R_s & 0 & 0 \\ R_s & 2R_s & 0 & 0 \\ 0 & 0 & R_r & -R_r \\ 0 & 0 & R_r & 2R_r \end{pmatrix}. \tag{4.24}$$

The $\mathbf{U}$ matrix can now be defined as

$$\mathbf{U} = \begin{pmatrix} u_{a-bs} \\ u_{b-cs} \\ u_{a-br} \\ u_{b-cr} \end{pmatrix}. \tag{4.25}$$

The electrical state derivatives can be expressed in the $\mathbf{x}$ matrix as

$$\mathbf{x} = \begin{pmatrix} i_{as} \\ i_{bs} \\ i_{ar} \\ i_{br} \end{pmatrix}. \tag{4.26}$$

Finally, the U matrix can be expressed as,

$$\mathbf{U} = \mathbf{L} \cdot \dot{\mathbf{x}} + (\mathbf{R} + \frac{\mathbf{d}}{\mathbf{dt}}\mathbf{L}) \cdot \mathbf{x}. \tag{4.27}$$

The electrodynamic torque, T_{el}, can be expressed as

$$T_{el} = \frac{p\sqrt{3}M}{2}[(B_1 i_{ra}+B_2 i_{rb}+B_3 i_{rc})i_{sa}+(B_1 i_{rb}+B_2 i_{rc}+B_3 i_{ra})i_{sb}+(B_1 i_{rc}+B_2 i_{ra}+B_3 i_{rb})i_{sc}]. \tag{4.28}$$

Finally the rotor speed derivative can be expressed as

$$\frac{d}{dt}\omega = \frac{p}{J}(T_{el} - T_L) \tag{4.29}$$

where p and J is the number of pole pairs and the moment of inertia respectively and T_L is the load applied to the motor.

4.1.2 Steady state modeling

A steady-state model of the IM including the core losses and stay losses has been proposed in [10] and the Y-equivalent circuit representation from this article is presented in figure 4.1. The difference compared to the more common representation of the equivalent circuit is the the resistance in parallel with the rotor leakage inductance. This resistance, R_{stray}, represents the stray losses in the rotor circuit. This results from studies made on the stray losses[11], showing that the stray losses are proportional to the square of the shaft torque. In addition, [11] has further shown that the stray losses are proportional to the operating frequency. Hence, R_{stray} can be expressed as

$$R_{stray}(f) = R_{stray50Hz}\frac{f}{50} \tag{4.30}$$

The iron losses are represented by R_c and are also dependent on the frequency. The value of R_c as a function of the frequency are calculated from measurement, refer to Section 4.1.3.

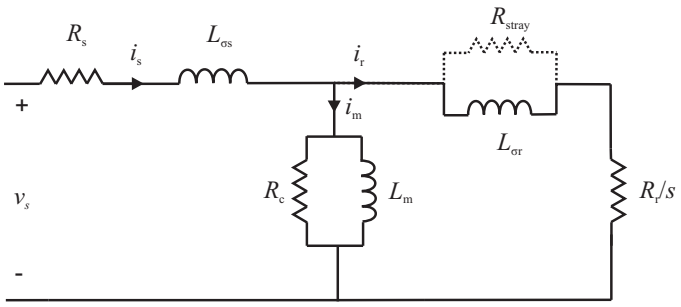

Figure 4.1 Y-ekvivalent circuit of an IM including iron and stray losses.

4.1.3 Parameter identification

The IM parameters can be identified using different series of tests. The stator resistance can be obtained by by measuring the line to line DC resistance R_{DC}. The per phase stator resistance is then half R_{DC}.

When the IM is running at no load, the sum of the core losses and the mechanical losses, P_{cm}, can be established. At no load, the rotor part of the circuit is open and s approximately equals zero,

$$\frac{R_r}{s} = \infty, \tag{4.31}$$

and the resistance and the inductance on the rotor side can be ignored. To separate the mechanical and the core losses a test named *the no load test* has to be performed. The measured quantities required for *the no load test* are

- The no load input power P_0 (P_0 includes the stator loss (P_{stator} = $3I^2R_s$), the core loss, P_{core}, and the mechanical loss, P_{mec})
- The no load line current, I_0
- The phase voltage U_{ph}
- The stator resistance R_s

The mechanical losses and the core losses can be obtained by subtracting the stator losses from the total losses. To separate the core losses from the mechanical losses, the sum of the two losses, can be plotted against the square of the phase voltage, U_{ph}, since the core loss is proportional to U_{ph}^2, where U_{ph} is ranging from 125% of its rated value down to the value where the current is increased, according to [38]. Linear regression is performed on the measured values, which results in the best linear approximation. The mechanical loss P_{mecl} can now be obtained from the plot where the voltage U_{ph}^2=0 (since P_{mec} is independent of U_{ph}).

Finally, R_c can be calculated as

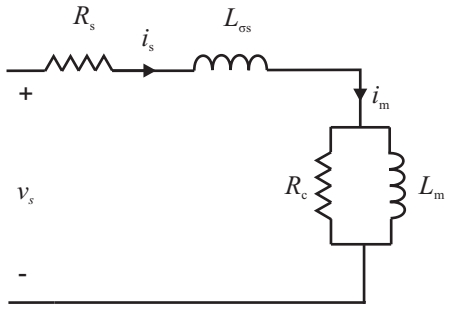

Figure 4.2 Y-ekvivalent circuit of an IM at no load, s = ∞.

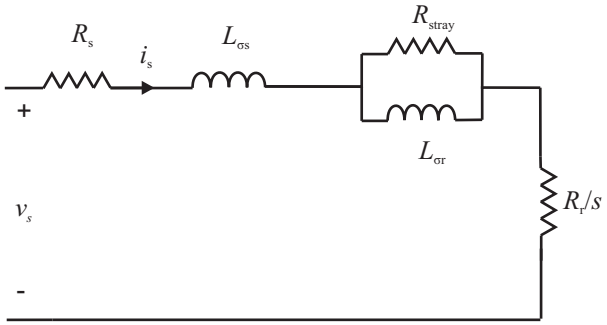

Figure 4.3 Y-ekvivalent circuit of an IM with locked rotor, s=1, neglecting L_m and R_c

$$R_c = \frac{3(\mathbf{U}_{ph} - \mathbf{I}_0 R_s^2 - \mathbf{I}_0 j\omega L_{\sigma s})}{P_c}. \tag{4.32}$$

In order to avoid losses caused by switching harmonics the motor will be fed by a pure sinusoidal at the no load test. As a result, only the fundamental iron loss component will be obtained.

The remaining components can now be estimated by measuring the phase voltages and current at no load and at locked rotor, refer to figure 4.2 and 4.3.

The stator and rotor leakage inductances can be calculated from the locked rotor test

$$X_{r\sigma} + X_{s\sigma} = \Im[\frac{\mathbf{U}_{ph}}{\mathbf{I}_{lock}}] \tag{4.33}$$

it is further assumed that,

$$X_{r\sigma} = X_{s\sigma}. \tag{4.34}$$

R_r is calculated as

$$R_r = \Re[\frac{\mathbf{U}_{ph}}{\mathbf{I}_{lock}}] - R_s \tag{4.35}$$

Finally, the magnetizing inductance are estimated from the no load voltage and current,

$$X_m = \Im[\frac{\mathbf{U}_{ph} - \mathbf{I}_0\mathbf{U}_{ph}}{\mathbf{I}_0}] - X_{s\sigma}. \tag{4.36}$$

The resistance representing the stray losses in equation 4.30, $R_{stray50Hz}$ can be estimated by approximating the stray losses at rated output power presented in different standards (IEC, IEEE). However, the standards are not in agreement [10]. Stray losses of 0.5-2.5% of the rated output power are proposed, depending on motor the rating, (the relative stray loss component increases with decreasing motor rating). By assuming that the stray losses are x% of the rated output power, the real part of $R_{stray50Hz}$ in parallel with $X_{\sigma r}$ can be calculated as,

$$\Re[R_{stray50Hz}||jX_{\sigma r}] = \frac{x}{100}\frac{P_{mecN}}{3I_{rN}^2} \tag{4.37}$$

It is now straight forward to calculate $R_{stray50Hz}$.

All parameters in the equivalent circuit can now be determined. However, the parameters are not constant in the operating region of the IM. Following list describes how the motor parameters are affected during the operation.

- R_s: The stator resistance is temperature dependent. When the temperature increases the resistivity increases, increasing the stator resistance and hence the stator losses. The temperature coefficient for copper is approximately 39(10^{-3}/°C) meaning that a 50°C increase in temperature results in approximately 20% increase of the stator resistance.

- R_r: The same reasoning as for the rotor resistance. However, the rotor often consists of aluminium instead of copper, having a temperature coefficient of 43(10^{-3}/°C)

- $L_{\sigma x}$: The leakage inductance in the motor are dependent on the magnitude of the current. A reasonable parameter value changes is 2% [39].

- L_m: The magnetizing inductances in the motor is mainely dependent on the magnetizing current and decreases with increasing current. An example of parameter changes are 10% increase in L_m when the magnetizing current decreases with 20% [39].

- R_c: R_c is only a function of the frequency given that the flux level are below the nominal value.

- R_{stray}: The uncertainties are already discussed above.

4.2 Brushless DC motor

The topic of BLDC modeling has been well documented in the literature [31, 32]. However, usually only general models, which are not straightforward to implement are presented, therefore, a more detailed Matlab Simulink ® model will be explained in this section.

4.2.1 Dynamic modeling

The general state space model is expressed in (4.38), where L_s and R_s represents the per phase self inductance and resistance respectively, M the mutual inductance and e_x the back emf of phase x.

$$\begin{pmatrix} v_a \\ v_b \\ v_c \end{pmatrix} = \begin{pmatrix} R_s & 0 & 0 \\ 0 & R_s & 0 \\ 0 & 0 & R_s \end{pmatrix} \begin{pmatrix} i_a \\ i_b \\ i_c \end{pmatrix} + \begin{pmatrix} L_s - M & 0 & 0 \\ 0 & L_s - M & 0 \\ 0 & 0 & L_s - M \end{pmatrix} \begin{pmatrix} \frac{di_a}{dt} \\ \frac{di_b}{dt} \\ \frac{di_c}{dt} \end{pmatrix} + \begin{pmatrix} e_a \\ e_b \\ e_c \end{pmatrix}. \tag{4.38}$$

However, the phase voltages v_a, v_b and v_c are not well defined for the same reason as for the induction motor model presented in Section 4.1.1. Hence, the model is modified in order to satisfy the line to line voltages as inputs. It is also assumed that the sum of the phase currents equals zero. The model can now be written according to (4.39) and (4.40)

$$\begin{pmatrix} v_{ab} \\ v_{bc} \end{pmatrix} = \begin{pmatrix} R_s & -R_s \\ R_s & 2R_s \end{pmatrix} \begin{pmatrix} i_a \\ i_b \end{pmatrix} + \begin{pmatrix} L_s - M & -L_s + M \\ L_s - M & 2(L_s - M) \end{pmatrix} \begin{pmatrix} \frac{di_a}{dt} \\ \frac{di_b}{dt} \end{pmatrix} + \begin{pmatrix} e_{ab} \\ e_{bc} \end{pmatrix}, \tag{4.39}$$

where

$$i_c = -i_b - i_a. \tag{4.40}$$

The next step is to determine the line to line voltages which are determined from the excitation of the converter, (the operation of the BLDC motor was described in 3.2). Hence the on and off state of the transistors are known and depends on the rotor position. However, when a phase voltage is turned off, the current will not go to zero at the same instant due to the inductance in the circuit. Instead, the current will continue to flow in the opposite freewheeling diode changing the polarity of the phase voltage. The phase voltage will remain in opposite polarity until the current reaches zero. The phase current will then remain at zero until the phase voltage is turned back on. It should also be noted that the transistors and freewheeling diodes are regarded as ideal components, and hence, turn on and off instantaneously.

In order to satisfy this criterion, the model will be divided into 6 parts in the range between 0-360° (electrical degrees) each consisting of two states, refer to figure 4.2.1.

1. 0-60°

At 0°, transistor T5 is turned off and T1 is turned on. The current in phase c, i_c decreases to zero (i_a increases from zero). At the time interval when $i_c \neq 0$, the current is freewheeling through D6, and the voltages can be expressed as,

$$v_{ab} - e_{ab} = \frac{V_s}{2} - (-)\frac{V_s}{2} - e_{ab} = V_s - e_{ab} \tag{4.41}$$

$$v_{bc} - e_{bc} = -\frac{V_s}{2} - (-)\frac{V_s}{2} - e_{bc} = -e_{bc} \tag{4.42}$$

When i_c reaches zero no current is flowing in phase c and the model can be expressed as:

$$v_{ab} - e_{ab} = V_s - e_{ab} \tag{4.43}$$

$$\frac{di_a}{dt} = \frac{V_s - e_{ab} - 2R_s}{2L_s - M} \tag{4.44}$$

$$\frac{di_b}{dt} = -\frac{di_a}{dt} \tag{4.45}$$

$$\frac{di_c}{dt} = 0 \tag{4.46}$$

2. 60-120°

T4 are turned off and T6 turned on, the reasoning is similar to the previous interval.

$i_b \neq 0$

$$v_{ab} - e_{ab} = \frac{V_s}{2} - \frac{V_s}{2} - e_{ab} = -e_{ab} \tag{4.47}$$

$$v_{bc} - e_{bc} = \frac{V_s}{2} - (-)\frac{V_s}{2} - e_{bc} = V_s - e_{bc} \tag{4.48}$$

$i_b = 0$

$$v_{ac} - e_{ac} = V_s - e_{ac} \tag{4.49}$$

$$\frac{di_a}{dt} = \frac{V_s - e_{ac} - 2R_s}{2L_s - M} \tag{4.50}$$

$$\frac{di_c}{dt} = -\frac{di_a}{dt} \tag{4.51}$$

$$\frac{di_b}{dt} = 0 \tag{4.52}$$

3. 120-180°

T1 is now turned off and T3 turned on the details are from now on left out since it is similar to the above two cases.

4. 180-240°

T6 off T2 on.

5. 240-300°

T3 off T5 on

6. 300-360°

T2 off T4 on

Additional power electronics is needed in order to control the magnitude of V_s. This can be achieved with a DC/DC converter, placed after the diode rectifier.

Simulation results

A 0.372kW 6-pole BLDC motor has been simulated in order to illustrate different control strategies of the converter. Figure 4.4a shows the phase voltage, the back-emf and the phase current for one period. V_s is assumed to be constant at a level of 100V and the windings are excited according to the previous explanation.

It can be noted the the current waveform deviates from the ideal current wave shape presented in Section 3.2. The reason is the inductance in the circuit, as well as the phase shifts each 60°. The dip in the current at 60° results from the phase shift between the b and c pahse. Prior to the shift, the common Y connection of the motor has a potential of 0V. However, when T4 are turned off and T6 turned on at 60°, the common Y connection will increase by V_s/6. As a result, i_a starts to decrease until i_c reaches zero and the potential in the common Y connection changes back to its original value.

It is evident, refer to Section 3.2, that this will cause a torque ripple. This can be reduced by control of the DC/DC converter. The DC voltage after the rectifier stage is the maximum output voltage to the motor. The 100V output is controlled by the DC/DC converter. However, at the phase transition, instead of applying 100V to the motor, the DC/DC converter puts out its maximum voltage, namely the voltage after the diode rectifier. When the current, in this case i_c, reaches zero the DC/DC converter return to its 100V output. This control technique will make the transitions much faster for apparent reasons.

A simulation result of this technique can be seen in figure 4.4b. It can be noted that the current is much closer to the ideal case compared to 4.4a. However, when the output voltage comes closer to the DC-link voltage, the ripple becomes larger. similar problems occurs at low speed, where the change in DC-voltage can be more precisely controlled. [34] suggests an adaptive control algorithm for this purpose.

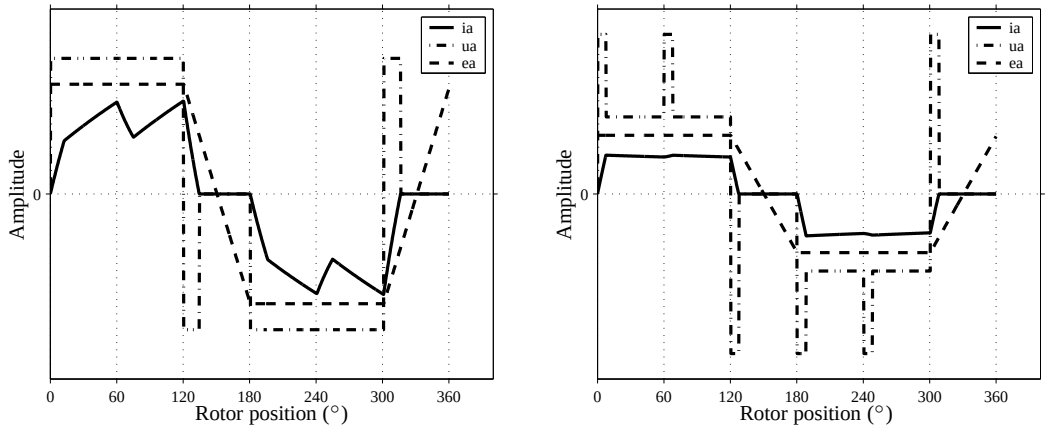

(a) Phase voltage, current and back emf for constant DC-voltage

(b) Phase voltage, current and back emf where the DC-voltage is increased during the phase transitions

Fig. 4.4 Simulation result of a BLDC motor for two types of DC voltage controls

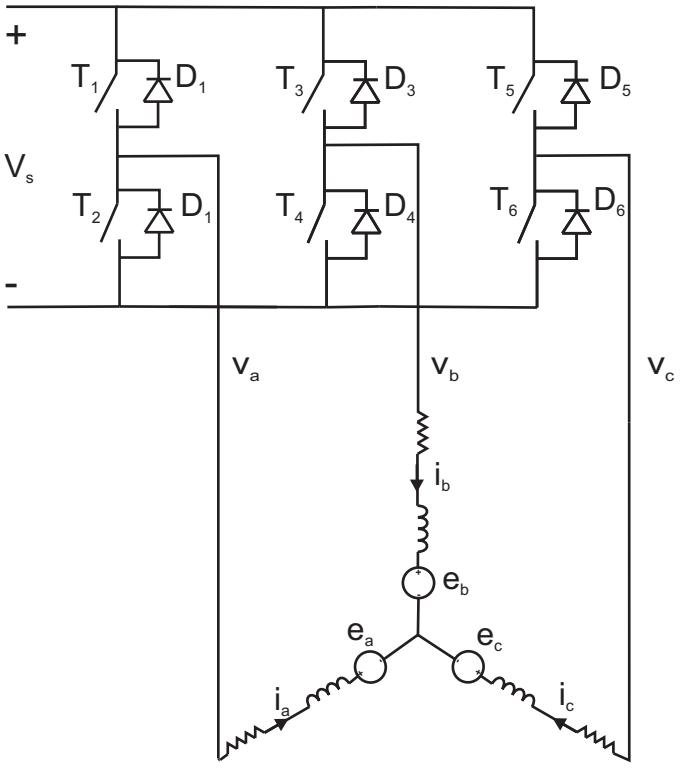

Fig. 4.5 Ekvivalent circuit of a BLDC drive

4.2.2 Parameter identification

In order to obtain the different parameters needed for the model, a series of test can be performed. The stator resistance can be obtained by measuring the stator winding resistance in the same manner as for the IM. The back emf can be obtained by rotating the motor and measure the induced voltage in the stator windings. Since no current is flowing in the windings, the measured voltage will be the back emf. Finally, the stator inductance can be estimated by studying the current derivatives.

4.3 Frequency converter

This section will present the assumptions made for estimating the losses in the frequency converter. The losses consists of switching losses and conductive losses. Typical switching characteristics was presented in Section 3.3. As a result, the switching loss for a component during a switching transition can be calculated as

$$W_{sw} = \int_{t_1}^{t_2} u(t)i(t)dt \tag{4.53}$$

where $u(t)$ and $i(t)$ are the voltage over the component and the current through the component during the switching interval and t_1 to t_2 is the time duration of the switching transition. The shape of $i(t)$ and $u(t)$, level and time duration, can be measured or in some extent be obtained from data sheets. In order to simplify the calculations, it is further assumed that the losses at each switching instant are proportional to the current at the switching instant. Hence, the power dissipation in a component x can be expressed as

$$P_{swx} = \frac{k_x}{f} \sum_{i=1}^{n} I_i \tag{4.54}$$

where k_x is a constant for component x, f is the fundamental frequency I_i is the current magnitude at a switching instant i and n is the number of switching instants during one period of the fundamental.

The conductive losses in a component depends on the voltage drop across the component U_{on} and the on-state current, I_{on}. The voltage drop is often dependent on both the current magnitude and the temperature of the component. The characteristics can be obtained from data sheets to some extent. However, it is fairly simple to obtain U_{on} as a function of the temperature and current from measurements. Given $U_{on}(I_{on})$ and I_{on}, the power dissipation can be calculated as

$$P_{cx} = \frac{1}{f} \sum_{i=1}^{n} U_{on}(I_i) I_i t_i \tag{4.55}$$

where t_i is the time duration of the conduction i and the sum includes one period of the fundamental.

The losses in the converter are now modeled and can be estimated for a given current and switching pattern.

Chapter 5

Field measurements on HVAC applications

This chapter will present the results obtained from the field measurements that have been performed. One commercial building has been the target of a long period of measurement in in order to establish the power demand of different applications but also to investigate the dimensioning of the drive systems.

5.1 Field measurements

Field measurements have been performed on five different pump applications in an office building. The electrical power has been measured with CEWE DQ 235 power meters and logged each minute. This section will present the most interesting result from this study.

Figure 5.1 shows a schematic over a part of the pump system. Pump p_1 is the main pump on the heating side, serving a number of branches including a radiator circulator and a floor hating circulator, referred to as p_2 and p_2 respectively. Pump p_1 is a PMSM type with a rating of 450W, operating at a constant pressure of 4.5m. Note that the rated power is given for the electrical input power. Figure 5.2 shows the distribution of the electrical power to the pump from June 2006 to April 2008. It can be noted that the operating power is at maximum 50% of the rated power.

Pump p_2 is a variable speed pump using an IM rated at 250W. It serves 70 radiators and is operated at a constant pressure of 1.1m. The pump is turned off when the outdoor temperature is above 20°. The temperature of the circulating water is controlled by a valve mixing the return water from the radiators with the water delivered from the main pump. Figure 5.3 shows the distribution of power demand of the pump for the period June 2006 to April 2007. It can be noted that also in this case the maximum electrical power input is approximately 50% of the rated power.

Pump p_3 is of a constant speed type and is turned off when the outdoor temperature is above 18° otherwise its turned on. The power demand of the pump can be seen in figure

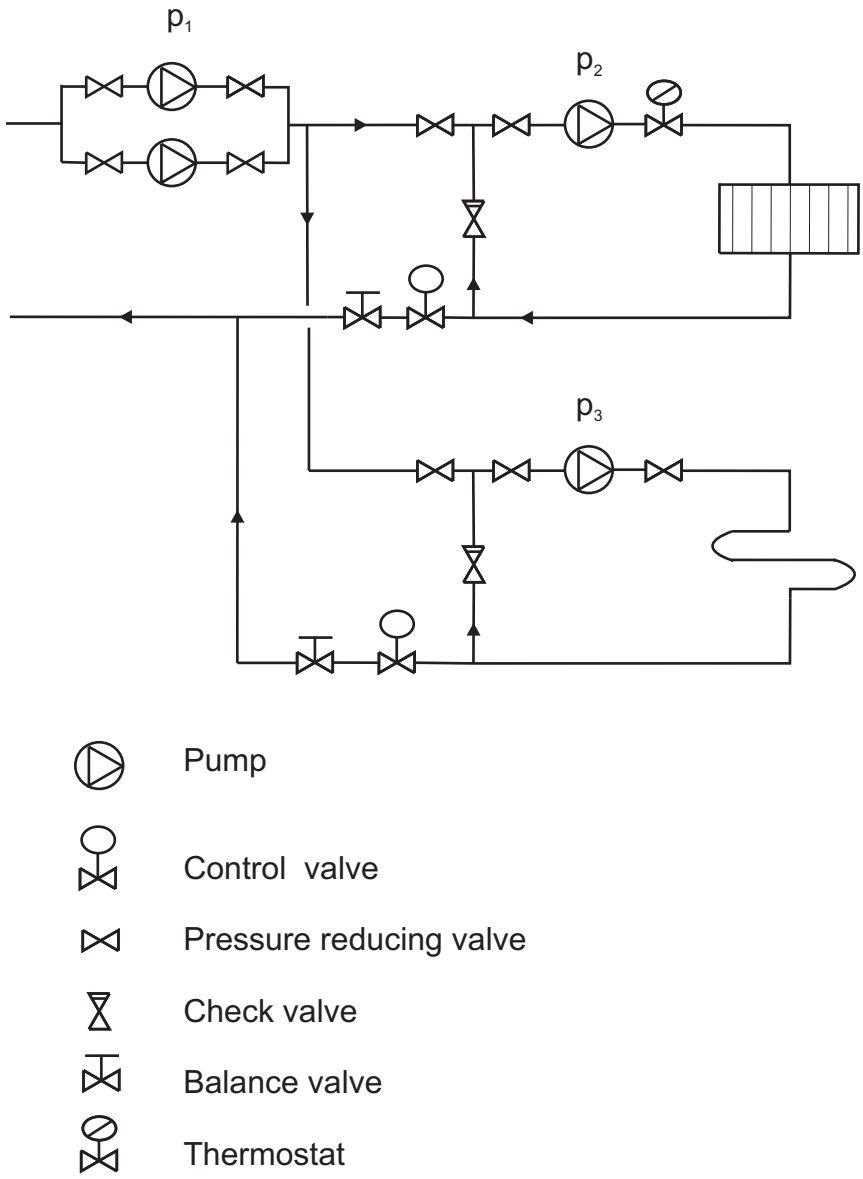

Fig. 5.1 Overview of one part of the pumping system including the main pump (p_1), radiator pump (p_2) and the floor heating pump (p_3)

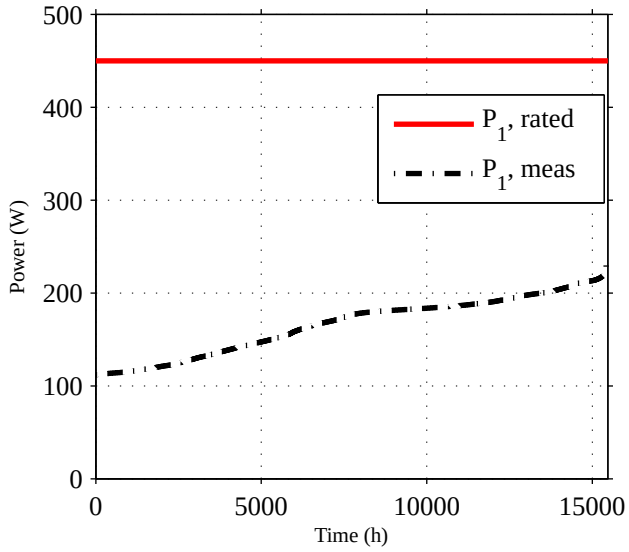

Fig. 5.2 Electrical input power the main pump during June 2006 to April 2008

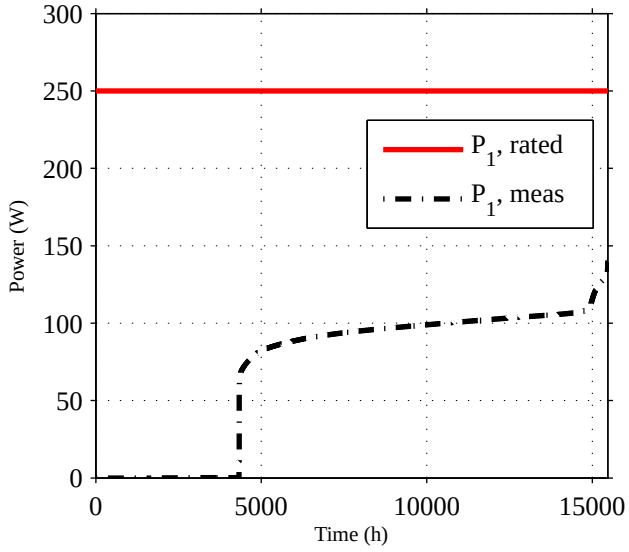

Fig. 5.3 Electrical power demand of the radiator circulator during June 2006 to April 2008

5.4 for the same time distribution as above.

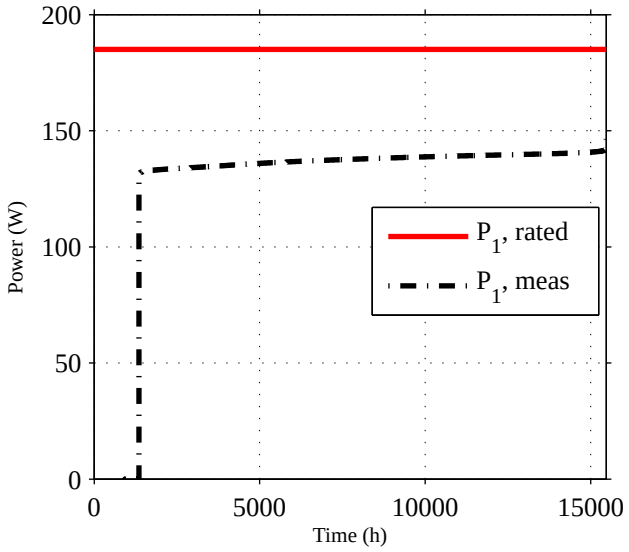

Fig. 5.4 Electrical power demand for the floor heating circulator during June 2006 to April 2007

Measurement has been also been carried out on a pump serving a cooling coil. The pump is a dry rotor pump of variable speed type with an IM, rated at 1.5kW. Figure 5.5 shows the input power distribution for the same period as above. It should be noted that the rated value for dry pumps are given for the mechanical output power of the motor. Hence, it can be noted that the motor is over dimensioned by far more then 100% referred to the electrical input power need.

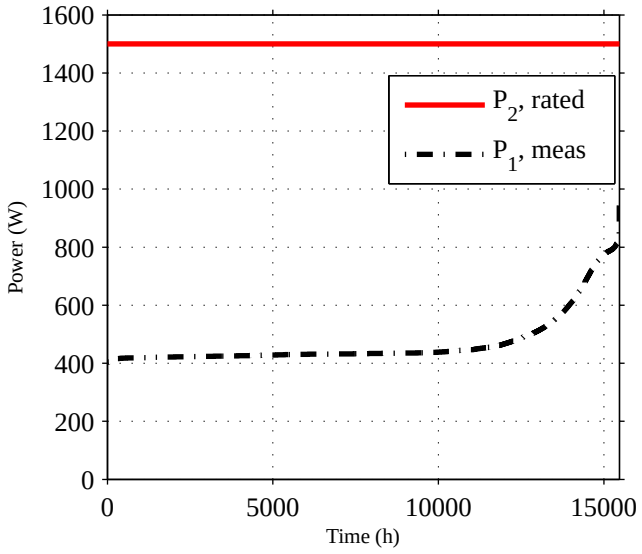

Fig. 5.5 Electrical input power to pump 4 during June 2006 to April 2008

Chapter 6

Efficiency determination of different Induction motor drive systems

Improvements of energy efficiency in a frequency converter and IM can be achieved either by changing the design or using different control schemes. This chapter will investigate the impact on efficiency in the IM using different design and control techniques, using simulations. Furthermore, different switching techniques will be investigated.

6.1 Induction motor setup

This section will present the energy efficiency of an IM and its dependence on motor design and control. Simulations have been carried out which are further used in Chapter 8 for determination of potential HVAC savings.

6.1.1 Comparison between different motor designs

This section will focus on the difference between the efficiency using eff1-eff3 motors described in Section 3.1. The stationary model of the IM will be used together with the method presented in Section 4.1.3 for parameter identification.

Parameter identification according to Section 4.1.3 has been performed on a 4-pole 4kW standard induction motor (eff3). The parameters are presented in Table 6.1.

The parameters are now modified in order to suit an eff1 and eff2 IM. The efficiency at 75% rated output power operating at rated voltage/frequency is assumed to increase 2% for an eff2 and 4.1% for an eff1 motor respectively, compared to the eff3 IM. The following assumptions have been made:

- R_r: For an eff1 IM, the aluminium in the rotor is replaced by copper which has approximately 37% lower resistivity. Hence, the value of R_r is reduced with 37%. The value for an eff2 IM is unchanged

Table 6.1 Motor data

Parameter	Eff3	Eff2	Eff1
R_s	1.5 Ω	1.28 Ω	1.2 Ω
R_r	1.3 Ω	1.3 Ω	0.82 Ω
$R_{c,50Hz}$	606 Ω	760 Ω	900 Ω
$R_{stray50Hz}$	9.89 Ω	8.13 Ω	9.5 Ω
$L_{\sigma s}$	8 mH	8 mH	8 mH
$L_{\sigma r}$	8 mH	8 mH	8 mH
L_m	0.14 H	0.14 H	0.14 H
P_{mecN}	4 kW	4 kW	4 kW
n_N	1435 rpm	1445 rpm	1455 rpm
U	3x400 V	3x400 V	3x400 V
I_{sN}	9.1 A	9.0 A	8.9 A

- R_s: For an eff1 and eff2 IM, more copper is used in the stator winding, resulting in a reduced stator resistance. It is assumed to be 20% and 15% lower for an eff1 and eff2 IM respectively.
- R_c: The rest of the increased efficiency is tuned in by increasing R_c. This can be motivated the assumption of thinner laminations.
- $R_{stray50Hz}$: The stray losses are still assumed to be 2% of the rated output power. However, the value needs to be modified since the operating condition has changed due to the modified motor parameters
- The inductances are assumed to be unchanged.

Section 6.1.3 will present simulation results of the eff3 and eff1 motor.

6.1.2 Energy optimal control of the Induction motor

The torque characteristics of an IM was briefly discussed in Section 3.1. It was stated that a simple control technique of an IM is to use constant V/Hz control, meaning that the ratio of the voltage and frequency is kept constant. As a result, the magnetic flux in the motor is kept constant which makes it possible to load the IM with its rated torque even at low frequencies. However, an operating point can be achieved with different sets of V/Hz as can be seen in figure 6.1, note that the slope of the curves are exaggerated for the purpose of illustration. It can be noted that the slip is increasing when the slope of the T-n is decreased, resulting in an increased current and thereby higher resistive losses. On the other hand, since the voltage is decreased, the core losses are lowered. It can be shown that each operating point has its unique set of V/Hz in order to minimize the losses in the motor [9]. Figure 6.2 shows an example of the core losses together with the resistive losses

for a constant operating point, (T,n)=(3.7Nm,800rpm), as a function of frequency. The efficiency of the IM is also presented and it can be seen in the figure that the maximum efficiency occurs, approximately, when the core and resistive losses intersects. The phase voltage at this operating point has been reduced from 126.5V, operating at constant V/Hz, to 76.4V.

Many loads have a lower torque demand at lower speeds, especially pumps and fans. Hence, it is possible to make substantial energy savings by controlling the motor to its optimal V/Hz.

The oncoming sections will present simulation results of the losses in an IM.

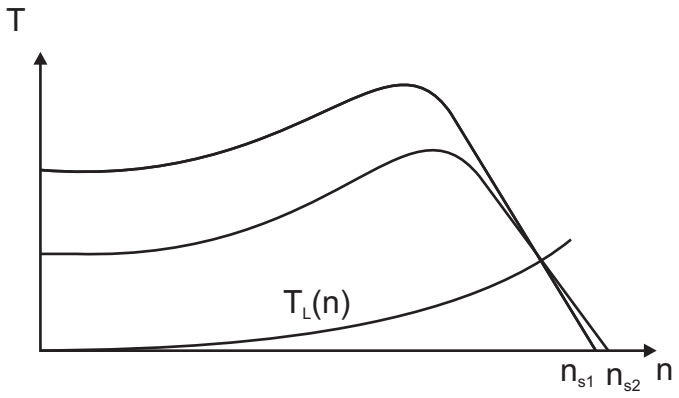

Fig. 6.1 Torque speed characteristics for two different setups of voltage/frequency resulting in identical operating point for the given load

6.1.3 Calculation result of different design and control techniques

Calculations have been performed using the steady-state model presented in Section 4.1.2. Different types of motor designs, according to Section 6.1.1, and different V/Hz control, according to Section 6.1.2, have been investigated. The result in this section will be further used in order to investigate the potential savings in HVAC applications, refer to Chapter 8.

4kW 4-pole IM

The efficiency has been calculated for an eff3 and eff1 IM, controlled with constant V/Hz and the eff1 IM with optimal V/Hz. Two different loads was used in the calculations, T=$b_1\omega^2$ and T=$b_2\omega$, where b_1 and b_2 are constants resulting in rated torque at rated speed. Figure 6.3 shows the efficiency of the IM with the quadratic load demand and figure 6.4 shows the efficiency using the linear load demand. It should be noted that the voltage is limited to is rated value. As a result, the optimal control of V/Hz will be limited at higher load. For example, the calculated optimal voltage becomes 15% above the rated value at at 100% load demand.

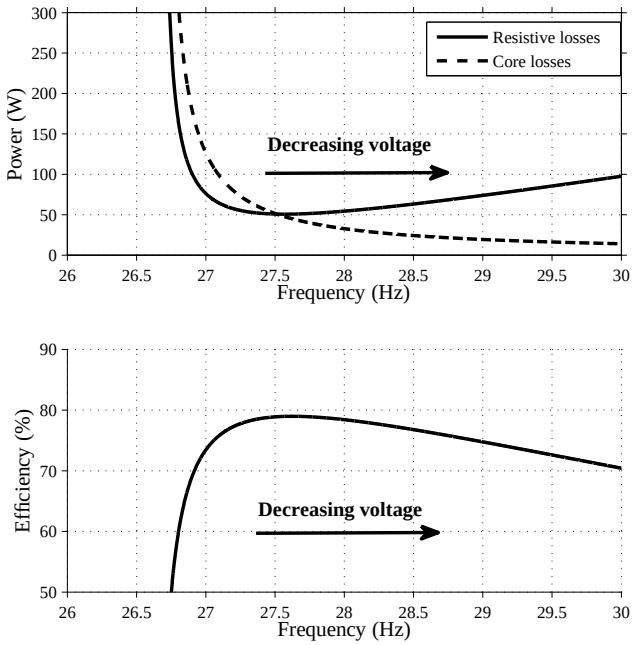

Fig. 6.2 Resistive losses in the stator and rotor for a given operating point,(T, n)=(3.7Nm, 800rpm), and the resulting efficiency of the IM

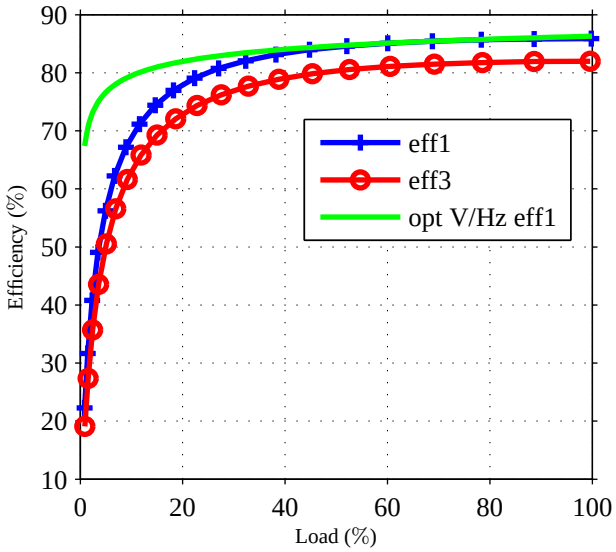

Fig. 6.3 Efficiency of the different IM setups applied to a quadratic load

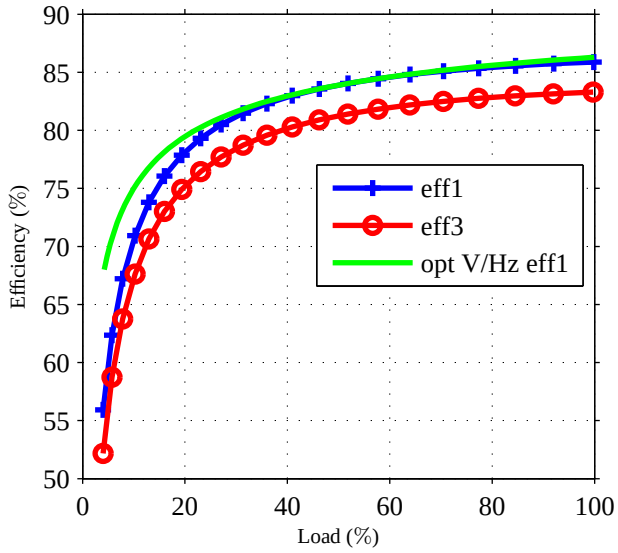

Fig. 6.4 Efficiency of the different IM setups applied to a linear load

The calculations assumed a load that was perfect dimensioned to the motor, 100% load demand gave the rated power of the motor.

6.2 Frequency converter setup

The basic operation of a frequency converter was described in Section 3.3. The production of a variable voltage and frequency using pulse with modulation (PWM) was described briefly.

This section will focus on how different PWM schemes affects the efficiency of the converter and motor.

6.2.1 Sinousodial PWM

Sinusoidal PWM was briefly introduced in the introduction to frequency converter since it gives a simple illustration of the PWM technique. However, this method has several drawbacks compared to more advanced techniques. For a modulation index, M, defined as,

$$M = \frac{V^*}{V_s/2} \tag{6.1}$$

where V^* is the amplitude of the reference voltage and V_s is the DC bus voltage, M=1 is the maximum value for linear control, . With M=1 the line to line voltage, V_{l-l} becomes

$$V_{l-l} = \sqrt{3}\frac{V_s}{2}. \tag{6.2}$$

For an ideal three phase inverter connected to a 400V grid V_s equals the peak value of the $l-l$ voltage, 565V, resulting in a maximum output peak line to line voltage of 490V (approx 87% of the rated value). Hence, it will not be possible to operate an IM at its 50Hz 400V rating which is one of the major drawbacks using this technique.

It is possible to increase the amplitude above $M = 1$ by using so called over modulation. However, the nonlinear relationship between M and the voltage magnitude is not desirable from a control point of view. Furthermore, over modulation results in low frequency harmonics. Instead a method to increase the linear control range will be discussed in the next section.

The current ripple will be used as an indicator of the harmonic losses. Assuming a delta connected load and a constant internal emf voltage during a switching transition, the current ripple through a delta load element can be expressed as,

$$I_{ab} = \frac{V_s^2}{4L_\sigma^2}\frac{\Delta T^2}{48}[\frac{3}{2}M^2 - \frac{4\sqrt{3}}{\pi}M^3 + \frac{9}{8}M^4] \tag{6.3}$$

where Δ T is half of the switching period. The term L_σ is defined as,

$$L_\sigma = L_s + \frac{L_r L_m}{L_r + L_m} \tag{6.4}$$

where L_s and L_r are the leakage inductances of the stator and rotor respectively and L_m is the magnetizing inductance.

The interested reader can find the derivation in [12].

6.2.2 Sinousodial PWM using third harmonic injection

It is possible to increase the modulation index above one and still have the linear relationship between M and the voltage reference. This is done by changing the common mode reference voltage. By adding a third harmonic component to phase voltage references it is possible to increase the modulation index. It can be shown [12] that a 15% increase is possible if the magnitude of the third component is 1/6 of the fundamental. However, this technique introduces low order harmonics. [12] also suggests a 1/4 third harmonic injection in order to improve the harmonic content on the cost of reduced output voltage.

The current ripple when injecting the third component with a magnitude of 1/6 gives a fundamental that is slightly larger then for a 1/4 injection at a modulation index close to 1.

The current ripple, using the same assumption as in (6.3), for the techniques can be expressed as

$$I_{ab1/6} = \frac{V_s^2}{4L_\sigma^2}\frac{\Delta T^2}{48}[\frac{3}{2}M^2 - \frac{4\sqrt{3}}{\pi}M^3 + M^4] \tag{6.5}$$

$$I_{ab1/4} = \frac{V_s^2}{4L_\sigma^2}\frac{\Delta T^2}{48}[\frac{3}{2}M^2 - \frac{4\sqrt{3}}{\pi}M^3 + \frac{63}{64}M^4]. \tag{6.6}$$

6.2.3 Space Vector Modulation

This section will describe the basics of space vector modulation (SVM) and different SVM schemes purposed in the literature.

A balanced three phase voltages, v_a, v_b and v_c can be transformed to an equivalent voltage vector v_α+j v_β, where v_α and v_β are defined as

$$\begin{pmatrix} v_\alpha \\ v_\beta \end{pmatrix} = \begin{pmatrix} 1 & 0 & 0 \\ 0 & \frac{1}{3} & -\frac{1}{3} \end{pmatrix} \begin{pmatrix} v_a \\ v_b \\ v_c \end{pmatrix}. \tag{6.7}$$

Figure 6.2.3 shows the three phase voltage and its equivalent α β components.

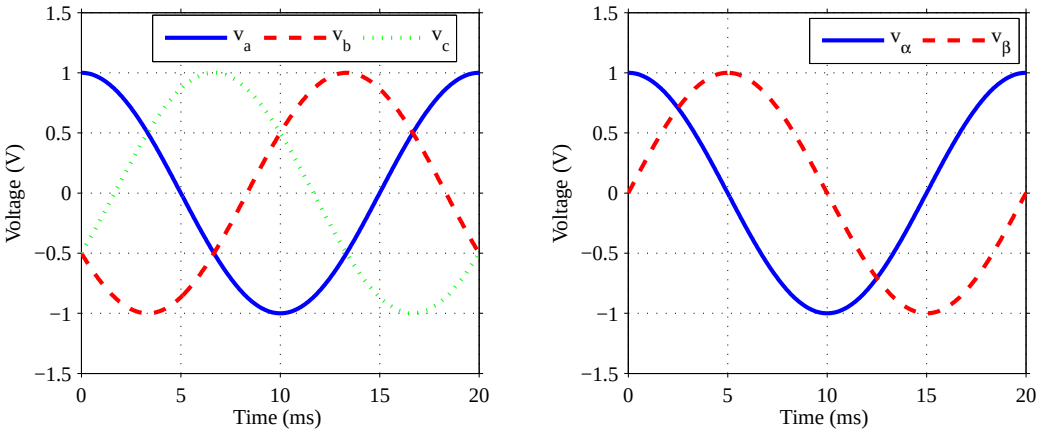

(a) Three phase voltage

(b) Transformed three phase voltage to its $\alpha\beta$ components

Fig. 6.5 Three phase voltage and its $\alpha\beta$ equivalent.

The $\alpha\beta$ components can now be mapped in the $\alpha\beta$-plane shown in figure 6.6 where V_1-V_{12} denotes examples of instantaneous voltage vectors during one period of the fundamental voltage. It is evident that the inverter generates a finite number of voltage vectors

Figure 6.7 shows the different switch combinations possible for a three phase inverter. The stationary space vector in the $\alpha\beta$ plane, created by the different switch states are shown in figure 6.8. Note that the magnitude of space vectors **SV0** and **SV7** are zero. An arbitrary space vector, $\mathbf{V}^*$, can now be created by switching between the different space vectors. If, for example, $\mathbf{V}^*$ at a time instant is located between **SV1** and **SV2** the vector is created by switching between **SV1**, **SV2** and the zero space vectors **SV0** and **SV7**. During half the switching period, T_{sw}/2, $\mathbf{V}^*$ can be expressed as,

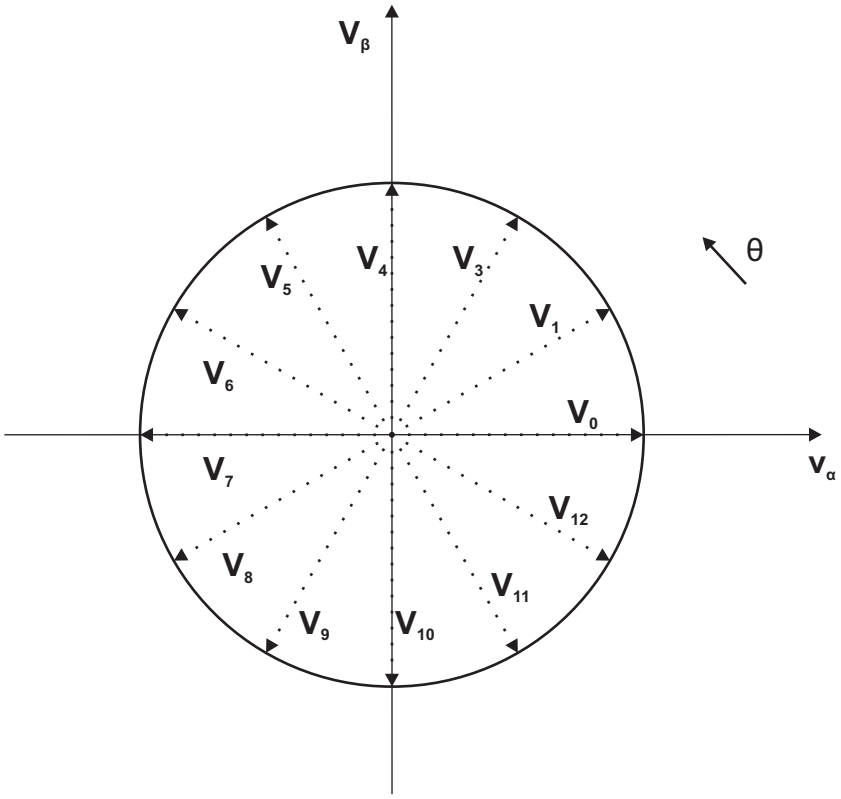

Fig. 6.6 Space vector voltage in the $\alpha\beta$-plane

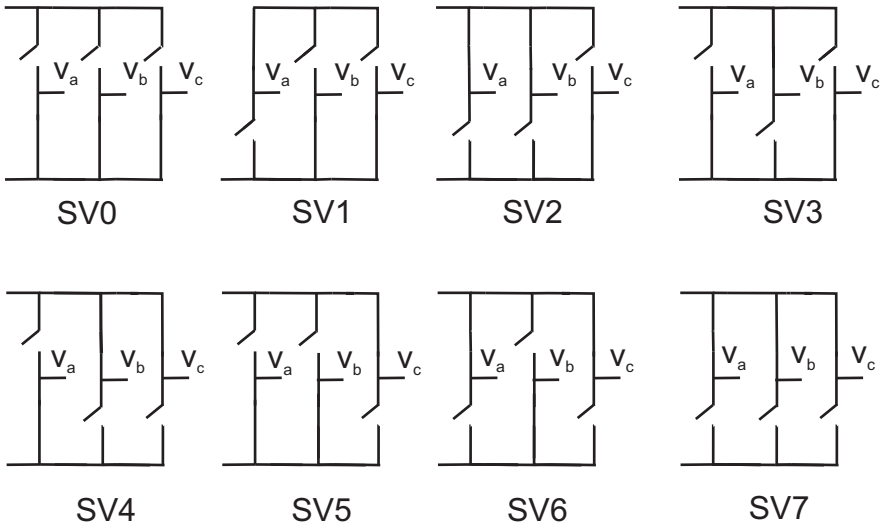

Fig. 6.7 Possible switching states for a three phase inverter

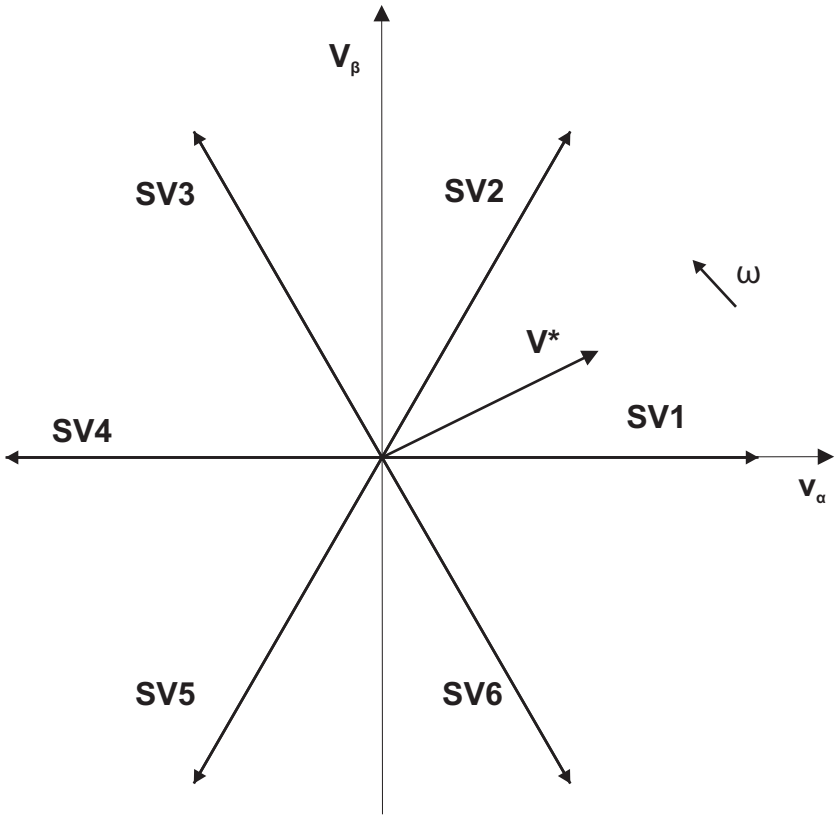

Fig. 6.8 Space vectors for the different switching states. SV0 and SV7 have zero magnitude and are left out in the figure.

$$\mathbf{V}^* = \frac{T_{SV1}}{T_{sw}/2}\mathbf{SV1} + \frac{T_{SV2}}{T_{sw}/2}\mathbf{SV2} \tag{6.8}$$

where T_{SVx} is the time **SVx** is on and T_{sw} is the time of the switching period. The time duration of the zero space vectors can now be defined as

$$T_{SV0} + T_{SV7} = Tsw/2 - T_{SV1} - T_{SV2}. \tag{6.9}$$

However, the time distribution between **SV0** and **SV7** is left undefined as well as the placement of the space vectors. It can be shown, [12], that the space vector placement shown in figure 6.9 should be used in order to achieve the lowest harmonic content. The zero space vectors are symmetrically placed during each switching period as figure 6.9 shows. In order to achieve this pulse pattern a phase leg voltage reference, different from the sinusoidal reference, needs to be determined. For details regarding the derivation of the reference voltage refer to [12]. Figure 6.10 shows the reference voltage for modulation index 0.9. However, as mention in the introduction of this section, optimal harmonic content does not necessarily results in optimal overall efficiency.

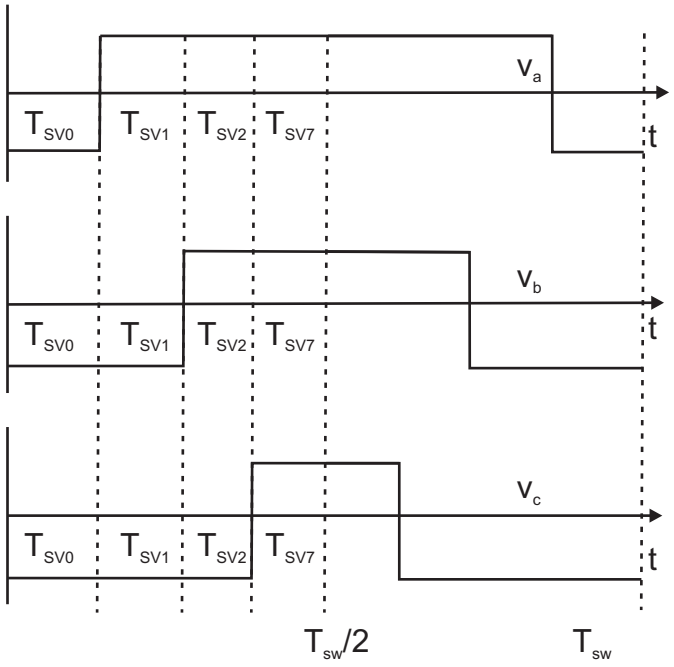

Fig. 6.9 Example of pulse pattern when the voltage reference is located between space vectors **SV1** and **SV2**

It is possible to rearrange the space vector placement in order to decrease the number of switchings and hence decrease the switching losses. [12] explains in detail different discontinues SVM techniques in order to decrease the switching instants. This section will describe the following techniques.

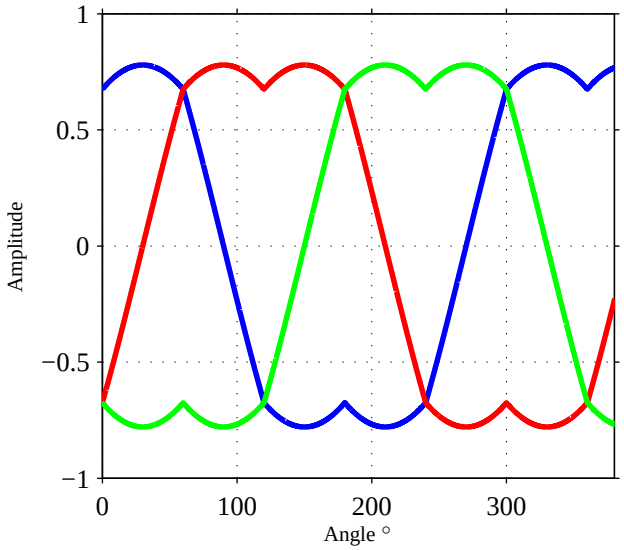

Fig. 6.10 Phase leg reference for SVM

- $120°$ Discontinuous PWM modulation Max DPWMMAX
- $120°$ Discontinuous PWM modulation Max DPWMMIN
- $60°$ Discontinuous PWM modulation Max DPWM60
- $30°$ Discontinuous PWM modulation Max DPWM30lag

DPWMMAX

This technique is called MAX since it only uses the **SV7** as the zero vector. Furthermore, the **SV7** concentrated at each switching period indicated in figure 6.11. It should be noted that the voltage average during the switching period T_{sw} is equal to the one resulting from the pulse pattern used in figure 6.9. During each $120°$ interval, one phase leg is clamped to the positive DC bus of the converter.

DPWMMIN

This technique is similar to DPWMMAX. Instead of using **SV7**, **SV0** is used clamping each phase to the negative DC bus for $120°$. The result in the decreased switching and the harmonic content are identical to DPWMMAX. Figure 6.12 shows the pulse pattern for the same voltage reference as in the previous case.

DPWM60 and DPWM30lag

It is evident that the losses in each device, using $120°$ SVM schemes, are not equally distributed. It is possible to switch equally between the MIN MAX technique. Each phase

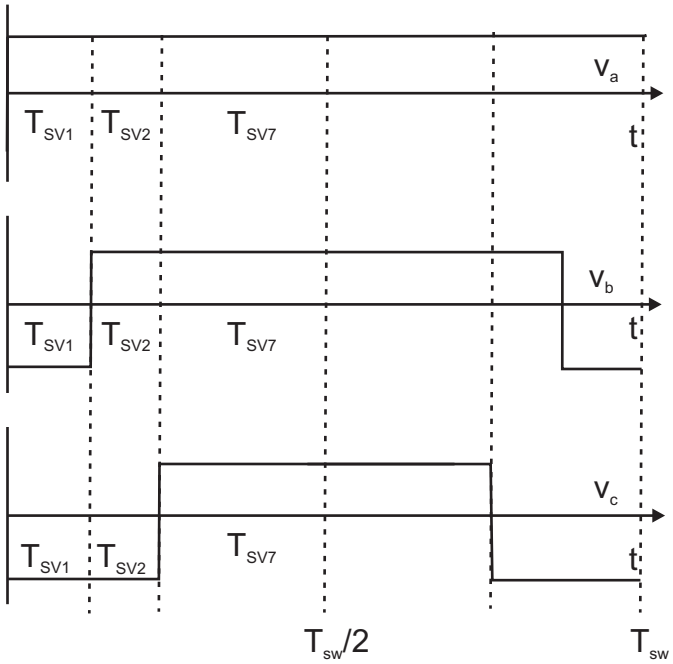

Fig. 6.11 Example of pulse pattern when the voltage reference is located between space vectors **SV1** and **SV2** for DPWMMAX

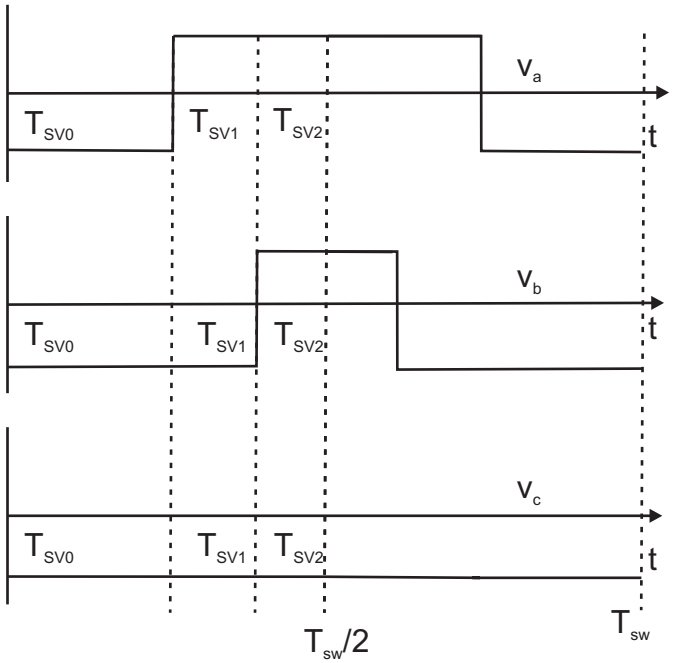

Fig. 6.12 Example of pulse pattern when the voltage reference is located between space vectors **SV1** and **SV2** for DPWMMIN

leg is now clamped to the upper or lower DC bus for 60° instead. The non switching period will now be located around the peak of each phase voltage. As a result, the switching losses will be decreased compared to DPWMMIN or DPWMMAX technique. This is clearly ideal for a resistive load where the switch stop also occurs at the peak current. However, it is possible to center the switch stop anywhere within the 120° interval. If v_a is taken as an example, it is possible to place the 60° switch stop anywhere around **SV1** ($\pm\ \pi/3$). As a result, it is possible to move the switch stop period if the load is inductive in order to decrease the switching losses, i.e to move the switching stop to a position closer to where the current has its maximum. When the load is an IM it is clearly desirable to lag the switching stop by 30°. This ensures a switching stop as close to the maximum current as possible due to the power factor of an IM.

The current ripple, using the same assumption as for 6.3, for the different SVM methods can be expressed as

$$I_{abSVM} = \frac{V_s^2}{4L_\sigma^2}\frac{\Delta T^2}{48}[\frac{3}{2}M^2 - \frac{4\sqrt{3}}{\pi}M^3 + \frac{9}{8}(\frac{3}{2} + \frac{9\sqrt{3}}{8\pi})M^4] \tag{6.10}$$

$$I_{abDPWMMIN} = \frac{V_s^2}{4L_\sigma^2}\frac{\Delta T^2}{48}[6M^2 - \frac{35\sqrt{3}}{2\pi}M^3 + (\frac{27}{8} + \frac{81\sqrt{3}}{64\pi})M^4] \tag{6.11}$$

$$I_{abDPWM60} = \frac{V_s^2}{4L_\sigma^2}\frac{\Delta T^2}{48}[6M^2 - (\frac{45}{2\pi} + \frac{4\sqrt{3}}{\pi})M^3 + (\frac{27}{8} + \frac{27\sqrt{3}}{32\pi})M^4] \tag{6.12}$$

The current ripple of the DPWMMIN, DPWMMAX and DPEM30lag are identical. Figure 6.13 shows the current ripple magnitude of the different PWM schemes as a function of the modulation index M. Note that the constant term is equal in each expression and therefore removed.

6.2.4 Theoretical comparison of different PWM schemes

A Simulink model of a 4kW IM loaded with T=bω^2 has been simulated using different SVM techniques. In order to compare the switching losses it has been assumed that the switching loss at each switching transition is proportional to the current at that time. Furthermore, no loss contribution has been accounted for in the freewheeling diodes. The switch loss component for the different techniques has been calculated as, using SVM as a reference

$$P_{sw\%} = \frac{\sum_{i=1}^{n_1} I_{ix}}{\sum_{i=1}^{n_2} I_{iSVM}} \tag{6.13}$$

where I_{ix} is the current through the transistor at the i th switching instant, n_1 and n_2 is the number of switching instants during one period of the fundamental and x refers to the technique.

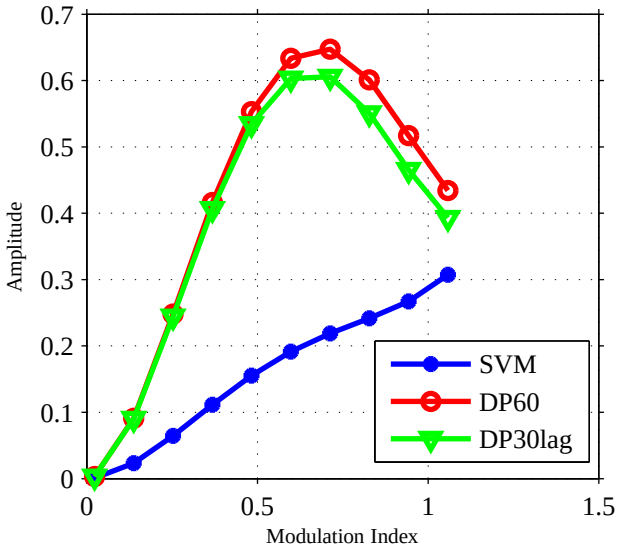

Fig. 6.13 Current ripple for different PWM schemes

Figure 6.14 shows the relation between the different techniques normalized to SVM, which has been chosen as a reference. Figure 6.15 shows the switch loss relation normalized to the maximum loss of SVM. It can be noted that DP30lag has the lowest losses, as expected. The decrease in the switching losses becomes higher at higher load due to the increased power factor which results in a switch stop closer and closer to the maximum current amplitude.

The losses due to harmonics presented in figure 6.13 were not possible to reproduce in the simulations, and will be a topic for future work.

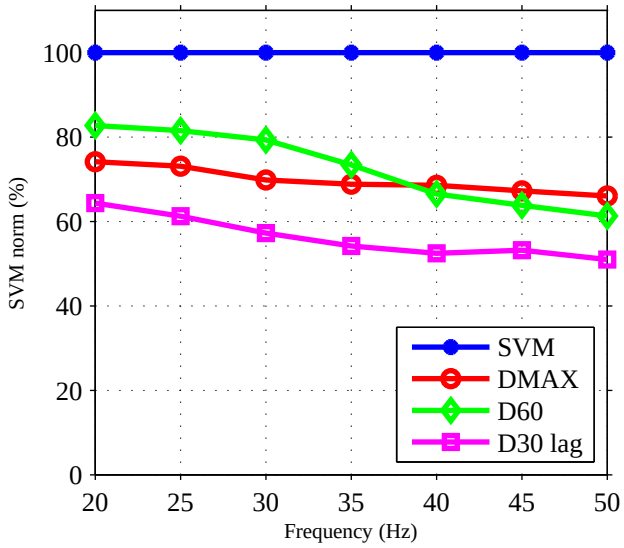

Fig. 6.14 Calculated switching losses, normalized to the SVM at each operating point

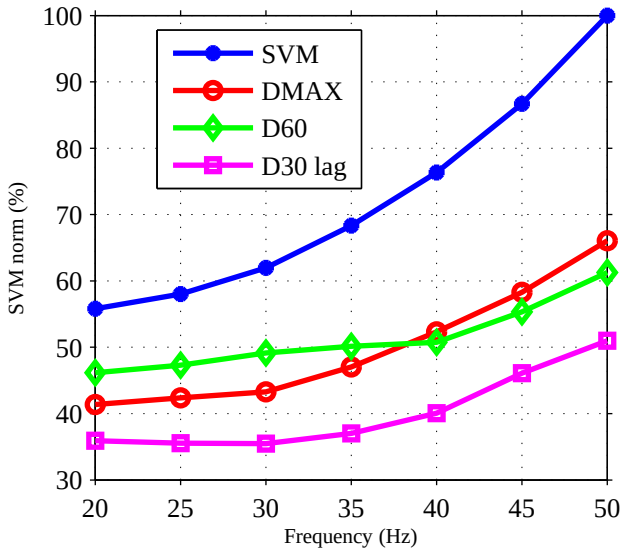

Fig. 6.15 Calculated switching losses, normalized to the SVM loss component at 100%

Chapter 7

Experimental investigation of different PWM control schemes

This chapter will describe the measurement setup and the performed measurements. In addition, a description of the frequency converter layout will be provided.

7.1 Measurement setup

In order to measure the losses in the converter accurately, the temperature was measured on the heat sink of the different components. In order to relate this temperature to a known power dissipation, a DC power supply was connected, short circuited by each component, while the voltage over it and current through it was measured. The temperature was then measured at different known power dissipation and in this way a power loss calibration was obtained.

The input power to the converter, P_{dc} and the input power to the motor P_{IM} has been measured with two different power analyzers, the speed, n, with a tachometer and the shaft torque, T_L was measured with a torque transducer. Table 7.1 lists the measurement equipment and the measured quantities. A schematic over the measurement setup can be seen in figure 7.1 and figure 7.2 shows a part of the laboration se setup.

7.1.1 Converter leg

A circuit diagram of one leg of the converter can be seen in figure 7.3 and figure 7.4 shows a photo of one leg. The freewheeling diodes F1 and F2 are SiC Schottky. This type of diodes where chosen due to its fast switching characteristics and the low recovery according to the manufacturer. The transistors T1 and T2 are MOSFET transistors. The diodes D1 and D2, are Shottky diodes, and connected in series with the MOSFET due to the parasitic diode in the MOSFET which unfortunate was a problem with this type of MOSFET. MOSFET transistors were chosen due to its superior switching speed compared

Table 7.1 Measurement instruments

Type	**Measured quantities**
Norma 61D2 3-phase power analyzer	$I_{a,b,c}$,$U_{a,b,c}$,cos(φ) $P_{a,b,c}$
Yokogawa WT 1600 power analyzer	I_{dc}, U_{dc}, P_{dc}
Lecroy digital Oscilloscope 9304 CM	I_{abc}, U_{abc}, I_{dc}, U_{dc}
Lecroy Differential voltage probe AP032	U_{abc}, U_{dc}
Lecroy Current probe AP015	I_{abc}, I_{dc}
PEM Rogowsky coil CWT03	$I_{T,D}$, I_F
Torque transducer T30 Fn	T_{IM}
Raynger ST 60 ProPlus IR thermometer	$Temperature$

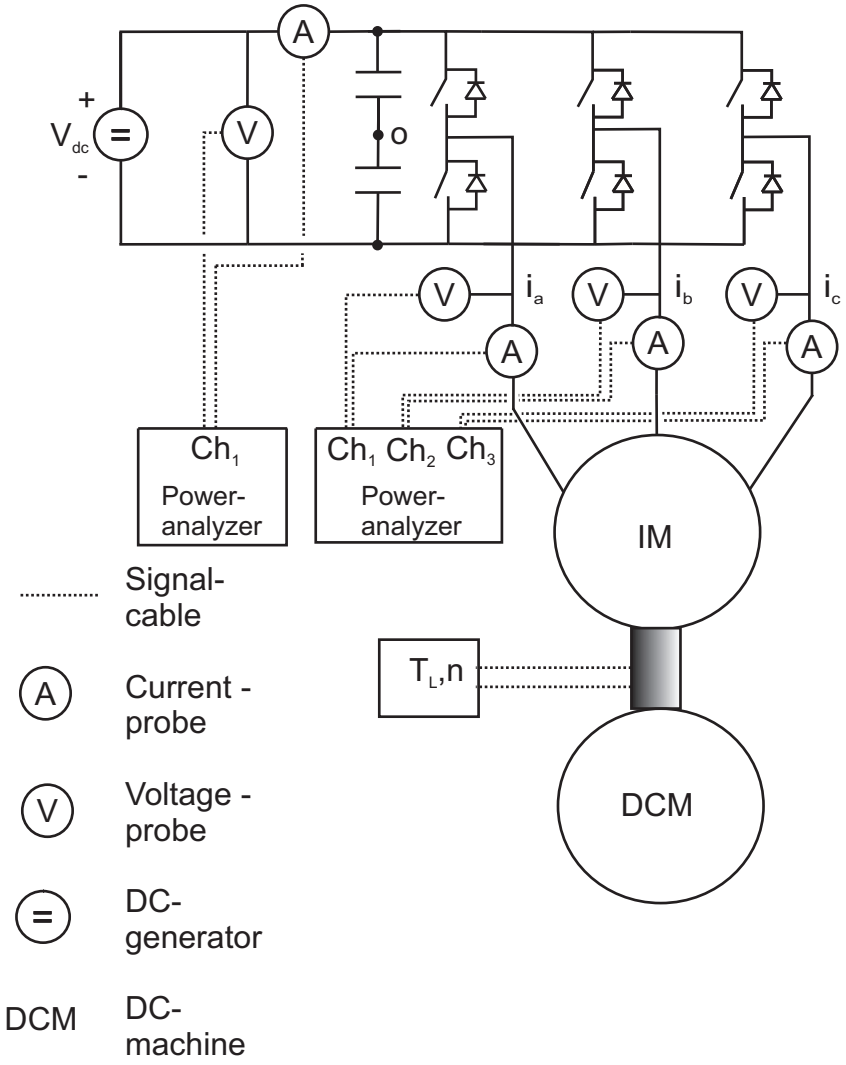

Fig. 7.1 Measurement setup

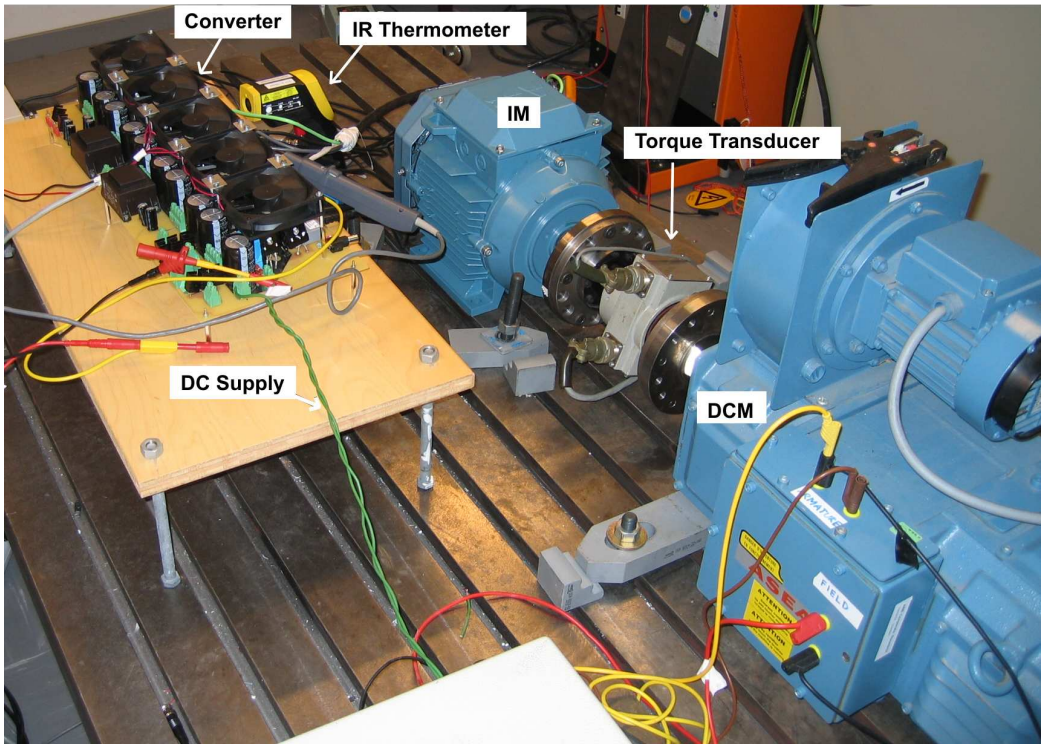

Fig. 7.2 Laboration setup

to its counterparts. The extra inductance, L_{extra}, was added due to some initial problem during the switching transitions causing the transistors to break down. Figure 7.5 shows the original gate voltage with a 70V DC link voltage and a load connected between the midpoint and the negative DC bus. The figure shows the turn off and turn on of T2 and T1 respectively. When the gate voltage applied to T1 increases, an oscillation in the gate voltage applied to T2 appears, caused T2 to turn on. As a result T1 and T2 created a short circuit of the DC voltage causing a high current through the components which in turn resulted in breakdown of the transistors. The oscillations was partly tracked down to D1 and D2, (the reason is yet unknown and will be dealt with in future work). Hence a ferrite bead, L_{extra}, was mounted on one leg on each diode. Table 7.2 lists the different components in the converter where T_j is the junction temperature, I_D the current through the device, V_{GS} the gate voltage, R_{dson} the on-state resistance of the transistor and V_R is the on-state voltage drop of the diodes.

7.1.2 Gate driver

The original gate driver provided a gate voltage of 0-15V. In order to obtain an extra safe margin on the gate voltage on the transistor that was turned off, a capacitor, with a parallel zener diode was connected in series with the gate resistance. The capacitor is charged to the breakdown voltage of the zener diode and results in a corresponding negative voltage

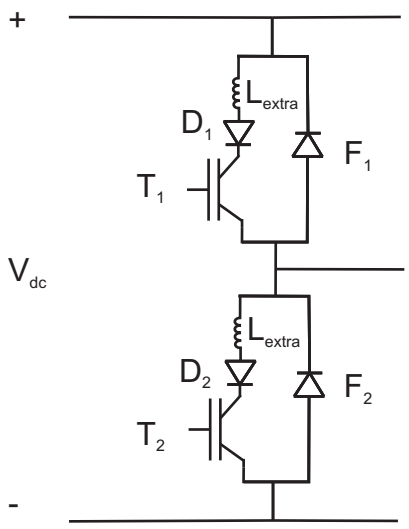

Fig. 7.3 Circuit diagram of one leg in the converter

Table 7.2 Components

Comp.	**Type**	V_{max}	I_{max}	**Condition**	**Value**
T1-T6	MOSFET	600V	60A	I_D=44A, V_{GS}=10V, T_J=25°	R_{dson}=40mΩ
				I_D=44A, V_{GS}=10V, T_J=150°	R_{dson}=110mΩ
D1-D6	Schottky	8V	80A	I_D=40A, T_J=25°	V_f=0.34V
				I_D=40A, T_J=125°	V_f=0.23V
F1-F6	Schottky, SiC	600V	12A	I_D=12A, T_J=25°	V_f=1.5V
				I_D=40A, T_J=150°	V_f=1.7V

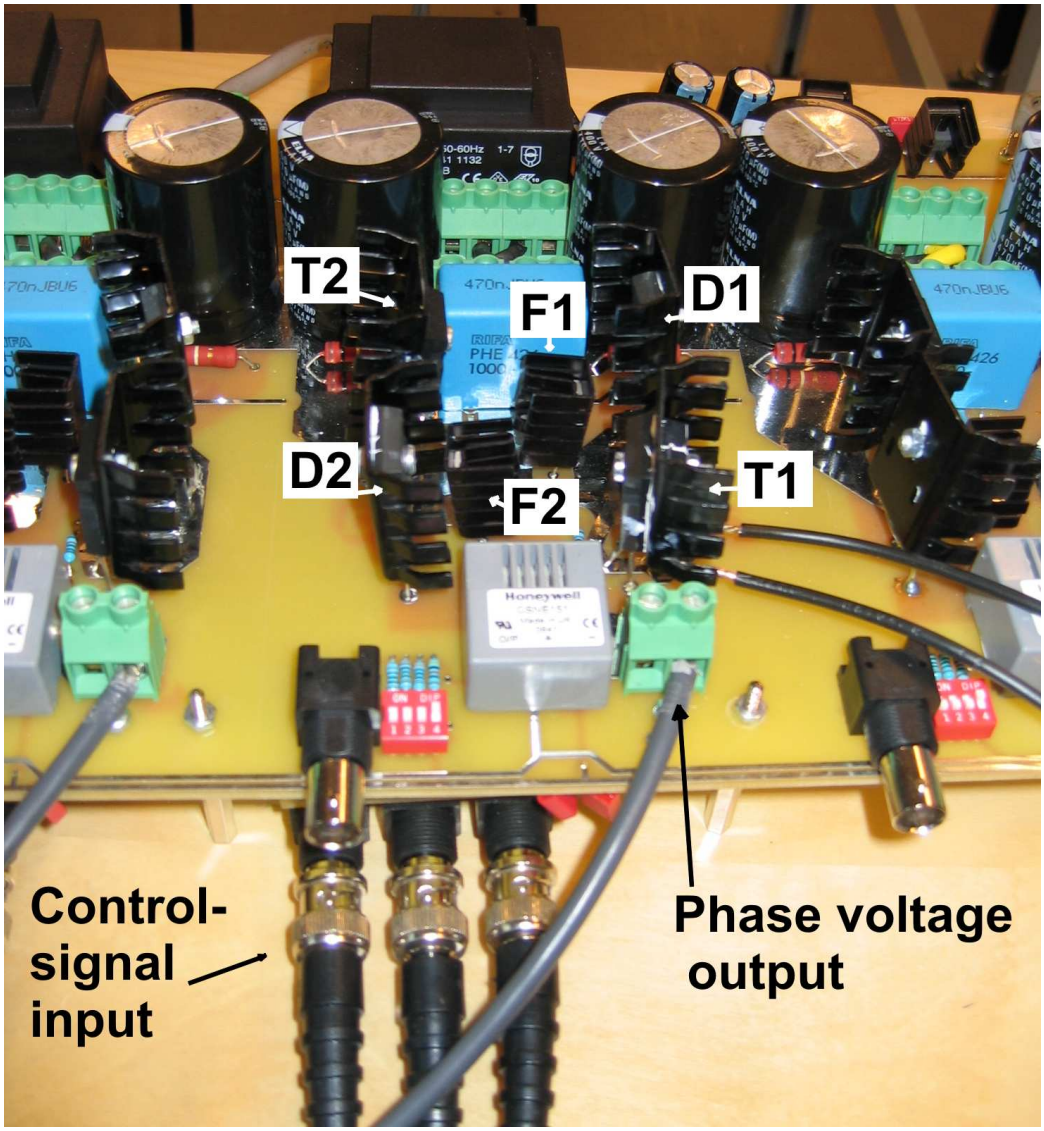

Fig. 7.4 One leg of the converter

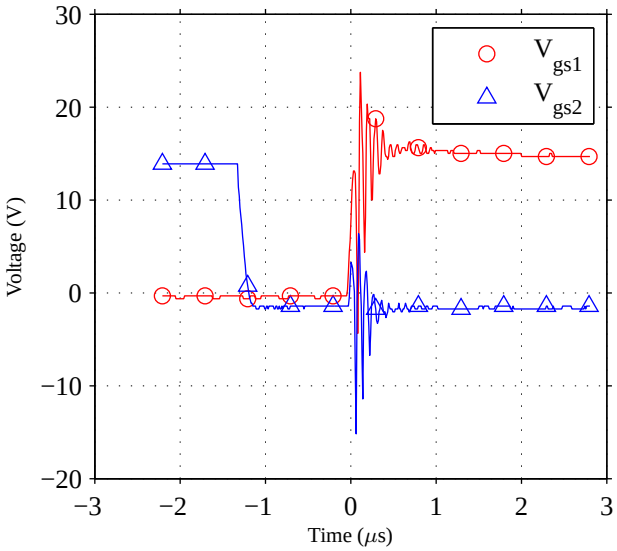

Fig. 7.5 Gate voltage of the upper and lower MOSFET

on the gate at turn off. The DC-level on the gate driver was increased from 15V to 18V and the zener diode was chosen to 4.4V resulting in a +14.6V and -4.4V gate voltage. The capacitor was chosen to 2μF in order to keep a negative voltage on the gate during 20ms which is sufficient for all operating condition during the tests (60° switch stop at 15Hz corresponds to 12ms). It can be noted that the capacitor slows down the gate driver but optimal gate drive design is not the objective of the study presented in this chapter.

Finally, the gate resistance was selected to 4Ω. Figure 7.6 shows the circuit diagram of a part of the the gate driver where G_{d+} and G_{d-} are connected to a totem-pole amplifier arrangement driven by a high and low side gate driver, IR2113. Figure 7.7 shows the gate voltage after the modifications, were the oscillations now are negligible.

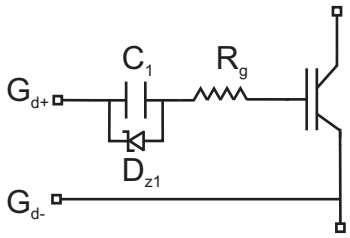

Fig. 7.6 Part of the gate drive circuit after modification

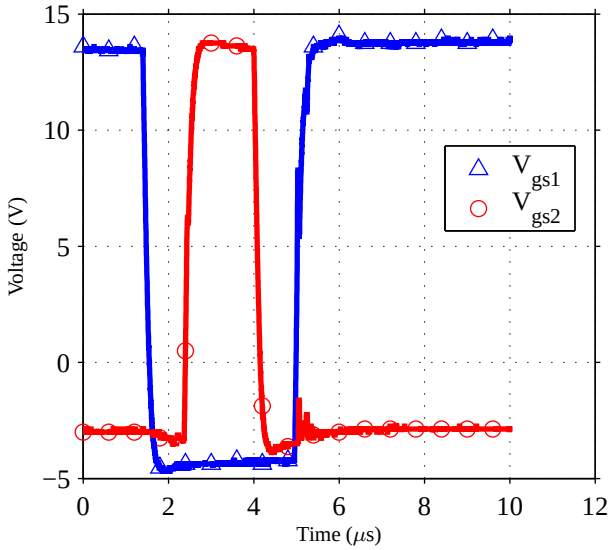

Fig. 7.7 Gate voltage of the upper and lower MOSFET after modification of the gate circuit

7.2 On-state measurement

The on-state measurements were performed in order to investigate the on-state losses in the converter. Each component was connected to a DC power supply, able to deliver a sufficiently high current. The current and the voltage drop across each component was measured. Futhermore, since the voltage drop is temperature dependent, it was desierable to perform the measurement in the same temperature range as for normal operation. Hence, the measurements were performed at approximately 45°C.

Figures 7.8 and 7.9 show the voltage drop across the transistor and and the diode respectively, as a function of current, in the range 0-20A. The data sheet of the transistor states an on-state resistance, R_{dson}, of 45mΩ at $25°$C, 44A drain current and 10V gate voltage. The results of the measurement results in approximately 50mΩ at 20A. However, the temperature during the measurement was $45°$ resulting in a slight increase in R_{dson}.

The measured voltage drop across the diode was 0.27V at 20A. This can be related to the data sheet, which states, a maximum voltage drop of 0.34V at 40A and $25°$, decreasing to 0.23V at $125°$.

The voltage drop over the freewheeling diode was measured in the current range of 0-15A. Figure 7.10 shows the result. The data sheet of the diode states a typical voltage drop of 1.5V at 12A and $25°$ increasing to 1.7 at $150°$.

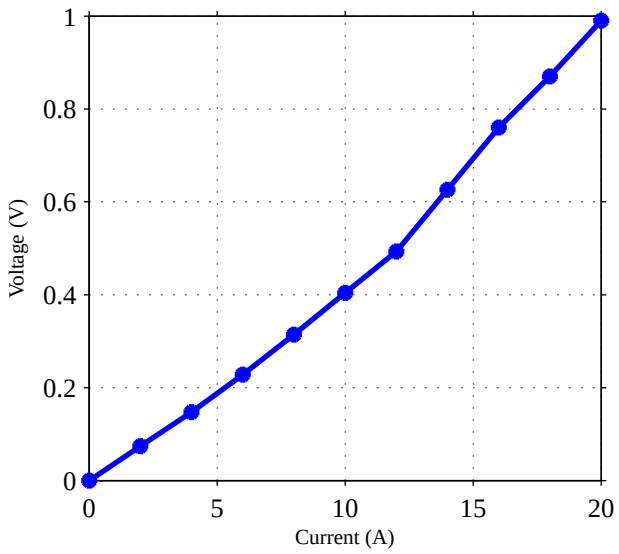

Fig. 7.8 Measured voltage drop across the transistor at $45°$C V_{GS}=14.4V.

The results from the on-state measurement are used together with the the description presented in Section 4.3 in order to estimate the conductive losses in the converter.

Measurements were also performed with short circuited components in order to investigate the conductive losses in the PCB traces of the converter. However, the influence of these losses was found to be negligible.

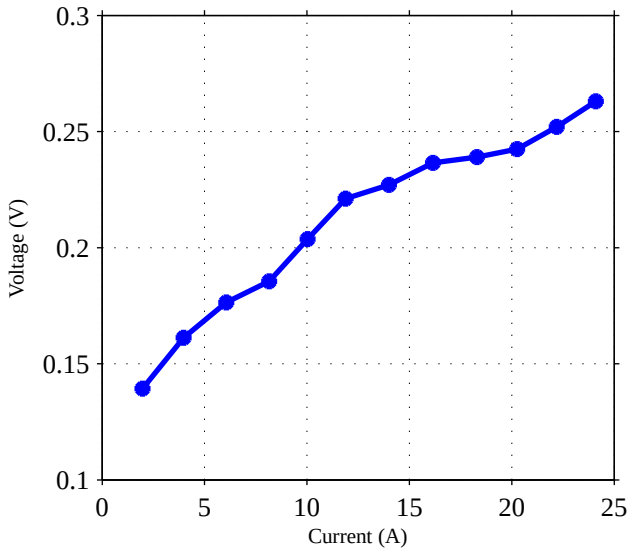

Fig. 7.9 Measured voltage drop across the series diode at $45°$C

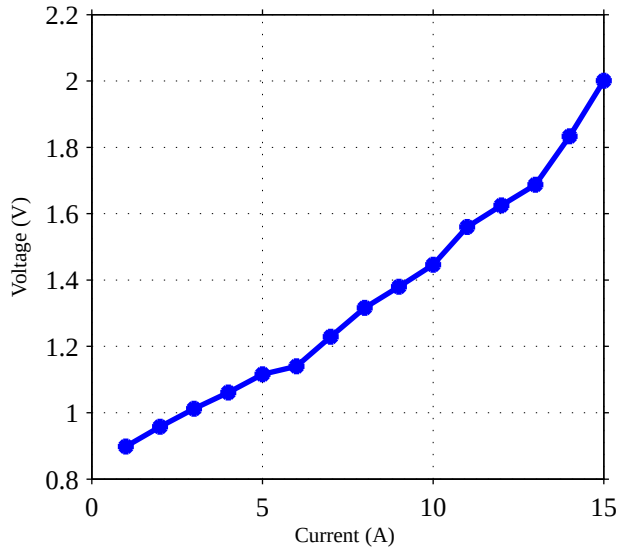

Fig. 7.10 Measured voltage drop and current trough the freewheeling diode at $45°$C.

7.3 Temperature calibration

The losses in each component are obtained by measuring the temperature on each heat sink and relate this to a known power dissipation in the component. Hence, the same connection as for the measurement of the on-state losses is used. The cooling fan of the converter was operating in its lowest state in order to achieve highest possible temperature difference of the components. Higher temperature difference is of course possible without the fan. However, this increases the heat transfer between the components. The temperature of the heat sink was taken after it had stabilized, 6 minutes, and was then cooled down to the ambient temperature before next measurement. This was done in order to have the identical condition between the calibration and the measurements. It should be noted that the temperature of the different heat-sinks affects each other. As a result, it is not possible to make the calibration on one component while the others have the ambient temperature. Hence, each calibration was performed while keeping the closest component at 45°C. This is of course not 100% accurate but decreases the error. Further errors are conductive heat energy in wires between the components. However, the absolute accuracy is not as important as the relative difference between different converter operation points.

7.4 Measurement of switching transitions

The switching transition measurements were performed in order to obtain the switching losses as a function of load current. A 1mH inductance was connected in series with the load, in order to obtain a constant current during the transitions. Figure 7.11 shows the circuit diagram of the connection. The lower transistor was first at its on-state, enough time for the current to reach its steady state. Then a short turn off and turn on pulse were given, (short enough in order to keep the current constant). The voltage was measured across the load, T2 and D2 together with the current through each component. The resistance was changed in order to obtain different load currents.

Figure 7.12 shows the turn on transition of T2. It can be noted that the current through T2-D2 has an overshoot due to the discharge of T1 and F1. The load current is 7.5A and it takes approximately 1μs until it has reached this value. This long duration can be explained by the extra inductance that has been added as described in Section 7.1.1. The inductance will force a current to flow in the T2-D2-DF2 loop as can be seen in figure 7.13.

Figure 7.14 shows the the switching transition when T2 turns off. It can be noted that the voltage has an overshoot before it reaches the DC link voltage. This overshoot results from the stray inductance in the circuit.

Figure 7.16 shows the the switching transition for F1 when T2 turns on. It can be noted that, in contradiction to the data sheet, the current becomes negative for a short period of time before it settles at 0A.

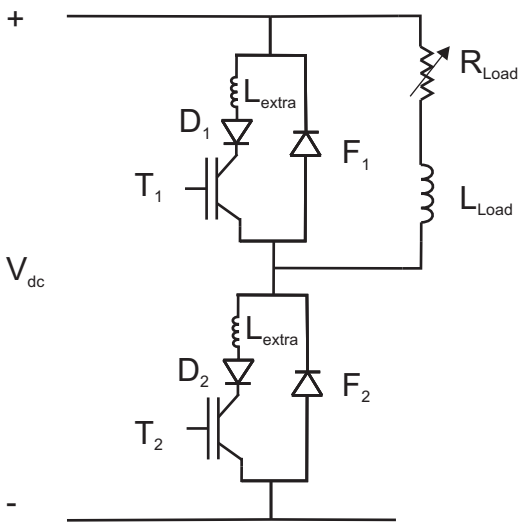

Fig. 7.11 Circuit diagram of one leg in the converter with applied load

Figure7.15 shows the the switching transition for F1 when T2 turns off. It can be noted that there is an oscillation of the current through F1 before it reaches the load current. The reason for this is yet unknown.

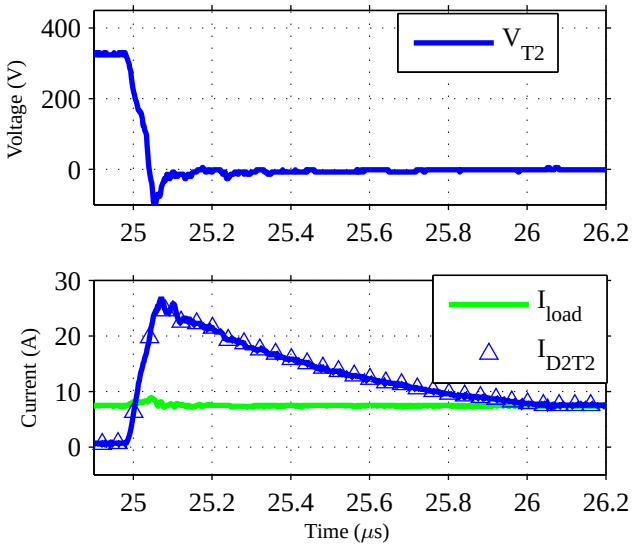

Fig. 7.12 Switching transition for the turn on of T2, for a constant load current of 7.5A

The result from this section is used together with the the description of switching loss calculation in Section 4.3 in order to estimate the switching losses.

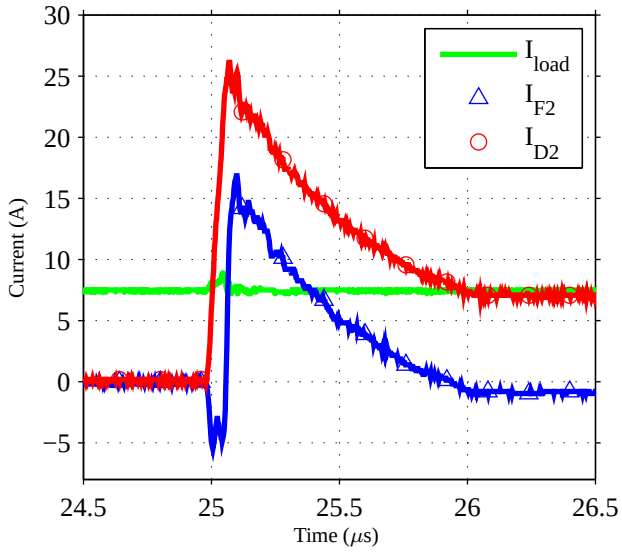

Fig. 7.13 Current through D2 and F2 during turn on of T2 at a load current of 7.5A

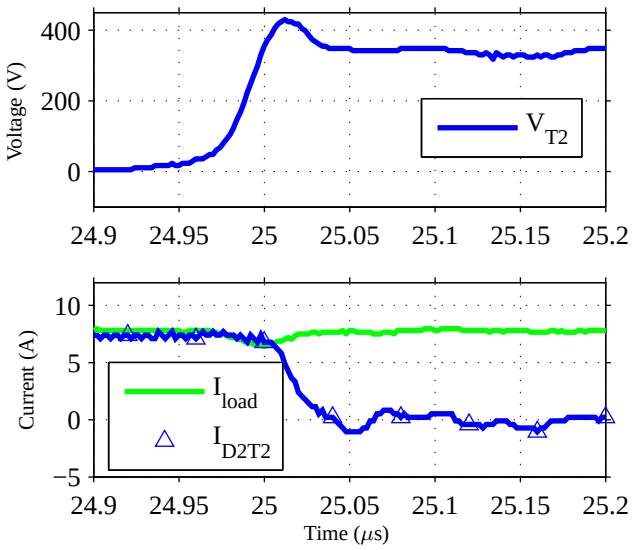

Fig. 7.14 Switching transition for the turn off of T2, for a constant load current of 7.5A

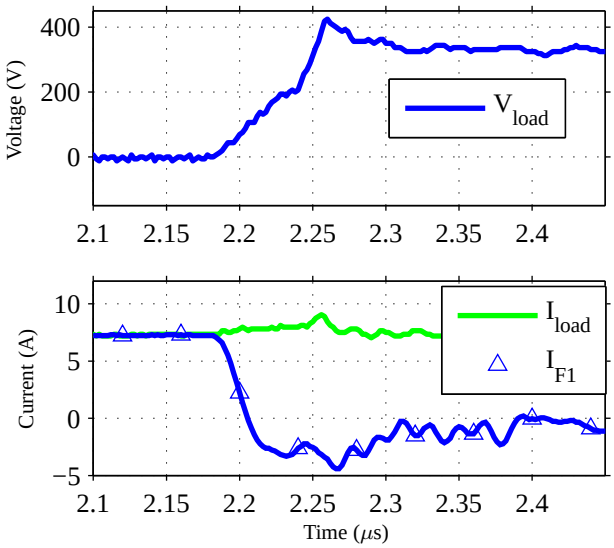

Fig. 7.15 Switching transition for F1 at turn off of T2, for a constant load current of 7.5A

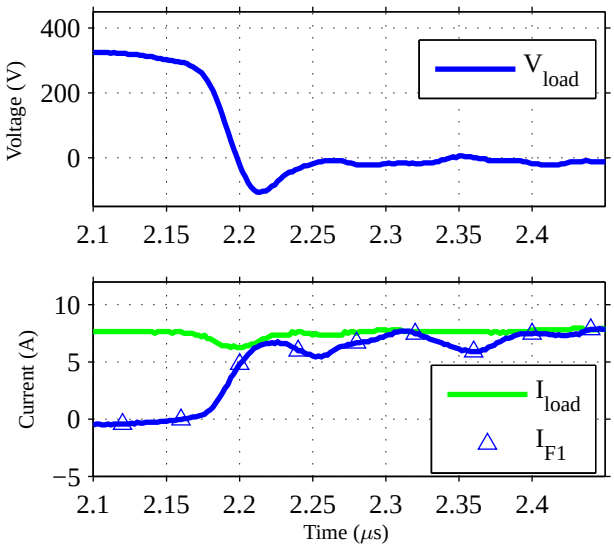

Fig. 7.16 Switching transition for F1 at turn off of T2, for a constant load current of 7.5A

7.5 Measurements of the frequency converter losses at IM operation

This section will present the results from the measurements of the losses in the converter using different switching techniques. The converter is controlled in an open-loop manner with a constant voltage frequency ratio and a constant DC-link voltage of 330V (330 since the motor is delta connected, giving the rated AC voltage for the motor of 230V at 50Hz). Furthermore, the switching frequency is 20kHz during the tests, if not stated otherwise.

A linear load was chosen, T_L=bω, giving rated operation at rated voltage/frequency. The cooling fan of the converter was operated in the same state as during the temperature calibration. Each measurement was performed after 6 minutes of operation followed by 15 minutes of forced cooling. This procedure ensured a stable temperature on each component and enough cooling to retain the ambient temperature of the components at the start of each measurement point. The oncoming sections presents obtained results.

7.5.1 SVM

This section will present the result obtained using SVM. The measurements will be compared with calculation of the different loss components presented in Sections 7.2 and 7.4.

Table 7.3 and 7.4 shows the detailed results from the measurement. Note that the power dissipation in the components presented in Table 7.4 is given for one single component.

Table 7.3 Measurement data

T_{Load} **(Nm)**	**n (rpm)**	V_{fun} **(V)**	**I (A)**	**cos(φ_1)**	P_{IM}	P_{dc}
7.88	437.9	36.6	8.4	0.53	498	600
10.50	584.2	49.3	9.3	0.59	817	933
13.12	730.8	62.3	10.2	0.64	1242	1357
15.75	876.6	74.8	11.2	0.69	1743	1872
18.38	1022	87.3	12.3	0.73	2345	2490
21.00	1167	99.2	13.4	0.76	3023	3182
23.62	1312	111.3	14.5	0.78	3798	3965
26.25	1456	122.8	15.7	0.8	4652	4847

Figures 7.17 show the measured losses in the transistors, T1-T6, together with the different calculated loss components. The calculations were done by using the measured currents and the on-state voltage. P_T P_{swT} and P_{cT} refers to the measured losses, the calculated switching losses and the conductive losses respectively. The results indicates an accurate estimation of the different loss components. However, to strengthen the validity, further measurements have been performed in order to separate the switching and the conductive losses, which will be presented in Section 7.5.2.

Table 7.4 Measurement data

T_{Load} **(Nm)**	ΔT_T (°C)	P_T **(W)**	ΔT_D(°C)	P_D **(W)**	ΔT_F(°C)	P_F **(W)**
7.88	12.5	3.0	17.7	2.0	19.6	4.9
10.50	13.8	3.3	19.3	2.2	22.0	5.8
13.12	17.5	4.0	18.4	2.1	21.6	5.6
15.75	19.6	4.5	19.6	2.3	22.7	6.0
18.38	23.2	5.4	21.3	2.4	22.2	5.8
21.00	26.7	6.2	23.1	2.5	23.3	6.1
23.62	33.2	7.8	26.3	2.7	24.0	6.2
26.25	49.7	11.5	29.0	3.0	25.1	6.4

Figures 7.18 and 7.19 shows the results for the freewheeling diodes, F1-F6, and the series diodes, D1-D6, respectively. It can be noted that the calculated and the measured losses for D1-D6 indicates a fairly accurate estimate. The losses in F1-F6 on the other hand does not show the same trend, possible causes are further analyzed in Section 7.5.2.

Figure 7.20 shows the measured losses with the input output method, meaning that the losses are determined from the difference in the measured input and output power to the converter, together with the calculated and measured losses using the temperature of each component. Note that the the so called bleeding losses, namely the losses in the converter at 330V DC link voltage when the transistors are off, is subtracted from the input power. These losses are approximately 12W and results from the power dissipation in resistors used to discharge the capacitors.

The difference can be explained by the inaccuracy in the measurements. The input and output power is relatively large compared to the losses. For example, the input and output power to the converter are 4847W and 4652W respectively at rated operation. Hence a small error in the measurement results in a large error in the loss components. At least the trend is the same. However, these results clearly indicates the usefulness of the ”temperature method” used here.

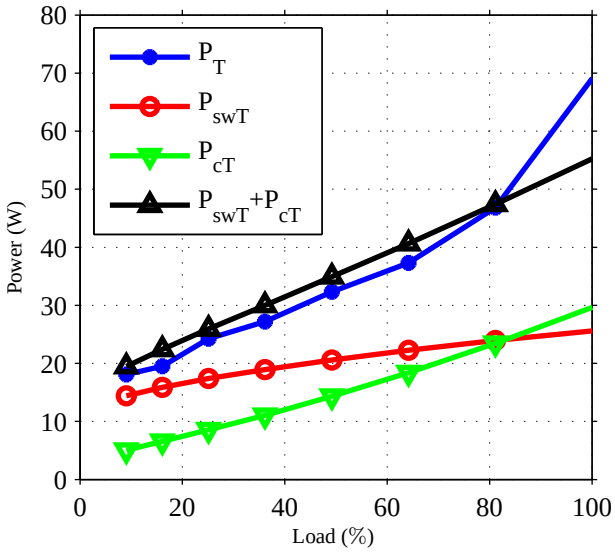

Fig. 7.17 Measured and calculated losses in the transistors (T1-T6)

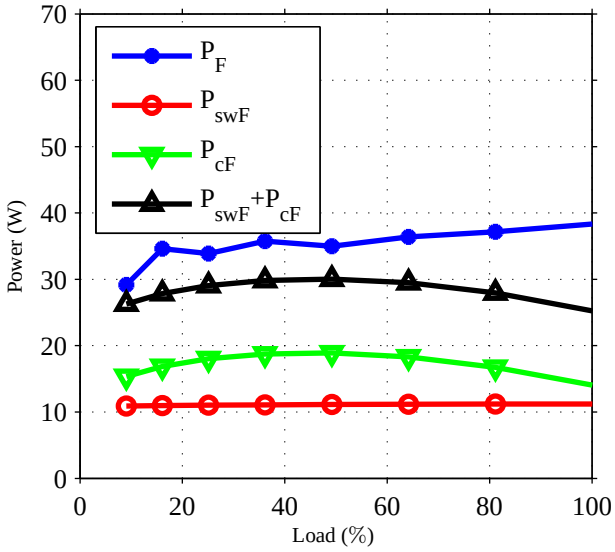

Fig. 7.18 Measured and calculated losses in the freewheeling diodes (F1-F6)

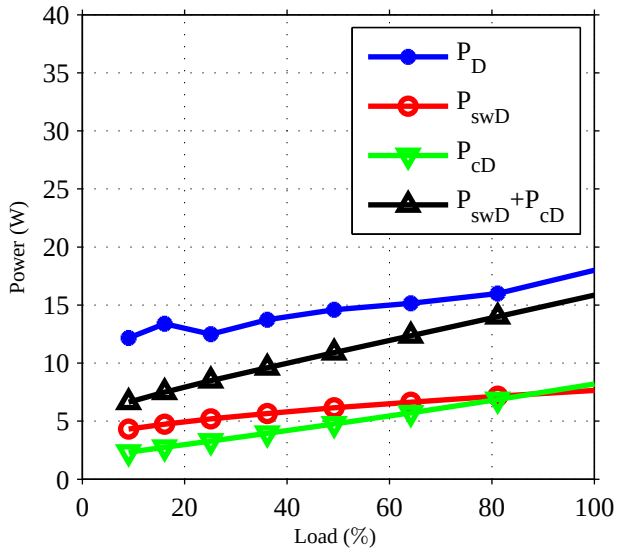

Fig. 7.19 Measured and calculated losses in the diodes (D1-D6)

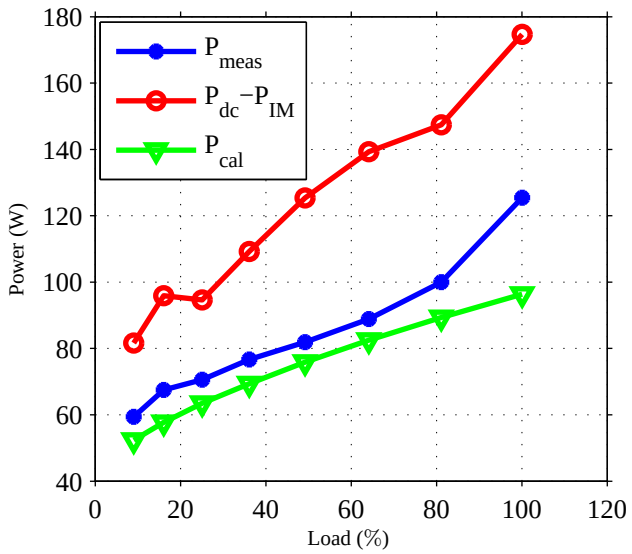

Fig. 7.20 Measured losses using input output method, temperature measurement including bleeding losses and calculated losses

7.5.2 Varying switching frequency

In order to validate the calculations and to investigate the cause of difference between the measured and calculated losses, a series of measurements were performed for a fix load situation using different switching frequencies. The IM was operated at 40Hz and loaded with 21Nm. The same measurement procedure was then performed for switching frequencies in the range of 5kHz to 20kHz with 3kHz increments. Figure 7.21 shows the measured losses in each component together with the linear regression of the measurement points. It should be noted that the voltage decreases with approximately 2% from 5kHz to 20kHz due to the blanking time at each switching instant. However, it was not possible to distinguish any difference in the phase current between the different measurements. Hence, the conductive losses are assumed to be constant and can be obtained from the linear regression. Table 7.5 presents the calculated and the measured conductive losses.

Table 7.5 Conductive losses

Component	Measured (W)	Calculated (W)
T1-T6	20.5	19.3
D1-D6	10.3	5.9
F1-F6	10.9	18.7

It can be concluded that the calculated conductive losses in the transistors are close to the measurement. The cause of the difference in the measurement and calculation for D1-D6 and F1-F6 has not yet been established.

The accuracy in the switching losses can be evaluated by calculating the slope of the linear regression curves and the calculated loss curve. Table 7.6 presents the calculated and the measured slope of the loss curves. Again, the calculated and estimated losses in T1-T6 are close in magnitude. Furthermore, the estimated switching losses in D1-D6 are also fairly close whereas the switching losses in the freewheeling diode differs substantially from the measurement. The reason for this is unknown and is a subject for further research

Table 7.6 Energy loss change with frequency

Component	Measured (W/kHz)	Calculated (W/kHz)
T1-T6	0.92	1.15
D1-D6	0.25	0.34
F1-F6	1.33	0.56

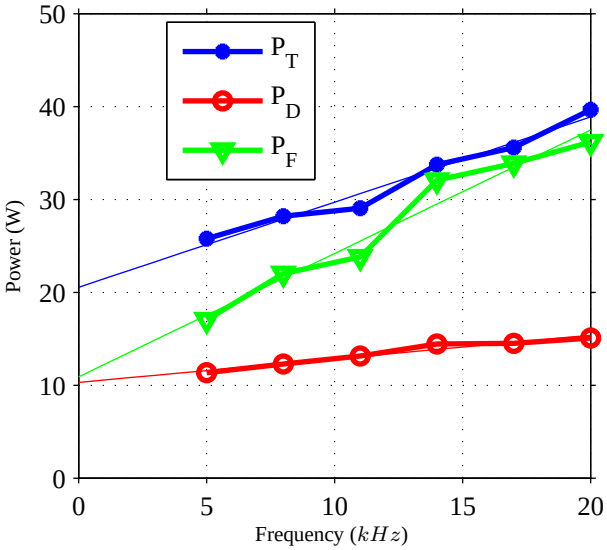

Fig. 7.21 Measured losses in the different components together with a linear regression of the measurement points

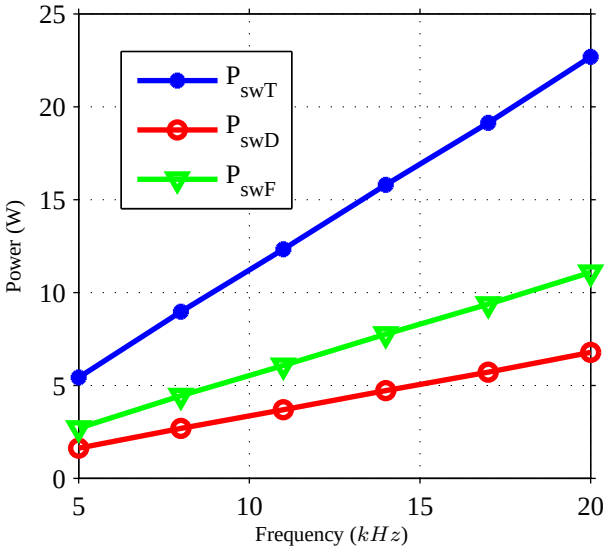

Fig. 7.22 Calculated switching losses for different switching frequencies

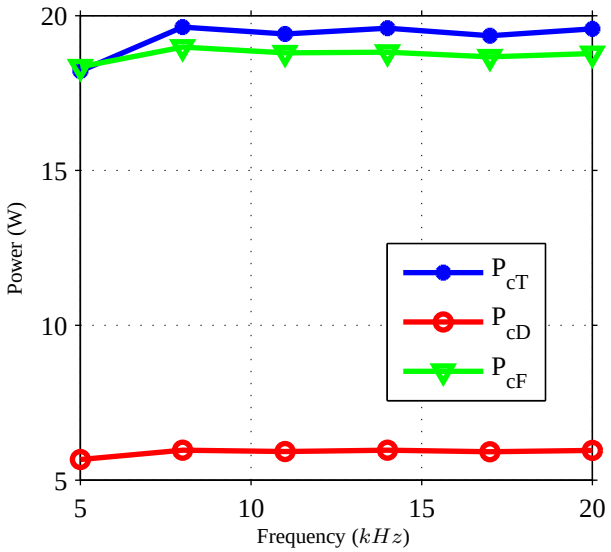

Fig. 7.23 Calculated on-state losses for different switching frequencies

7.5.3 DPWM60 and DPWM30

The same measurements where performed for the switching reduction strategies DPWM60 and DPWM30 presented in Section 6.2.

7.5.4 Comparison of the different switching schemes

The measured losses in the components for the different PWM schemes are presented in figure 7.24. The result clearly shows a decrease in the losses when changing from SVM to DP60 as expected. The losses decreases further for DP30 which also is in correspondence with the expectations.

Figure 7.25 shows the losses normalized to SVM.

In order to compare the measurements with the simulations made in Chapter 6 the losses in T1-T6 are considered. The calculated conductive losses for T1-T6 are subtracted from the measurement, since only the switching losses where accounted for in the simulation. Figure 7.26 shows the measured switching losses together with the simulated switching losses in the transistor. It can be noted that the simulation are in agreement with the measurement. Figure 7.27 shows the efficiency of the converter using the sum of the measured output power and the power dissipation obtained from the temperature measurement as input power.

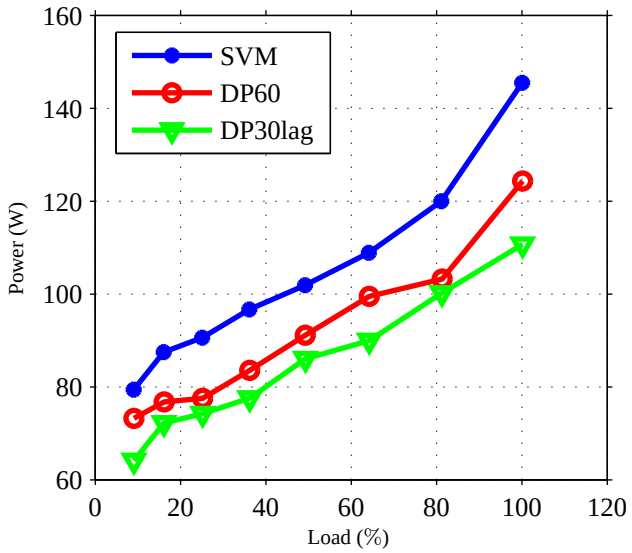

Fig. 7.24 Measured losses at the different switching schemes

The total efficiency of the drive system are presented in figure 7.28. It can be noted that only the load at 30-50Hz are presented in order to see a difference between the different setups.

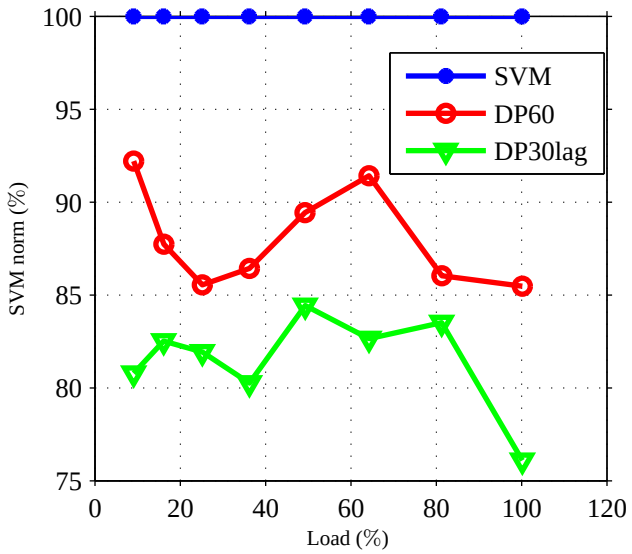

Fig. 7.25 Measured losses normalized to SVM

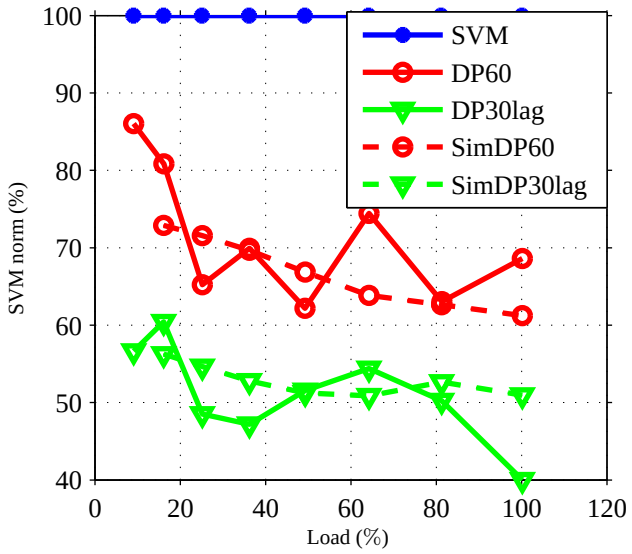

Fig. 7.26 Simulated and measured switching losses in the transistors normalized to SVM

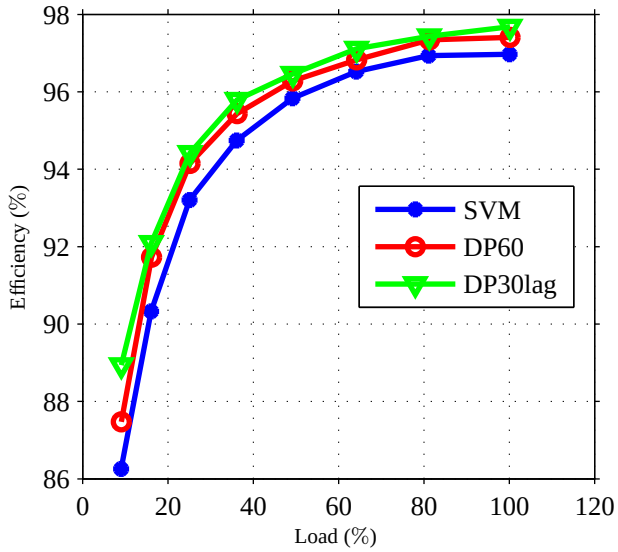

Fig. 7.27 Measured converter efficiency for the different switching schemes

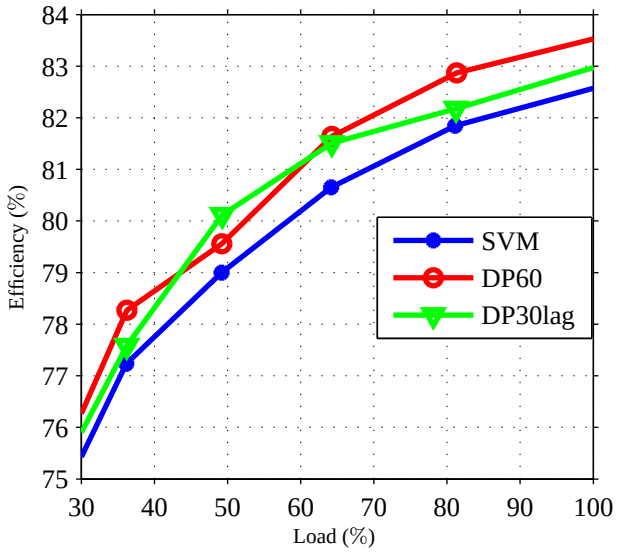

Fig. 7.28 Efficiency of the drive system

7.5.5 Influence on IM efficiency

The difference in the IM efficiency between different switching schemes was not possible to determine from the input output method. However, the difference can be estimated from the difference in harmonic losses between the switching schemes. Figure 7.29 shows the measured harmonic content in the active power. It can be noted that the continues SVM has lower harmonic losses as expected. The maximum difference is however only 5W. However, the result is not in accordance with the theoretical harmonic estimation presented in Chapter 6 which will be a topic for future work.

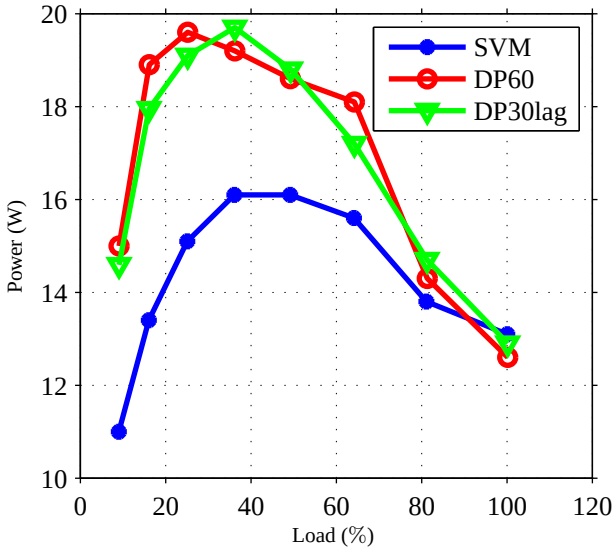

Fig. 7.29 Measured harmonic losses for SVM and DP30lag

In order to validate the accuracy in the harmonic loss measurement, the IM was fed by a generator providing a pure sinusoidal voltage with variable voltage and frequency. Measurement where performed at no load operation, for SVM converter control and for the generator supply, with equal fundamental frequency and voltage. The no load operation was chosen in order to achieve a well defined operation. The measured harmonic losses was negligible when the IM was fed from the generator (< 0.2W). Furthermore, by comparing the fundamental power between the two cases, which ideally should be identical, it was found that the difference was at maximum 3%. The harmonic power component where further in close correlation to the result presented in figure 7.29.

7.6 Efficiency measurements at optimal V/Hz operation

This section will present the results from the measurements made with optimal V/Hz control of the IM.

Measurements where performed for a quadratic load characteristic, T_L=bω^2, having rated torque at rated speed. Figure 7.30 show the efficiency for constant V/Hz and for optimal V/Hz ratio together with the simulated result presented in Chapter 6.

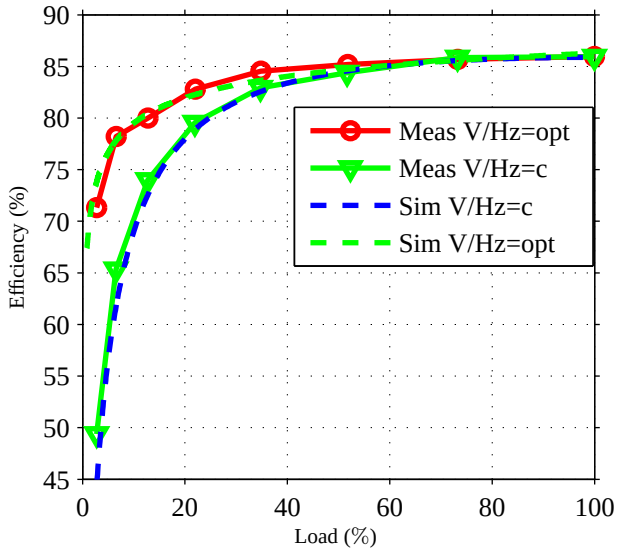

Fig. 7.30 Measured and calculated efficiency using constant V/Hz and optimal V/Hz control

Chapter 8

Energy potential savings for different load profiles

This chapter will use the theory presented in previous chapters in order to estimate the saving potential for different load profiles, associated to various HVAC applications. Different motor controls, motor designs and dimensioning aspects will be considered.

8.1 Energy consumption calculation

The annual energy consumption of a drive system can be calculated as

$$W = \int_0^{8760} p_{in}(t)dt \tag{8.1}$$

where $p_{in}(t)$ is the power demand as a function of time and 8760 is the number of hours during a year. The electric input power to the drive system and the time duration of each load situation will be determined from the load profiles described in Chapter 2. Each profile consists of a different number of constant levels resulting in different power demands. Given each power demand and time distribution, the energy consumption can be calculated as

$$W = \int_0^{t_1} P_1 + \int_0^{t_2} P_2 + ... + \int_0^{t_n} P_n \tag{8.2}$$

wheret_1,t_2.....t_n is the time duration of the electric power input P_1,P_2.....P_n.

8.2 Induction motor drive setups

Chapters 6 and 7 analyzed different setups of an IM drive. The loss model valid for different energy labels, eff1-eff3, using constant and optimal V/Hz control will be used in order to estimate the potential savings for different load profiles.

For the applications described in this thesis, it is assumed that the pump/fan speed is proportional to the flow, according to the affinity laws. This means that it is assumed that the torque demand of the pump/fan is proportional to the square of flow. Assuming a constant pump/fan efficiency, the torque speed demand of the driving motor can be derived from a given load profile, **Q**,

$$\mathbf{n} = n_N \frac{\mathbf{Q}}{Q_{max}} \tag{8.3}$$

$$\mathbf{T} = T_N \frac{\mathbf{Q}^2}{Q_{max}^2} \tag{8.4}$$

where n_N and T_N is the rated speed and torque respectively and Q_{max} is the maximum flow resulting in rated motor operation.

In order to investigate the influence of IM dimensioning, the load demand, using the same pump/fan speed, will be decreased, meaning that the torque demand of the puump/fan will be decreased. The dimensioning will be referred to as the percentage of the original flow demand, e.g. a dimensioning of 80% corresponds to a decrease of the flow to 80% which means that the torque will decrease to 64% of its original value.

It should also be noted that in order to compare the different types of energy labels, identical operating points needs to be considered. Hence, the input parameters are the speed and torque demand, where the maximum is set to 1435 rpm and 26.6Nm corresponding to rated operation for the eff3 IM. As a result, the same operating point for the eff2 and eff1 IM will result in a slight overload since the frequency needs to be decreased 0.3-0.5Hz from the rated frequency.

Since the number of different IM ratings are limited the standard ratings of 1.1kW, 1.5kW, 2.2kW, 3kW 4kW are considered. The calculations are based on the 4kW IM and scaled to fit for the different machines. Hence, it should be noted that the efficiency is assumed to be identical for a fixed percentage of rated load. As a result, the savings made by moving down in motor size is slightly overestimated since the actual efficiency decreases with decreased motor rating.

The following subsections provides the results for different load profiles.

8.2.1 Load profile A

Load profile A was presented in Chapter 2 describing a two level load operating at 100% for two thirds of the time and at 50% for one third of the time.

Figure 8.1 shows the energy consumption for different IM setups using an eff3 with constant V/Hz control as a reference. First the eff3 IM is replaced by an eff1 IM with the same rating resulting in a 4-7% decrease in energy consumption. The next step is to move from 4kW rating to a lower rating when possible. The difference becomes evident when the dimensioning percentage decreases. Finally, both the IM and control of the IM is changed which results in the largest decrease in energy consumption. It should be noted that the consumption of the 4kW eff1 with optimal V/Hz control becomes almost identical to the smaller ratings with optimal control. This is due to the fact that the calculation for the smaller IM ratings are derived from the 4kW IM. Hence, since decreased IM rating in practice results in a decrease in efficiency, over dimensioning actually results in a lower energy consumption if the oversized IM is operated at optimal V/Hz.

Cost analysis

The largest saving is provided when both the IM and the frequency converter is replaced. However, this also results in the largest investment. Hence, the saving potential must be related to the initial cost. It is here assumed that a frequency converter and a eff3 IM costs 1000 SEK/kW. It is further assumed that an eff1 IM costs 1500 SEK/kW and an eff2 1250 SEK/kW. The annual saving between the eff3 and eff1 class in SEK, where it is assumed that 1kWh costs 1 SEK, can be found in figure 8.2.

In order to include interest rate in the investment, the following expressions can be used in order to calculate the payback time and the total saving,

$$T_p = \frac{I_n + \sum_{n=1}^{N}(I_n - \frac{I_n}{N}n)\frac{r}{100}}{W_{save}W_{cost}} \tag{8.5}$$

$$Saving = W_{save}W_{cost}(T_{Life} - T_p) \tag{8.6}$$

where T_p is the payback time (years), I_n is the investment (SEK), r is the interest rate (%), W_{save} is the annual saving (SEK), W_{cost} price of 1kWh (SEK) and T_{Life} is the life time of the drive system (years).

Another important fact to consider is if the drive system are to be replaced, e.g due to renovation. In that case, the cost difference between the different choices are of interest, not the total investment, this of course reduces the payback time substantially. Table 8.1 presents the payback time and the total savings that can be made assuming 20 years of operation and a 5% interest rate. Note that the investment is accounted for in the total saving. In the case where the eff2 and eff1 IM are considered, only the price difference between the different choices are accounted for, in order to investigate if there is any reason for choosing an eff2 IM instead of an eff1 IM.

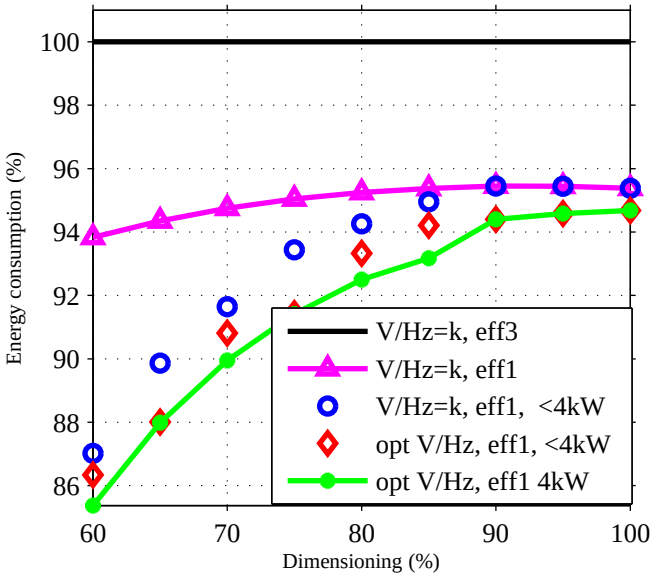

Fig. 8.1 Potential energy savings for load profile A

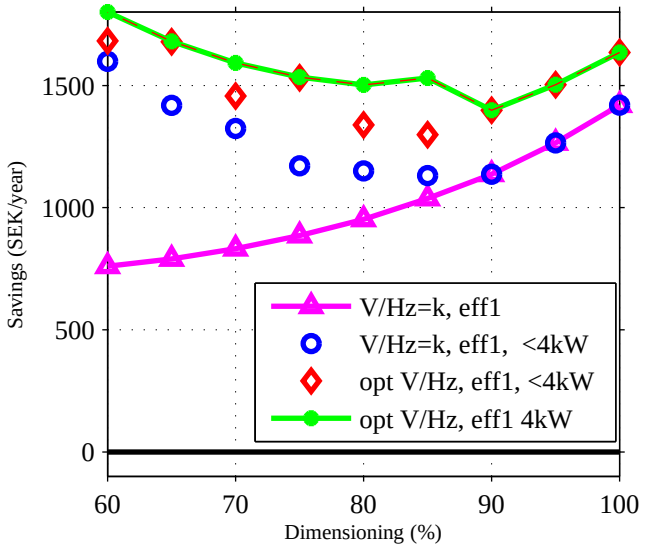

Fig. 8.2 Potential annual savings in SEK for load profile A

Table 8.1 Saving potential with load profile A

Replacement	**Dim. (%)**	I_e	T_p	**Tot. saving**	**Tot. energy cost**
eff3, V/f=k→ eff1, V/Hz=k	100	6 000	6	20 000	589 000
eff3, V/f=k→ eff1, V/Hz=k	80	6 000	9	12 000	385 000
eff3, V/f=k→ eff1, V/Hz=k	60	6 000	10	8 000	234 000
eff3, V/f=k→ eff1, opt V/Hz	100	10 000	9	18 000	585 000
eff3, V/f=k→ eff1, opt V/Hz	80	10 000	10	15 000	375 000
eff3, V/f=k→ eff1, opt V/Hz	60	10 000	11	21 000	215 000
eff2, V/Hz=k→ eff1, V/Hz=k	100	1 000	2	17 000	589 000
eff2, V/Hz=k→ eff1, V/Hz=k	80	1 000	3	8 000	385 000
eff2, V/Hz=k→ eff1, V/Hz=k	60	1 000	4	6 000	234 000
eff2, opt V/Hz→ eff1, opt V/Hz	100	1 000	2	16 000	585 000
eff2, opt V/Hz→ eff1, opt V/Hz	80	1 000	3	7 000	375 000
eff2, opt V/Hz→ eff1, opt V/Hz	60	1 000	6	3 000	215 000

8.2.2 Load profile B

Load profile B was presented in Chapter 2 and describes a VAV load. Figure 8.3 shows the energy consumption for different IM setups using an eff3 with constant V/Hz control as a reference. The result becomes similar to that of the load profile A.

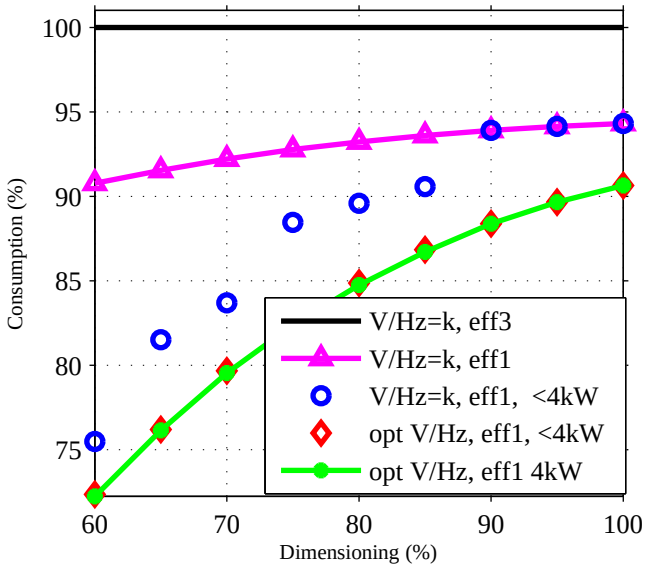

Fig. 8.3 Potential energy saving for load profile B

Cost analysis

An identical cost analysis made for load profile A is presented in figure 8.4 and Table 8.2.

Table 8.2 Saving potential with load profile B

Replacement	**Dim. (%)**	I_e	T_p	**Tot. saving**	**Tot. energy cost**
eff3, V/Hz=k→ eff1, V/Hz=k	100	6 000	11	7 000	248 000
eff3, v/Hz=k→ eff1, V/Hz=k	80	6 000	13	5 000	170 000
eff3, V/Hz=k→ eff1, V/Hz=k	60	6 000	14	4 000	110 000
eff3, V/Hz=k→ eff1, opt V/Hz	100	10 000	12	10 000	239 000
eff3, V/Hz=k→ eff1, opt V/Hz	80	10 000	11	13 000	155 000
eff3, V/Hz=k→ eff1, opt V/Hz	60	10 000	9	29 000	89 000
eff2, V/Hz=k→ eff1, V/Hz=k	100	1 000	4	6 000	248 000
eff2, V/Hz=k→ eff1, V/Hz=k	80	1 000	5	4 000	170 000
eff2, V/Hz=k→ eff1, V/Hz=k	60	1 000	6	3 000	110 000
eff2, opt V/Hz→ eff1, opt V/Hz	100	1 000	4	5 000	239 000
eff2, opt V/Hz→ eff1, opt V/Hz	80	1 000	7	3 000	155 000
eff2, opt V/Hz→ eff1, opt V/Hz	60	1 000	12	1 000	89 000

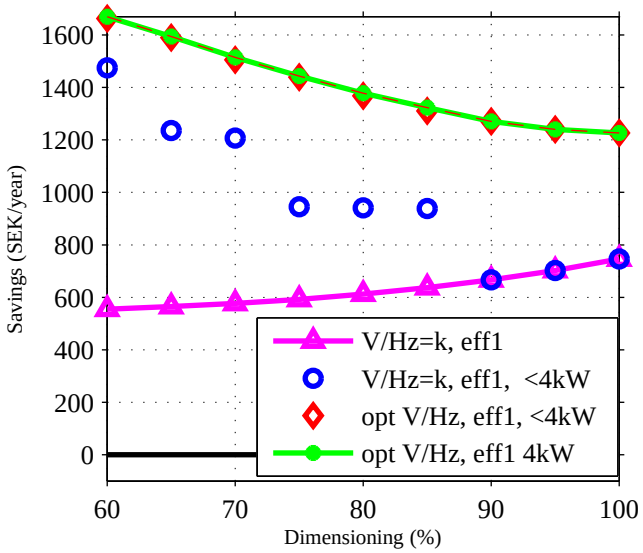

Fig. 8.4 Annual potential saving for for load profile B

8.2.3 Load profile C

Load profile C describes a load with a low load demand during 80% of the time and 100% load demand for 20% of the time. Figure 8.5 shows the same setups as for profile A and B. In this case only the maximum load demand is decreased when the dimensioning are considered, since the 20% load demand already is extremely low.

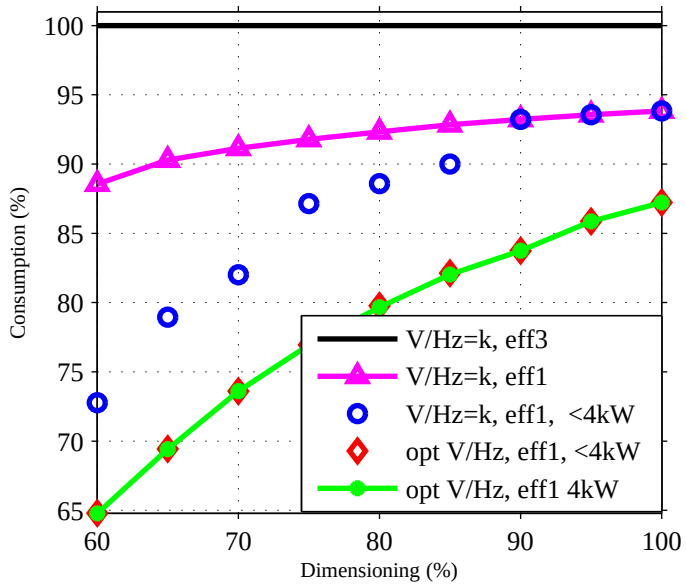

Fig. 8.5 Potential saving for load profile C

Cost analysis

An identical cost analyze made for load profile A and B is presented in figure 8.6 and Table 8.3.

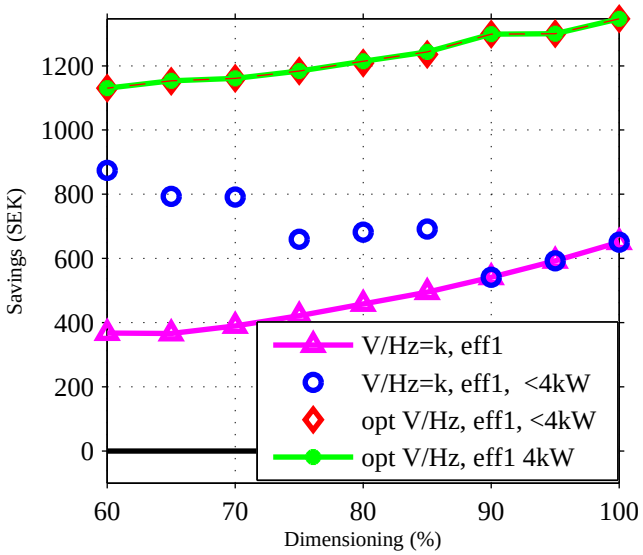

Fig. 8.6 Annual potential saving for load profile C

Table 8.3 Saving potential with load profile C

Replacement	**Dim. (%)**	I_e	T_p	**Tot. saving**	**Tot. energy cost**
eff3, V/Hz=k→ eff1, V/Hz=k	100	6 000	13	5 000	198 000
eff3, V/Hz=k→ eff1, V/Hz=k	80	6 000	16	2 000	119 000
eff3, V/Hz=k→ eff1, V/Hz=k	60	6 000	20	0	72 000
eff3, V/Hz=k→ eff1, opt V/Hz	100	10 000	11	12 000	185 000
eff3, V/Hz=k→ eff1, opt V/Hz	80	10 000	12	10 000	105 000
eff3, V/Hz=k→ eff1, opt V/Hz	60	10 000	12	9 000	57 000
eff2, V/Hz=k→ eff1, V/Hz=k	100	1 000	4	6 000	198 000
eff2, V/Hz=k→ eff1, V/Hz=k	80	1 000	6	3 000	119 000
eff2, V/Hz=k→ eff1, V/Hz=k	60	1 000	9	2 000	72 000
eff2, opt V/Hz → eff1, opt V/Hz	100	1 000	5	4 000	185 000
eff2, opt V/Hz → eff1, opt V/Hz	80	1 000	10	2 000	105 000
eff2, opt V/Hz→ eff1, opt V/Hz	60	1 000	15	500	57 000

8.2.4 Load profile D

Load profile D describes a constant load demand 100% of the time. Figure 8.7 shows the same setups as for profile A , B and C.

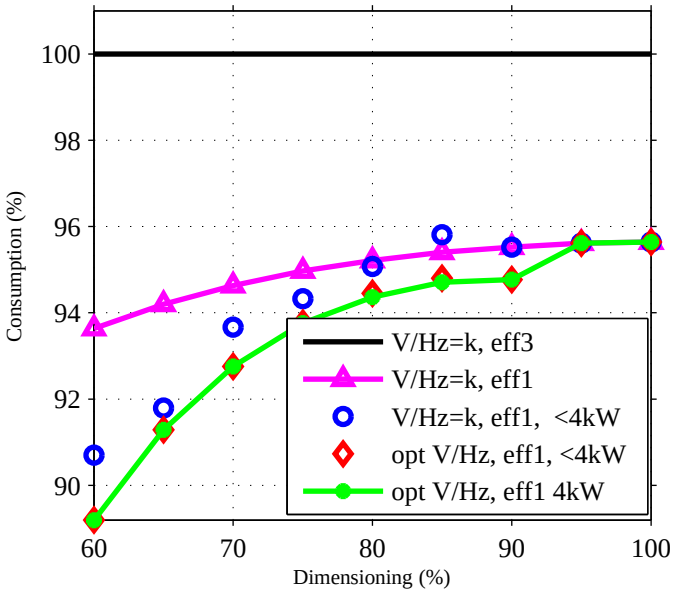

Fig. 8.7 Potential saving for load profile D

Cost analysis

An identical cost analyze made for load profiles A-C is presented in figure 8.8 and Table 8.4.

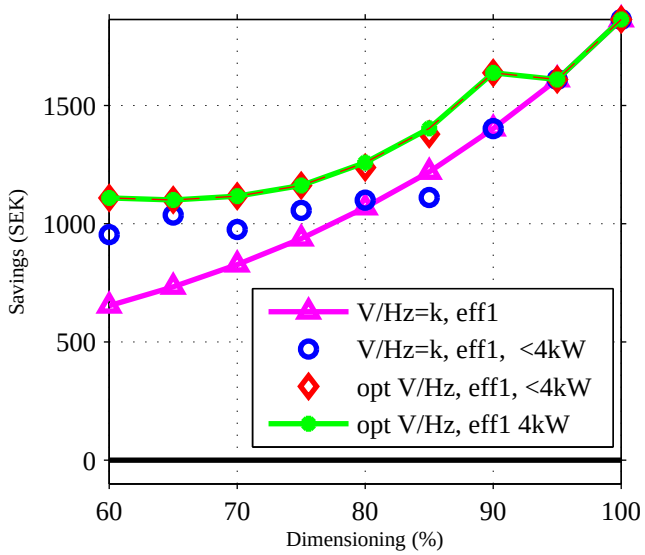

Fig. 8.8 Annual potential saving for load profile D

Table 8.4 Saving potential with load profile D

Replacement	**Dim. (%)**	I_e	T_p	**Tot. saving**	**Tot. energy cost**
eff3, V/Hz=k→ eff1, V/Hz=k	100	6 000	5	28 000	821 000
eff3, V/Hz=k→ eff1, V/Hz=k	80	6 000	8	14 000	426 000
eff3, V/Hz=k→ eff1, V/Hz=k	60	6000	12	5 000	192 000
eff3, V/Hz=k→ eff1, opt V/Hz	100	10 000	8	22 000	821 000
eff3, V/Hz=k→ eff1, opt V/Hz	80	10 000	12	10 000	424 000
eff3, V/Hz=k→ eff1, opt V/Hz	60	10 000	13	7 000	184 000
eff2, V/Hz=k → eff1, V/Hz=k	100	1 000	1	23 000	821 000
eff2, V/Hz=k→ eff1, V/Hz=k	80	1 000	2	11 000	426 000
eff2, V/Hz=k→ eff1, V/Hz=k	60	1 000	5	5 000	192 000
eff2, opt V/Hz→ eff1, opt V/Hz	100	1 000	1	23 000	821 000
eff2, opt V/Hz→ eff1, opt V/Hz	80	1 000	3	9 000	424 000
eff2, opt V/Hz→ eff1, opt V/Hz	60	1 000	5	4 000	184 000

8.3 Evaluation of the potential saving

Load profiles A-D covers a wide range of different possible load profiles. The largest saving with an IM replacement is when the load demand is high. This becomes evident for load profile D where the load demand is high during the whole time interval. As the load demand decreases, the savings of replacing the IM decreases. The extreme case was shown with load profile C where the payback time came close to break even for a poor dimensioning. The opposite is valid for the optimal control of the IM. However, even if the energy savings are large relative to the constant V/Hz control at light load, the energy cost decreases with decreasing load. Hence, the savings does not necessarily increase as the load decreases.

When the system are to be replaced and the choice of IM is eff2 or eff1, the eff1 is the overall best choice. Again, the payback time is shorter for an application with high load demand but even for the extreme case, load profile C, savings can be made.

The analysis regarding dimensioning of the IM showed that the potential savings decreases when a smaller IM rating is used, provided that the control is optimal.

Chapter 9

Bearing currents in Induction Motor drives

The increased use of inverter driven drive systems during the last decade has increased the problem related to bearing currents [40]. The problem is often not detected by the user before the bearings breaks down which can be quite costly for the user due to the downtime of the system in which the induction motor drive operates.

Studies have been made on bearing currents related to PWM drives which identifies the common mode voltage and currents as its cause [40]. [41] describes a system model where the parasitic capacitances is explained as the cause of the bearing currents. The model is further verified with experimental results.

This chapter will focus on small and medium sized machines ($<$30kW), with insulated load, and show that the capacitive effect are dominating. A method for estimating the parasitic capacitors of the motor will also be tested.

9.1 Stray capacitances in an IM

Stray capacitances are created when two conducting materials are separated by an isolator. A useful and descriptive model presented in [41], is here presented in figure 9.1, also showing approximate values for the stray capacitances valid for an 4kW IM. The stray capacitances are, the statorwinding-to-rotor capacitance (C_{sr}), statorwinding-to-frame capacitance (C_{sf}), rotor-to-frame capacitance (C_{rf}) and bearing capacitance (C_b) (when the bearing balls have been separated from the race). Note that C_{rf} and C_b are in parallel and will be treated as a one capacitance. The size of a capacitance increases as the permittivity of the isolating material and the surface area of the conductors are increased and decreases with increasing distance between the conducting materials. Hence, C_{sr} and C_{rf} can approximately be expressed as

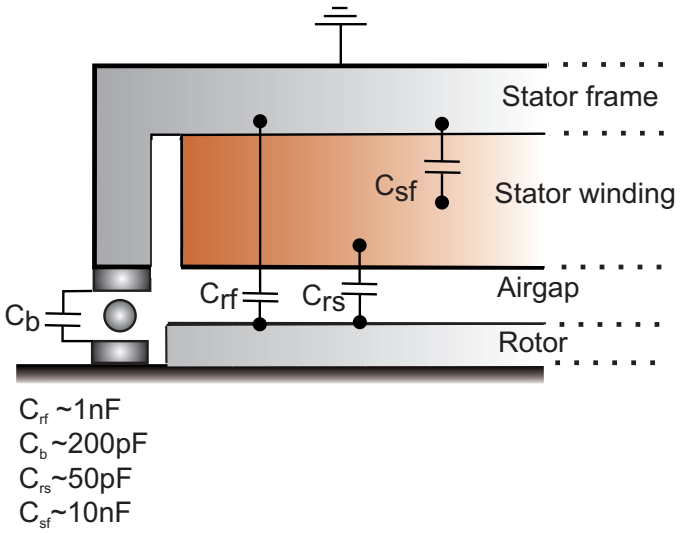

Figure 9.1 Parasitic capacitances in an IM where the approximate values are valid for an 4kW IM.

$$C_{sr} = \epsilon_1 \frac{A_1}{d_1} \tag{9.1}$$

$$C_{rf} = \epsilon_2 \frac{A_2}{d_2} \tag{9.2}$$

where ϵ denotes the permittivity and A and d denotes the area and distance between the conductive material respectively. The ratio of C_{sr}/C_{rf} can now be expressed as

$$\frac{C_{sr}}{C_{sr}} = \frac{\epsilon_1}{\epsilon_2} \frac{A_1 d_2}{A_2 d_1}. \tag{9.3}$$

When the frame size is decreased, the air gap is relatively constant. As a result, it can be assumed that d_1 is kept constant whereas d_2 decreases. However, the ratio A_1/A_2 will increase more compared to the decrease of d_2/d_1. Hence, the ratio of C_{sr}/C_{rf} will increase for smaller frame sizes. The consequences of this change will be discussed in the oncoming sections

9.2 Effects of PWM voltage

When a balanced IM is fed with a balanced sinusoidal voltage, the motor neutral will equal zero volt. However, the sum of the phase voltages will never equal zero when the motor is fed from a three phase PWM voltage.

The zero sequence voltage, v_0, and the zero sequence current for an impedance Z can be defined as

$$v_0 = \frac{v_{an} + v_{bn} + v_{cn}}{3} = \frac{v_{aG} + v_{bG} + v_{cG}}{3} - v_{nG} \tag{9.4}$$

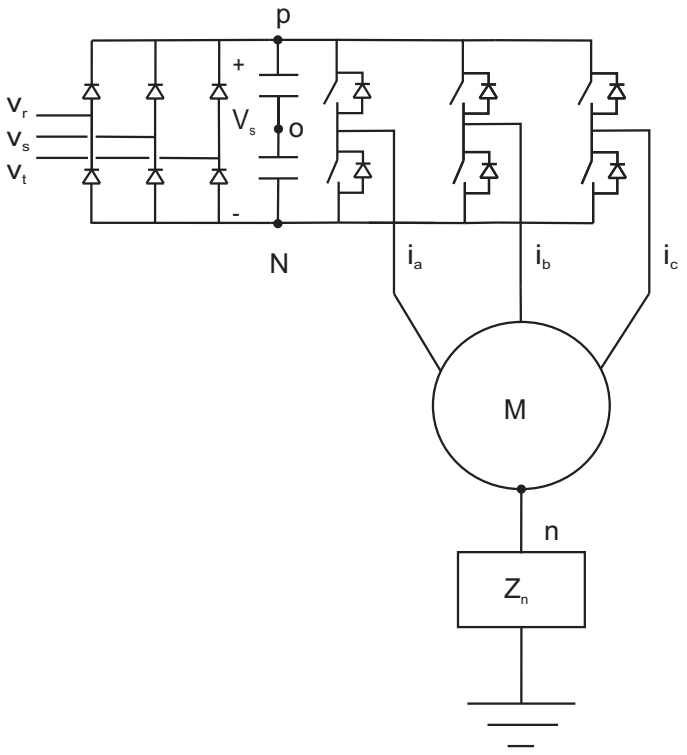

Figure 9.2 Three phase inverter feeding an IM

$$i_0 = \frac{i_a + i_b + i_c}{3} = 3i_n \tag{9.5}$$

Furthermore, the zero sequence impedance, Z_0, can be defined as

$$Z_0 = \frac{v_0}{i_0} \tag{9.6}$$

Combining (9.4) and (9.6) it can be found that,

$$\frac{v_{aG} + v_{bG} + v_{cG}}{3} - i_n Z_n = Z_0 \frac{i_n}{3}$$
$$i_n = \frac{v_{aG} + v_{bG} + v_{cG}}{3} \frac{3}{Z0 + 3Z_n}.$$

Finally, the load neutral voltage, v_{nG} can be expressed as

$$v_{nG} = \frac{v_{aG} + v_{bG} + v_{cG}}{3} \frac{3Z_n}{Z_0 + 3Z_n} \tag{9.7}$$

As a result, the load neutral voltage are determined by a voltage divider between the Z_0 and $3Z_n$.The load neutral voltage has the frequency of the switching frequency in the converter [42].

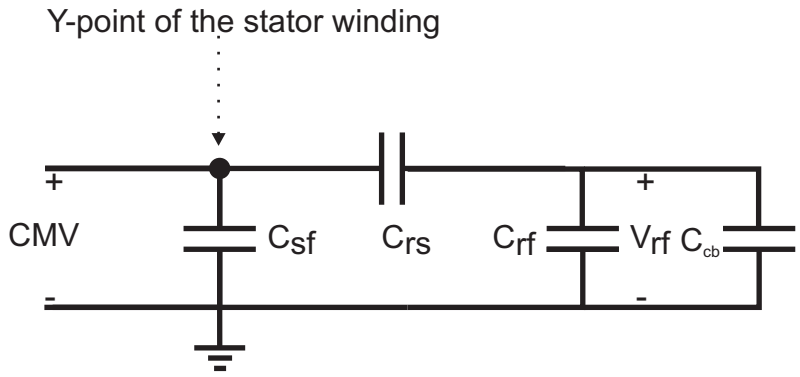

Figure 9.3 Equivalent circuit

9.3 Cause of bearing currents

The different types of bearing currents can be divided in three groups, conducting currents, capacitive currents and discharge currents also called Electric Discharge Machining (EDM). The conducting currents occur at low speed when the bearing balls are in contact with the races. The bearing then creates a short circuit and hence the shaft potential to the ground is zero. When the speed increases, the bearing balls are separated from the races by the oil film of the bearings and the bearing can now be represented by a capacitance in a circuit model of the motor. However, due to impurities in the oil or if the electric field inside the bearing breaks down the film, a short circuit path through the bearing is created (normally 5-20V depending on the bearing [41]) and a discharge current is created.

There are four main causes of bearing currents in a inverter driven drive system

1. When the motor speed is increasing the balls are separated from the races and a thin oil film separates the balls from the race. The bearings can now be represented by a capacitance C_b. C_{sr} and C_b now charges and the shaft potential starts to increase. The voltage over the bearing due to the capacitive coupling are caused by a voltage division between C_{sr} and C_{rf} in parallel with C_b, shown in figure 9.1. The neutral to ground impedance are now assumed to consist only of the stray capacitances in the IM. Figure 9.3 shows the equivalent circuit, this can also be understood by the description of the common mode voltage (CMV) in Section 9.2.

Only capacitive bearing current will occur as long as the film can withstand the shaft voltage. However, when the oil film breaks down, the capacitors will be discharged through the bearing as described earlier. The possible damage the discharge will cause on the bearing depends on the amount of energy that is dissipated. The dissipated energy, which is the energy stored in the capacitor, can be expressed as:

$$W = C\frac{V^2}{2} \tag{9.8}$$

When the size of the IM decreases, the air gap will more or less be the same. Hence,

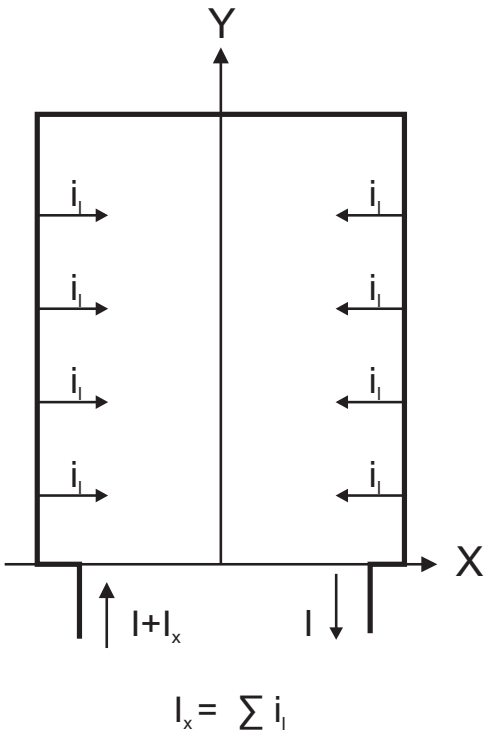

Figure 9.4 Current in a winding

C_{rf} will decrease relative to C_{sr}, refer to Section 9.1, which results in a higher voltage across the bearings. Hence this factor will become more dominating at smaller frame sizes. Typical relative difference of the capacitors between 100kW and 10kW is approximately a factor of 5.

2.[40] explains in detail a type of bearing currents referred to as circulating bearing currents, the theory is also experimentally verified. This section will only give a concise explanation. Figure 9.4, [40], shows the current in one phase winding where Y is the shaft direction. It is evident that currents will leak through the parasitic capacitors to the stator frame and to the rotor. It can be assumed that the IM has perfect symmetry which results in equal leakage current along the winding. The current component consists of the fundamental component and the harmonics, I. The current component I_x, which also can be referred to as the common mode component, represents the grounding (leakage) current in the system. As a result, the current entering the coil is larger that the current that exits the coil. This will result in an unbalance in the stator current which results in a net flux linkage acting on the motor shaft. Hence, a pulsating current will start to flow in the loop shaft- bearing-stator frame.

As the frame size of the IM increases, C_{sf} increases. Hence, the impedance path to the stator frame is decreased which results in higher circulating currents as the motor size increases.

3. Inductive coupling caused by impedance unbalance or symmetry unbalance in the

motor may cause bearing currents. However, this bearing current cause is more dominant i large machines and details are left out.

4. The current always seeks the lowest impedance path back to the inverter. When the IM is connected to a non isolated load, e.g. a pump, high frequency bearing currents can find a lower impedance path through the load, and hence bearing currents can occur.

9.4 Preventive measures

Different preventive measures have been proposed to prevent bearing currents. This section will discuss different solutions and how they affect the different cause of bearing currents.

9.4.1 Grounding of the system

If the load is not electrically isolated, a poor ground connection increases the risk of bearing currents. This is due to the possibility that a lower impedance path to the ground can be found via the load.

9.4.2 Isolated bearings

One solution that is mentioned often are isolation of the bearing on the non drive side. This will stop damage due to circulating bearing currents. However, the problem with capacitive discharge current are not solved. Instead, the non isolated bearing will experience an increased rate of capacitive discharge currents [44]. As a result, both bearing needs to be isolated to overcome this problem [44]. This solution provides that the IM is isolated from the load or that the load is isolated. Otherwise, a current will flow from the motor shaft through the grounded load.

9.4.3 Filter

It is also possible to reduce the cause of bearing currents by filtering the output of the converter. If the high frequency components are reduced the risk of bearing currents are also reduced. Passive filters are available, using inductors and shunt capacitors to form a conventional low pass filter. However, this might not be a cost effective solution since the losses increases (1-1.5%) and additional investment cost [43].

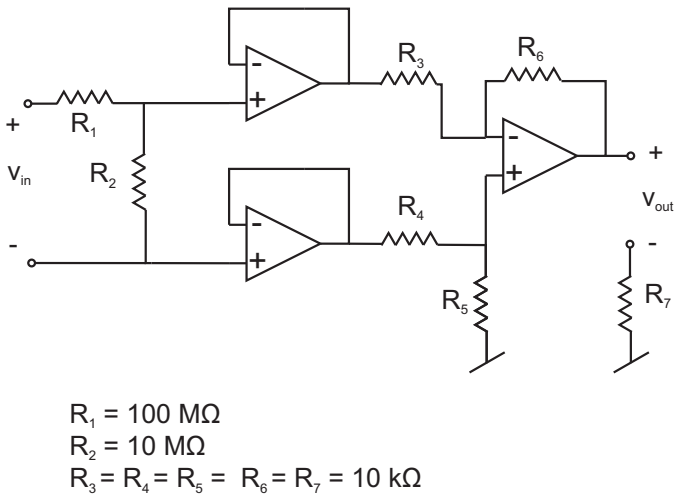

Figure 9.5 Circuit diagram of the voltage measurement device

9.5 Experimental setup

A 4 pole, 4kW IM was used during the laboratory tests. The IM was electrically insulated from the load (DC machine) and the motor bed was connected to ground.

In order to measure the shaft voltage without affecting the shaft voltage, a voltage probe with very high input impedance was needed. Since the shaft to ground impedance is in the order of magnitude of 1MΩ, at 50Hz, a high impedance voltage measurement device where constructed with an input impedance of 110MΩ, the circuit diagram is shown in figure 9.5.

The shaft voltage was measured using a copper wire pressed to the center of the shaft.

In order to determine the magnitude of the stray capacitances an initial series of measurement using an RCL-meter where used. However, the result was not satisfactory. Hence a new method was used where different capacitors where connected between the neutral and motor shaft. A circuit diagram of the stray capacitances including the extra capacitance can be seen in figure 9.7 where C_{extra} denotes the added capacitance. The order of magnitude of the stray capacitances for different frame sizes has been documented, [44], which states an approximate order of 1nF for C_{sr} for a 4kW IM. Hence, eight measurements were performed, for different values of C_{extra} with the maximum of 1nF. The ratio between V_{sr} and V_{rf} can be expressed as

$$\frac{V_{rf}}{V_{sr}} = \frac{C_{sr}}{C_{rf}} + \frac{1}{C_{rf}} C_{extra} \tag{9.9}$$

resulting in a linear relationship between the ratio of V_{rf} and V_{sr} and C_{extra}.

9.5.1 Case A

In Case A the IM was connected to the grid. The purpose of the analysis with a grid connected IM is to verify the theory presented earlier but also to identify the parasitic components of the IM.

The IM was connected with two phases directly to the grid and the third one connected via an autotransformer. This was done in order to create an unbalance in the stator voltage and to investigate its influence on the shaft voltage. The voltage in the third phase was decreased in steps of approximately 15-20V. As the phase voltage decreases, the phase current increases and at approximately 165V it has reached the rated current. Hence 5 measuring points have been performed.

Figure 9.6 shows the normalized voltages, between the stator frame and the shaft, V_{rf}, and the CMV when the stator voltage is balanced (case 1). It can be noted that V_{rf} follows the CMV. This is in agreement with the theory presented in Section 9.2 and 9.3. The peak value of CMV and V_{rf} are in this case approximately 35V and 1V respectively.

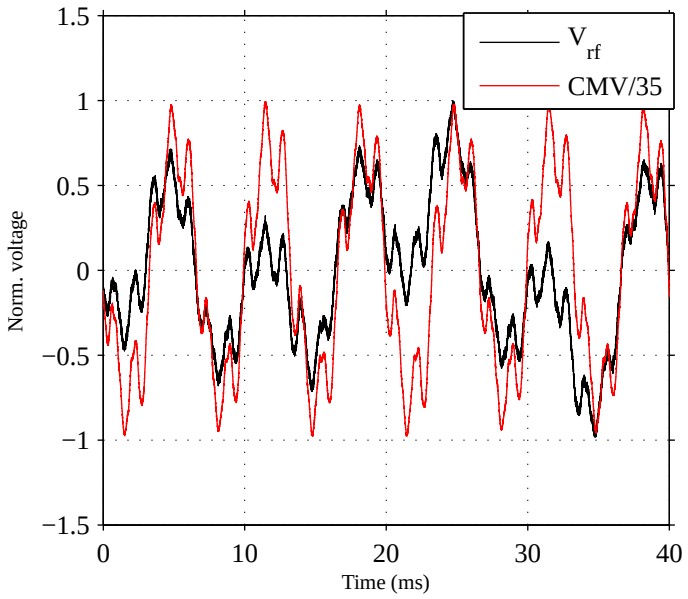

Fig. 9.6 Measured voltage between shaft and stator The amplitude has been normalized for comparison

By introducing an unbalance in the voltage, lowering the amplitude of one phase voltage, the CMV can be increased. This also results in an increase of the V_{rf} as expected, the results is presented in Table 9.1 and 9.2.

The 50Hz component and the 150Hz component was dominating in both CMV and V_{rf}.

Table 9.3 displays the ratio between the V_{rf} and CMV. It can be noted that the magnitude of V_{rf} follows CMV with the exception of the fundamental component at balanced

Table 9.1 Measured CMV voltage

Case	CMV50Hz	CMV150Hz
1	0.88	27
2	9.4	24.3
3	19	21
4	29	18
5	46	15

Table 9.2 Measured voltage of Vrf

Case	Vrf50Hz	Vrf150Hz
1	0.36	0.53
2	0.30	0.44
3	0.59	0.44
4	0.76	0.35
5	1.3	0.26

voltage, the reason for this is yet unknown.

Table 9.3 Measured voltage of V_{rf}

Case	Vrf50Hz/CMV50Hz	Vrf150Hz/CMV150Hz
1	0.413	0.019
2	0.032	0.018
3	0.031	0.022
4	0.026	0.019
5	0.028	0.017

By assuming that the third component of the CMV is divided between the stator to rotor impedance and rotor to frame impedance, which are assumed to consist only of stray capacitors, the value of the stray capacitances can be estimated. Figure 9.8 shows the measured ratio of the third harmonic of the CMV and V_{rf} as a function of C_{extra} together with the least mean square of the data points. It can be found that the ratio is approximately 2.3% and the stray capacitances are estimated to, C_{sr}=33pF and C_{rf}=1.4nF.

9.5.2 Case B

The IM was now fed from a frequency converter. The motor bed was connected to safety ground, as well as the PE in the cable from the converter. The cable screen remained disconnected. Figure 9.9 shows V_{rf} which shows a significant difference compared to case A for reasons explained in Section 9.2 . Figure 9.10 shows a zoom of V_{rf} , where

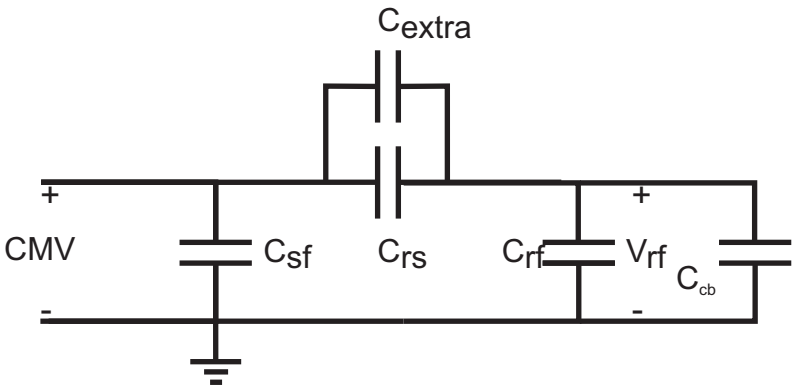

Figure 9.7 Equivalent circuit diagram

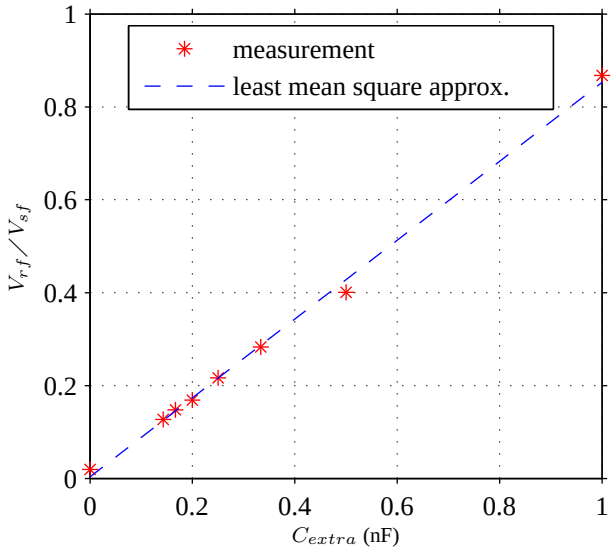

Fig. 9.8 Measured ratio between V_{rf} and V_{sr} for different values of the extra capacitor connected in parallel with C_{sr}

two charges and two natural capacitor discharges of the stray capacitances between the rotor and ground are shown. Figure 9.11 shows CMV and V_{rf}, normalized for comparison. It can be noted that V_{rf} follows the CMV.

Figure 9.12 shows a typical discharge caused by a discharge current through the bearing.

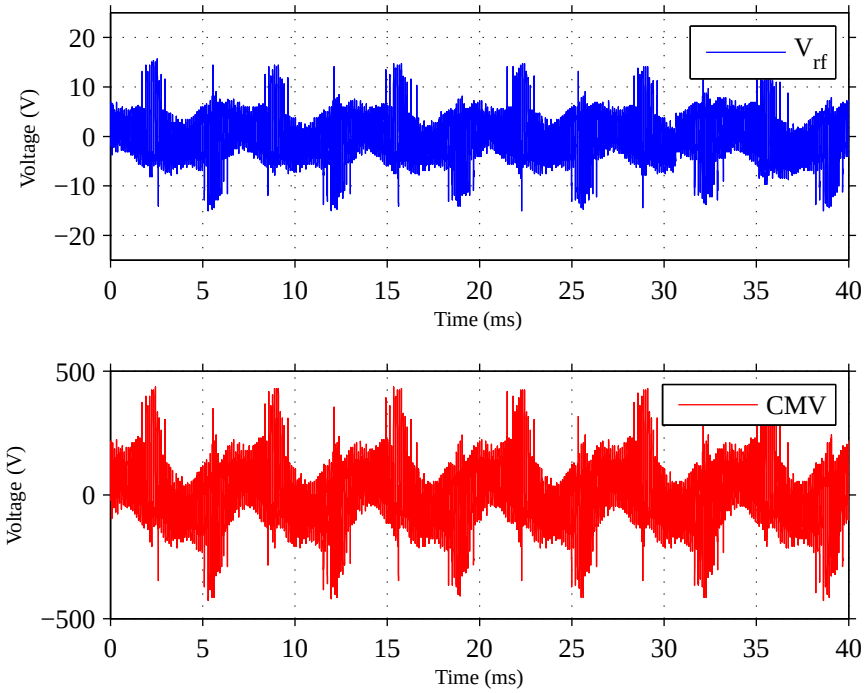

Fig. 9.9 Measured voltage between shaft and stator frame and the load neutral to stator frame

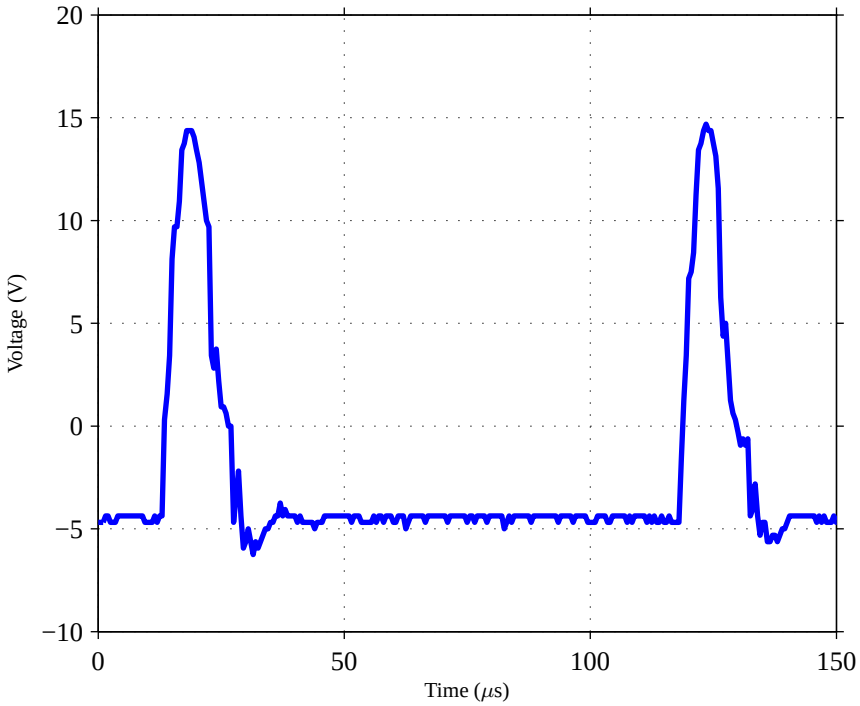

Fig. 9.10 Measured voltage between shaft and stator case

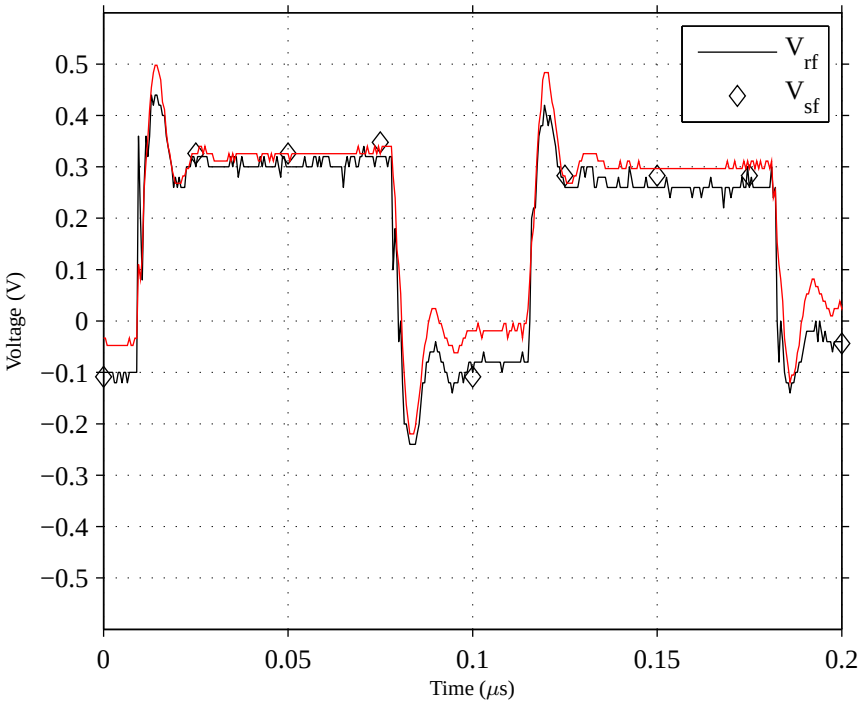

Fig. 9.11 Normalized voltage for comparison V_{rf} and CMV.

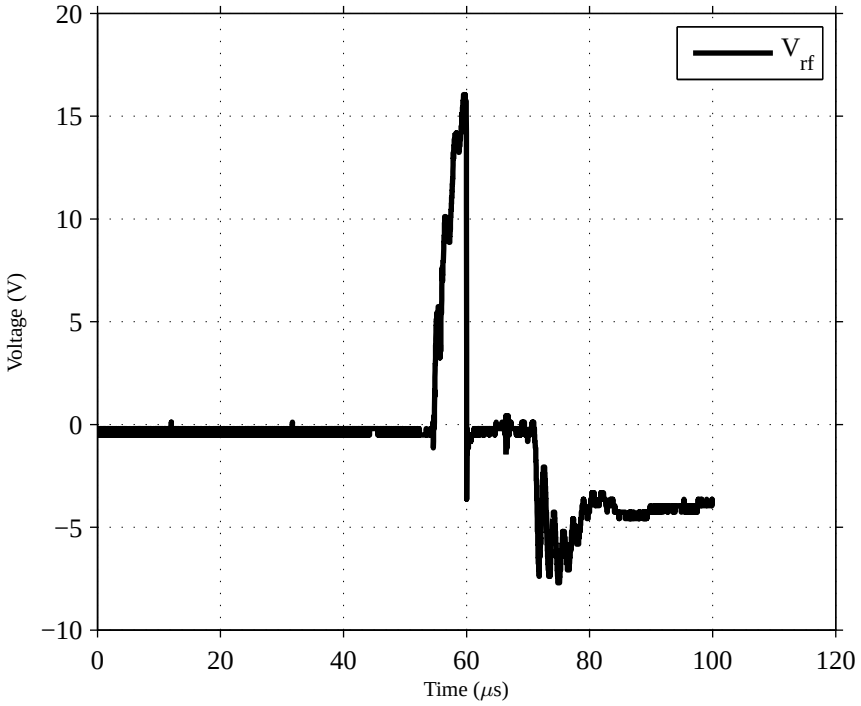

Fig. 9.12 Typical discharge of the shaft causing EDM

Chapter 10

Concluding Remarks and future work

10.1 Concluding Remarks

In this thesis an overview of different electric drive systems and power electronic components have been presented. Furthermore, HVAC load profiles have been described in order to analyze saving potentials for different drive system setups. Focus during the analysis was placed on different IM designs, (different energy labels), different control schemes of the IM and the frequency converter. It has been shown that the simulated results of the switching losses in a frequency converter, using different SVM schemes, showed a close correlation compared to the measurement. It has further been shown that the simulated efficiency difference between constant V/Hz control and optimal V/Hz control reproduced with close correlation during the measurements. Regarding the loss components in the semiconductor devices, the calculation and measurements differed, to some extent, for the diode in series with the MOSFET and the freewheeling diode, whereas the calculation for the transistor was well matched with the measurement. It could be determined that the conductive losses in the series diode and the switching and conductive losses in the freewheeling diode differed from the calculated values. The reason for this cause could not be determined explicitly. Possible modification of the measurement procedure would be to isolate each component from the nearby components, extend the temperature measurement to more components using additional equipment.

The analysis of potential savings using different IM and different control was based on the simulations. The main conclusion was that the saving potential was higher for an over dimensioned IM if it was operated at optimal V/Hz. It was further observed that the potential increased witch increased over dimensioning. The latter can be explained by the improved efficiency that is achieved using optimal V/Hz control at light loads. It has further been shown that the potential saving made by replacing the IM or by replacing both the IM and the converter is highly load dependent. The analysis of IM replacement was straight forward since the potential saving increases with increasing load. The worst case scenario was a break even situation when an eff3 IM was replaced with an eff1 IM

for a extremely light load. The analyze has also shown that the choice between an eff2 and eff1 IM, for the given load profiles, always generate the highest saving for the eff1 IM. It is interesting to note that, during the time period 1998-2003, eff2 label took 86% of the market share compared to eff1 8% and eff3 6%.

When it comes to the analysis of the difference between constant and optimal V/Hz it has been shown that the relative saving increases with decreasing load but not necessarily the absolute savings since the power demand decreases with decreasing load. However, the general conclusion is that savings will be made for all of the given load profiles except the extreme cases of 100% and 80% load demand during 100% of the time.

Finally, it was shown that the method, described in Chapter 9, for determine the stray capacitances in an IM worked well.

10.2 Proposals of Future Work

In this thesis the main focus has been placed on a 4kW IM including simulations and measurements with focus on efficiency determination. The first step for future work is to solve the shortcomings in the loss calculations and perform a detailed analysis of the harmonic losses in the IM. Further investigation on the effect of different switching schemes, adding of snubber circuits and the resulting influence on both efficiency and EMI are proposed.

The topic of permanent magnet motors has yet only been briefly discussed. Hence, a similar study on PM motors, as was done for the IM, should be of highest interest. Furthermore, a study of the efficiency for decreased motor ratings, both for IM and PM motors, is proposed due to the large number of use in today's buildings.

References

[1] Dalenbäck, J.O, Göransson, A, Jagemar, L, Nilson,A, Olsson,D, Pettersson,B, *Åtgärder för ökad energieffektivisering i bebyggelse, Chalmers EnergiCentrum, sep 2005*

[2] *Från byggsekt till byggsektor SOU 2000:44, May 2000*

[3] Rooks, J, Wallace A, *Energy efficiency of variable speed drive systems, Pulp and Paper Industry Technical Conference, June 2003, pp) 160- 163*

[4] Nilsson L. *Energy systems in transition-Electricity use in pumping and air-handeling systems*, LTH (Lund Institute of Technology, Theisis for lic.Eng. Lund), 1991

[5] Nilsson L. *A system oriented assessment of electricity use and efficiency in pumping and air-handeling*, LTH (Lund Institute of Technology, Report 1 IMES/EESS Lund), 1991

[6] Barry Crozier *Application guide AG Enhancing the Performance of Oversized Plant*, May 2000

[7] F. Abrahamsen *Energy Optimal Control of induction Motor Drives*, Institute of Energy Technology, Alborg University, February 2000

[8] F. Abrahamsen F. Blaabjerg, J. K. Pedersen, P. Z. Grabowski, P. Thøgersen *On the Energy Optimized Control of Standard and High-Efficiency Induction Motors in CT and HVAC Applications*, IEEE Transactions, vol. 34, No. 4 July 1998

[9] Cao-Minh Ta, Yoichi Hori *Convergence imoprovement of Efficiency optimization control of induction motor drives*, IEEE, 2001

[10] A. Lamine, E. Levi, *Dynamic induction machine modelling considering the stray load losses*, Universities Power Engineering Conference, 6-8 Sept. 2004, pp. 582-586

[11] A. Wallace, A.Juanne, A. Nagornyy *Evaluation of stray load losses in induction motors at different supply frequencies*, Industry Applications Conference, 13-18 Oct. 2002. pp 2296-2300

[12] D. Holmes Grahame , A. Lipo Thomas *Pulse Width Modulation for Converters Principles and Practice*, IEEE press 2003

[13] Trzynadlowski, A.M.; Kirlin, R.L.; Legowski, S.F. *Space vector PWM technique with minimum switching losses and a variable pulse rate* , Industrial Electronics, IEEE Transactions on Volume 44, Issue 2, April 1997

[14] Yu, Z. Mohammed, A. Panahi, I., *A review of three PWM techniques,* American Control Conference, 1997. Proceedings of the 1997 Volume 1, 4-6 June 1997

[15] L. Deboy, G. Zverev, I. *Matched pair of CoolMOS transistor with SiC-Schottky diode - advantages in application Lorenz,* Industry Applications IEEE Transactions on Volume 40, Issue 5, Sept.-Oct. 2004, pp 1265 - 1272

[16] Ozpineci, B.; Tolbert, L.M. *Characterization of SiC Schottky diodes at different temperatures,* Power Electronics Letters, IEEE Volume 1, Issue 2, June 2003, pp 54 - 57

[17] Ozpineci, B., Tolbert, L.M., Islam, S.K., Hasanuzzaman, M. *Effects of silicon carbide (SiC) power devices on HEV PWM inverter losses,* Industrial Electronics Society, 2001. IECON '01. The 27th Annual Conference of the IEEE Volume 2, 29 Nov.-2 Dec. 2001, pp 1061 - 1066

[18] Abel, E. Elmroth, A., Byggnaden son system, Forskningsrådet Formas, 2006

[19] Hans P. Andersen *Europeans agree on energy standards for pumps,* Grundfos,March 2005

[20] Ned Mohan, Electric Drives an integrative approach 2003 pp 15-1 to 15-12

[21] C. B. Rasmussen, H.R. Andersen, E, Ritchie, J. K Pedersen *Design and Efficiency Comparation of Electric Motors for Low Power Variable Speed Drives with Focus on Permanent Magnet Motors,* IEEE, Electrical Machines and Drives, sep 1995

[22] Karlsson A. *Behovsstyrd ventilation i lokalbyggnader, Innebörd och strömningstekniska konsekvenser,* Departement of Energy and Environment, Chalmers 2005

[23] Danfoss *The drive to reduce Costs ans Improve System Control,* May 2000

[24] J. Dodge, J. Hess, ÏGBT Tutorial", Advanced power technology, July 1 2002

[25] N. Mohan, T.Undeland ,W.P. Robbins *Power Electronics Converters, Applications and Design,*John Wiley and Sons, Inc 1995.

[26] Linder, S. *Power Semoconductors,* 2006: EFPL Press. 300

[27] Aníbal T. De Almeida João L. C. Marinho Fernando J. T. E. Ferreira Paula Fonseca *Inception Report: Analysis of existing technical and market,* 2006, ISR-University of Coimbra

[28] Lelkes, A. Krotsch, J. De Doncker, R.W. *Low-noise external rotor BLDC motor for fan applications , Industry Applications Conference, 2002. 37th IAS Annual Meeting. Conference Record of the Volume 3, 13-18 Oct. 2002,pp 2036 - 2042, vol.3*

[29] Lelkes, A. Bufe, M. *BLDC motor for fan application with automatically optimized commutation angle , Power Electronics Specialists Conference, PESC 04. 2004 IEEE 35th Annual Volume 3, pp 2277 - 2281, Vol.3*

[30] Mora, J.L.V., Lelkes, A., Pacas, J.M. *External rotor PM motor fed by a load commutated inverter for fan applications , Industrial Electronics Society, IEEE 2002 28th Annual Conference, Volume 1, 5-8 Nov. 2002, pp 767 - 770*

[31] Sozer, Y. Torrey, D.A. *Adaptive torque ripple control of permanent magnet brushless DC motors, Applied Power Electronics Conference and Exposition, APEC '98. Conference Proceedings 1998, Thirteenth Annual Volume 1, 15-19*

[32] Jeon, Y.S. Mok, H.S. Choe, G.H. Kim, D.K. Ryu, J.S. *A new simulation model of BLDC motor with real back EMF waveform , Iomputers in Power Electronics, The 7th Workshop on 16-18 July 2000, pp 217-220*

[33] D. W. Novotny and T.A Lipo *Vector control and dynamics of AC drives, Oxford science publications, 1996, ISBN 0 198564392*

[34] Y. Sozer, D.A. Torrey *Adaptive Torque Ripple Control of Permanent Magnet Brushless DC Motors*, Applied Power Electronics Conference and Exposition, Feb. 1998. vol1 pp15-19

[35] Clayton R. Paul *Introduction to Electromagnetic Compatibility*, Wileyintersscience, 2006

[36] László Tihanyi *Electromagnetic compatibility in power electronics*, 1995

[37] Keith Armstrong *Banana skinns compendium*, Cherry Clough Consultants 5th March 2007

[38] *IEEE Standard test Procedure for Polyphase Induction Motors and generators, March 10 1991*

[39] T. Thiringer *Measurements and Modelling of Low-Frequency Disturbances in Induction Machines generators, , Chalmers Unicersity of Thechnology, 1996*

[40] S. Chen, A. Lipo, D. Novotny, *Circulating Type Motor Bearing Current In Inverter Drives IEEE Industry Applications Magazine, Jan-Feb 1998 Vol 4 , Issue 1*

[41] D. Busse, J. Erdman, R.J. Kerkman, D. Schlegel, G. Skibinski, *Bearing currents and their relationship to PWM drives Power Electronics IEEE Transactions on Volume 12, Issue 2, March 1997 pp 243 - 252*

[42] Un, E. Hava, A.M. *Performance analysis and comparison of reduced common mode voltage PWM and standard PWM techniques for three-phase voltage source inverters Applied Power Electronics Conference and Exposition, Twenty-First Annual IEEE Publication, 19-23 March 2006*

[43] Finlayson, P.T *Output filters for PWM drives with induction motors Industry Applications Magazine, IEEE Volume 4, Issue 1, Jan.-Feb. 1998, pp. 46 - 52*

[44] Macdonald, D. Gray, W. *PWM drive related bearing failures Macdonald IEEE Volume 5, Issue 4, July-Aug. 1999, pp. 41 - 47*